

Nucleon Electromagnetic Form Factors

C. F. Perdrisat,¹ V. Punjabi,² M. Vanderhaeghen^{1,3}

¹ College of William and Mary, Williamsburg, VA 23187

² Norfolk State University, Norfolk, VA 23504

³ Thomas Jefferson National Accelerator Facility, Newport News, VA 23606

January 18, 2019

Abstract

There has been much activity in the measurement of the elastic electromagnetic proton and neutron form factors in the last decade, and the quality of the data has greatly improved by performing double polarization experiments, in comparison with previous unpolarized data. Here we review the experimental data base in view of the new results for the proton, and neutron, obtained at JLab, MAMI, and MIT-Bates. The rapid evolution of phenomenological models triggered by these high-precision experiments will be discussed, including the recent progress in the determination of the valence quark generalized parton distributions of the nucleon, as well as the steady rate of improvements made in the lattice QCD calculations.

Contents

1	Introduction	4
2	Nucleon form factors from eN cross sections	6
2.1	Early nucleon structure investigations	6
2.1.1	The Dirac and Pauli nucleon form factors	7
2.1.2	The electric and magnetic form factors	9
2.1.3	Isovector and isoscalar nucleon form factors	10
2.1.4	Form factors in the Breit frame	10
2.2	Rosenbluth form factor separation method	11
2.2.1	Proton form factor measurements	11
2.2.2	Neutron electric form factor measurements	13
2.2.3	Neutron magnetic form factor measurements	15
2.2.4	Rosenbluth results and dipole form factor	16
2.3	Nucleon size	17
3	Nucleon form factors from double polarization observables	20
3.1	Polarization transfer	20
3.2	Asymmetry with polarized targets	21
3.3	Double polarization experiments	23
3.3.1	Proton form factors from polarization experiments	23
3.3.2	Results from recoil polarization experiments	25
3.3.3	Measurements of neutron form factors with polarization experiments	26
3.4	Relative merit of recoil polarization versus target asymmetry measurements	29
3.4.1	Proton form factors	29
3.4.2	Neutron form factors	32
3.5	Discussion of the form factor data	33
3.6	Rosenbluth results and radiative corrections	35
4	Theoretical interpretation of nucleon electromagnetic form factors	41
4.1	Dispersion theory	42
4.1.1	Vector Meson Dominance (VMD)	42
4.1.2	Dispersion analyses	43
4.2	Quark models versus pion-cloud models	45
4.2.1	Non-relativistic constituent quark models	45
4.2.2	Relativistic constituent quark models	47
4.2.3	Pion cloud models	50
4.3	Radial distributions and shape of the nucleon	53
4.3.1	Radial distributions of charge and magnetization	53
4.3.2	Intrinsic quadrupole moment and the shape of the nucleon	56
4.4	Chiral perturbation theory	57
4.5	Lattice QCD and chiral extrapolation	59
4.5.1	Lattice simulations	59

4.5.2	Chiral extrapolations	65
4.6	Generalized parton distributions (GPDs)	70
4.6.1	Definition of GPDs and form factor sum rules	70
4.6.2	Models for the GPDs H and E	72
4.6.3	GPDs and transverse structure of hadrons	76
4.7	Perturbative QCD (pQCD)	78
4.7.1	pQCD predictions for form factors	78
4.7.2	The transition to pQCD	79
5	Conclusions and outlook	82

1 Introduction

The characterization of the structure of the nucleon is a defining problem of hadronic physics, much like the hydrogen atom is to atomic physics. Elastic nucleon form factors (FFs) are key ingredients of this characterization. As such, a full and detailed quantitative understanding of the internal structure of the nucleon is a necessary precursor to extending our understanding of hadronic physics.

The electromagnetic (e.m.) interaction provides a unique tool to investigate the internal structure of the nucleon. The measurements of e.m. FFs in elastic as well as inelastic scattering, and the measurements of structure functions in deep inelastic scattering of electrons, have been a rich source of information on the structure of the nucleon.

The investigation of the spatial distributions of the charge and magnetism carried by nuclei started in the early nineteen fifties; it was profoundly affected by the original work of one of its earliest pioneers, Hofstadter and his team of researchers [Hof53b], at the Stanford University High Energy Physics Laboratory. Quite early the interest turned to the nucleon; the first FF measurements of the proton were reported in 1955 [Hof55], and the first measurement of the neutron magnetic FF was reported by Yearian and Hofstadter [Yea58] in 1958. Simultaneously much theoretical work was expanded to the development of models of the nucleus, as well as the interaction of the electromagnetic probe with nuclei and the nucleon. The prevailing model of the proton at the time, was developed by Rosenbluth [Ros50], and consisted of a neutral barionic core, surround by a positively charged pion cloud.

Following the early results obtained at the Stanford University High Energy Physics Laboratory; similar programs started at several new facilities, including the Laboratoire de l'Accélérateur Linéaire in Orsay, (France), the Cambridge Electron Accelerator, the Electron-Synchrotron at Bonn, and the electron accelerators at CEA-Saclay and at NIKHEF. The number of electron accelerators and laboratories, and the beam quality, grew steadily, reflecting the increasing interest of the physics problems investigated and results obtained using electron scattering. The most recent generation of electron accelerators, which combine high current with high polarization electron beams, at MIT-Bates, the Mainz Microtron (MAMI), and the Continuous Electron Beam Accelerator Facility (CEBAF) of the Jefferson Lab (JLab), have made it possible to investigate the internal structure of the nucleon with unprecedented precision. The CEBAF accelerator adds the unique feature of high energy which allows to perform measurements of nucleon e.m. FFs to large momentum transfers. Sizeable parts of the programs at these facilities were and are oriented around efforts to characterize the spatial distribution of charge and magnetization in nuclei and in the nucleon.

The recent and unexpected results from JLab of using the polarization transfer technique to measure the proton electric over magnetic FF ratio G_{Ep}/G_{Mp} [Jon00, Gay02, Pun05], has been the revelation that the FFs obtained using the polarization and Rosenbluth cross section separation methods, were incompatible with each other, starting around $Q^2 = 3 \text{ GeV}^2$. The FFs obtained from cross section data had suggested that $G_{Ep} \sim G_{Mp}/\mu_p$, where μ_p is the proton magnetic moment; the results obtained from recoil polarization data clearly show that the ratio G_{Ep}/G_{Mp} decreases linearly with increasing momentum transfer Q^2 . The numerous attempts to explain the difference in terms of radiative corrections which affect the results of the Rosenbluth separation method very significantly, but polarization results only minimally, have led to the previously neglected calculation of two hard photon exchange with both photons sharing the momentum transfer.

These striking results for the proton e.m. FF ratio as well as high precision measurements of the neutron electric FF, obtained through double polarization experiments, have put the field of nucleon elastic e.m. FFs into the limelight, giving it a new life. Since the publication of the JLab ratio measurements, there have been two review papers on the subject of nucleon e.m. FFs [Gao03, Hyd04]. The present review complements the

previous ones by bringing the experimental situation up-to-date, and gives an overview of the latest theoretical developments to understand the nucleon e.m. FFs from the underlying theory of the strong interactions, Quantum Chromodynamics (QCD). We will focus in this review on the space-like nucleon e.m. FFs, as they have been studied in much more detail both experimentally and theoretically than their time-like counterparts. We will also not discuss the strangeness FFs of the nucleon which have been addressed in recent years through dedicated parity violating electron scattering experiments. For a recent review of the field of parity violating electron scattering and strangeness FFs, see e.g. Ref. [Bei05].

The paper is organized as follows. Section 2 of this review is dedicated to a description of the beginning of the field of electron scattering on the nucleon, and the development of the theoretical tools and understanding required to obtain the fundamental FFs. Elastic differential cross section data lend themselves to the separation of the two e.m. FFs of proton and neutron by the Rosenbluth, or LT-separation method. All experimental results obtained in this way are shown and discussed.

Section 3 discusses the development of another method based on double polarization, either measuring the proton recoil polarization in $\vec{e}p \rightarrow e'\vec{p}$, or the asymmetry in $\vec{e}p \rightarrow ep$. The now well documented and abundantly discussed difference in the FF results obtained by Rosenbluth separation on the one hand, and double polarization experiments on the other hand, is examined in section 3.5. The radiative corrections, including two-photon exchange corrections, essential to obtain the Born approximation FFs, are discussed in details in section 3.6.

In Section 4, we present an overview of the theoretical understanding of the nucleon e.m. FFs. In Sect. 4.1, we firstly discuss vector meson dominance models and the latest dispersion relation fits. To arrive at an understanding of the nucleon e.m. FFs in terms of quark and gluon degrees of freedom, we next examine in Sect. 4.2 constituent quark models. We discuss the role of relativity when trying to arrive at a microscopic description of nucleon FFs based on quark degrees of freedom in the few GeV^2 region. The present limitations in such models will also be addressed. In Sect. 4.3, we highlight the spatial information which can be extracted from the nucleon e.m. FFs, the role of the pion cloud, and the issue of shape of hadrons. Sect. 4.4 discusses the chiral effective field theory of QCD and their predictions for the nucleon e.m. FFs at low momentum transfers. Sect. 4.5 examines the ab initio calculations of nucleon e.m. FFs using lattice QCD. We will compare the most recent results and the open issues in this field. We also explain how the chiral effective field theory can be useful in extrapolating lattice QCD calculations for FFs, performed at larger than physical pion mass values, to the physical pion mass. In Sect. 4.6, we present the quark structure of the nucleon and discuss how the nucleon e.m. FFs are obtained through sum rules from underlying generalized (valence) quark distributions. We show the present information which has been obtained on GPDs from fits of their first moments to the recent precise FF data set. Finally, in Sect. 4.7, we outline the predictions made by perturbative QCD at very large momentum transfers and confront them with the FF data at the largest available Q^2 values.

We end this review in Section 5 with our conclusions and spell out some open issues and challenges in this field.

2 Nucleon form factors from eN cross sections

In this section we outline the development of what was, in the early nineteen fifties, a new and exciting field of investigation of the structure of nuclei, using the elastic scattering of electrons with several hundreds of MeV energy. We also discuss the evolution of the Rosenbluth separation method to its present form, and show all FF results obtained using this method for both the proton and the neutron.

In the late forties, several papers had pointed out the possibility of measuring the shape and size of nuclei by observing deviations from Mott scattering by a point charge; most influential were the papers by Rose [Rose47], who argued that “high energy” electrons would be most suited for such studies, with 50 MeV a best value; and by Rosenbluth [Ros50] for the proton, who provided explicit scattering formula taking into account both charge and the anomalous magnetic moment, with the use of “effective” charge and magnetic moment.

The first report of work done at the Stanford University High Energy Physics Laboratory at energies larger than 100 MeV, was reported by Hostadter, Fechter and McIntyre [Hof53a], who detected deviations from scattering by a point charge in carbon and gold. The first review paper of the field, written by Hofstadter in 1956 [Hof56] included the first proton FF measurement, up to a momentum transfer squared of $q^2 = 13.3 \text{ fm}^{-2}$, or 0.52 GeV^2 .

The field had acquired enough exciting new results by the mid nineteen sixties to receive its next extensive review, by Wilson and Levinger [Wil64]. More recently the nucleon FFs were reviewed by Gao [Gao03] and by Hyde-Wright and de Jager [Hyd04].

2.1 Early nucleon structure investigations

In the middle nineteen fifties, it had been known for more than 20 years that the proton could not be just a mathematical point charge and point magnetic moment. Indeed the measurement of the proton’s magnetic moment by Stern [Ste33] had revealed a value ~ 2.8 times larger than expected for a spin- $\frac{1}{2}$ Dirac particle.

Earliest definitions of a FF are usually credited to Rosenbluth [Ros50]; in this early reference Rosenbluth discussed a model of the proton consisting of a neutron core and a positively charge meson cloud, known then as the weak meson coupling model. A high energy electron was expected to penetrate the mesonic cloud and to “feel” reduced charges and magnetic moments, e' and $\kappa'e'$. Expressions for such quantities as $\frac{e'}{e}$ and $\frac{\kappa'e'}{\kappa_0 e}$ had been derived by Schiff in 1949 [Schi49].

In his seminal review paper Hofstadter [Hof56] was the first to relate the results of McAllister and Hofstadter [McA56] for the ep cross section in elastic scattering at given angle and energy, to the Mott cross section for the scattering of a spin $\frac{1}{2}$ electron by a spin-less proton, σ_{Mott} , with internal charge density distribution $\rho(r)$, as follows:

$$\sigma(\theta) = \sigma_{Mott} \left[\int_{volume} \rho(r) e^{i\vec{q} \cdot \vec{r}} d^3r \right]^2 = \sigma_{Mott} [F(q)]^2, \quad (1)$$

where:

$$\sigma_{Mott} = \left(\frac{Ze^2}{2E} \right)^2 \frac{\cos^2 \frac{\theta}{2}}{\sin^4 \frac{\theta}{2}}. \quad (2)$$

In this early framework a phenomenological form FF squared was obtained from absolute differential cross section measurements simply as:

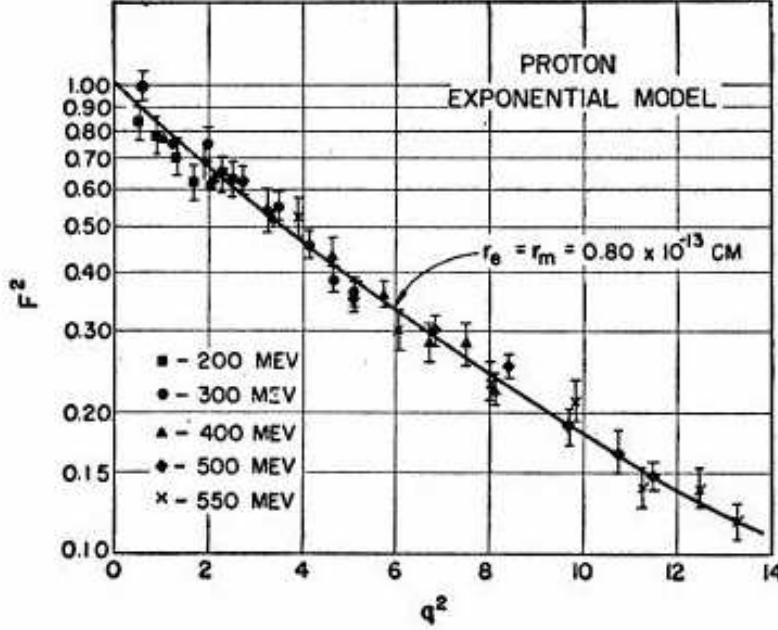


Figure 1: Fig. 27 in Ref.[Hof58], with figure caption “The square of the FF plotted against q^2 . q^2 is given in units of 10^{26}cm^2 . The solid line is calculated for the exponential model with rms radii $= 0.80 \times 10^{-13} \text{cm}$.”

$$[F(q)]^2 = \frac{\sigma(q)}{\sigma_{Mott}(q)}, \quad \text{with} \quad \vec{q} = \vec{p}_0 - \vec{p}_1 \quad \text{and} \quad q = |\vec{q}|, \quad (3)$$

where \vec{q} , \vec{p}_0 and \vec{p}_1 are the center-of-mass (CM) momentum transfer, and incident and scattered electron momenta, respectively. The historically significant results of these first measurements of the proton FF are seen in Fig. 1.

2.1.1 The Dirac and Pauli nucleon form factors

A direct connection between the reduced charge and magnetic moments discussed in [Ros50] and measurable observables was first proposed by Clementel and Villi [Cle56], who defined FFs on the basis of Rosenbluth’s discussion of effective charge and magnetic moments, following [Schi49], as $F_1(q) = \frac{e'}{e}$ and $F_2(q) = \frac{\kappa' e'}{\kappa_0 e}$. These FFs were then introduced in experimental papers by Hofstadter and coworkers [Hof56, McA56], who generalized the “effective” charge and magnetic moment concepts by associating the first with the deviation from a point charge Dirac particle (Dirac FF, F_1), and the second with the deviation from a point anomalous magnetic moment (Pauli FF, F_2).

Various, stepwise progresses were made from intensive work in the late 1960s, work which must be credited to Foldy [Fol52], Salzman [Sal55], Zemach [Zem56], and Yennie *et al.* [Yen57].

In lowest order, elastic scattering of an electron by the proton is the result of the exchange of a single virtual photon of invariant mass squared $q_\mu^2 = \omega^2 - q^2 = -4E_{beam}E_e \sin^2 \frac{\theta_e}{2}$, (the last step neglects the electron mass), where $\omega = E_{beam} - E_e$, the energy loss of the electron, and $\vec{q} = \vec{p}_{beam} - \vec{p}_e$, the vector momentum change of the electron; θ_e is the Lab electron scattering angle. For scattering in the space like region, \vec{q}_μ^2 is negative. The

time-like region, where \vec{q}_μ^2 is positive, can be accessed for example in $e^-e^+ \rightarrow p\bar{p}$ or $p\bar{p} \rightarrow e^-e^+$; it will not be discussed in this review.

Given the smallness of the fine structure constant $\alpha = e^2/4\pi \sim 1/137$, it has been common until recently, to neglect all higher order terms, except for the next order in α which is treated as a radiative **correction**, thus implicitly assuming that the single photon diagram, corresponding to the Born approximation, is determinant of the relation between cross section and FFs; we will revisit this point in section 4. In the single photon or Born approximation, illustrated in Fig. 2 the amplitude for elastic scattering can be written as the product of the four-component leptonic and hadronic currents, ℓ_ν and \mathcal{J}_μ , respectively:

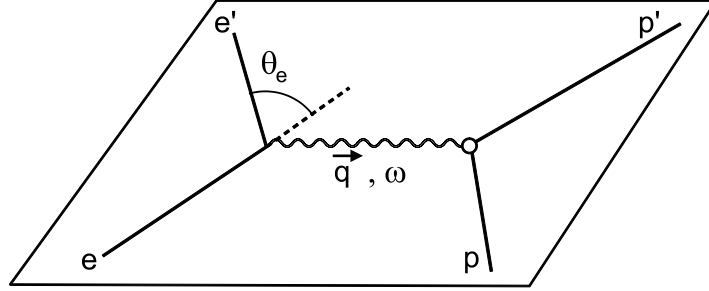


Figure 2: Feynman diagram for the single-photon exchange, or Born term, for elastic ep scattering. The labels k, k' and p, p' refer to the initial and final state electron and proton four-vectors, respectively.

$$i\mathcal{M} = \frac{-ig_{\mu\nu}}{q_\mu^2} [ie\bar{u}(k')\gamma^\nu u(k)] [ie\bar{N}(p')\Gamma^\mu(p', p)N(p)] = \frac{-i}{q_\mu^2} \ell_\mu \mathcal{J}^\mu, \quad (4)$$

where Γ^μ contains all information of the nucleon structure, u and N are the electron- and nucleon spinors, respectively, $g_{\mu\nu}$ is the metric tensor and k, k', p and p' are the four-momenta of the incident and scattered electron and proton, respectively. To ensure relativistic invariance of the amplitude \mathcal{M} , Γ^μ can only contain p, p' and γ^μ , besides scalars, masses and Q^2 .

As was shown by Foldy [Fol52], the most general form for the hadronic current for a spin $\frac{1}{2}$ -nucleon with internal structure, satisfying relativistic invariance and current conservation is:

$$\mathcal{J}_{hadronic}^\mu = ie\bar{N}(p') \left[\gamma^\mu F_1(Q^2) + \frac{i\sigma^{\mu\nu}q_\nu}{2M} F_2(Q^2) \right] N(p), \quad (5)$$

where $Q^2 = \vec{q}^2 - \omega^2 = -q_\mu^2$, is the negative of the square of the invariant mass q_μ^2 of the virtual photon in the one-photon exchange approximation in ep scattering, and F_1 and F_2 are the two only FFs allowed by relativistic invariance. Furthermore, the anomalous part of the magnetic moment for the proton is $\kappa_p = \mu_p - 1$, and for the neutron $\kappa_n = \mu_n$, in nuclear magneton-units, $\mu_N = \frac{e\hbar}{2M}$, with values $\kappa_p = 1.7928$ and $\kappa_n = -1.9130$, respectively; M is the nucleon mass. It follows that in the static limit, $Q^2=0$:

$$\begin{aligned} F_{1p}(0) &= 1, & F_{2p}(0) &= \kappa_p, \\ F_{1n}(0) &= 0, & F_{2n}(0) &= \kappa_n. \end{aligned}$$

for the proton and neutron, respectively.

In the one-photon approximation $F_1(Q^2)$ and $F_2(Q^2)$ are real functions which depend upon Q^2 only, and are therefore relativistically invariant. When higher order terms with two photons exchange are included, there are in general 6 FFs, which can be written in terms of 3 complex ones (see Appendix A).

The Lab cross section is then:

$$\frac{d\sigma}{d\Omega_e} = \frac{|\overline{\mathcal{M}}|^2}{64\pi^2} \left(\frac{E_2}{E_1} \right)^2 \frac{1}{M} \quad \text{with} \quad |\overline{\mathcal{M}}|^2 = \frac{1}{Q^2} |\overline{\ell \cdot \mathcal{J}}|^2, \quad (6)$$

Following the introduction above, we can now write the standard form for the Lab frame differential cross section for ep or en elastic scattering as:

$$\frac{d\sigma}{d\Omega_e} = \left(\frac{d\sigma}{d\Omega} \right)_{Mott} \left\{ F_1^2(Q^2) + \tau \left[F_2^2(Q^2) + 2 (F_1(Q^2) + F_2(Q^2))^2 \tan^2 \frac{\theta_e}{2} \right] \right\}, \quad (7)$$

where $\left(\frac{d\sigma}{d\Omega} \right)_{Mott}$ is now the Mott cross section for the proton, including the recoil factor $\frac{E_e}{E_{beam}} = (1 + \frac{2E_{beam}}{M} \sin^2 \frac{\theta_e}{2})^{-1}$, and given by:

$$\left(\frac{d\sigma}{d\Omega} \right)_{Mott} = \frac{\alpha^2}{4E_{beam}^2 \sin^4 \frac{\theta}{2}} \frac{E_e}{E_{beam}} \cos^2 \frac{\theta}{2}. \quad (8)$$

Eq. (7) is the most general form, as required by Lorentz invariance, symmetry under space reflection and charge conservation. Experimentally, the first separate values for F_1 and F_2 were obtained by the intersecting ellipse method described by Hofstadter [Hof60]. The early data of Bumiller *et al.* [Bum60] showed that F_2 decreased with q^2 faster than F_1 , even suggesting a diffractive behavior for the proton cross section. Typically these results show F_1/F_2 -ratio values which are several times larger than modern values for the proton.

2.1.2 The electric and magnetic form factors

Another set of nucleon FFs, F_{ch} and F_{mag} , was first introduced by Yennie, Levy and Ravenhall [Yen57]; Ernst, Sachs and Wali [Ern60] connected F_{ch} and F_{mag} to the charge and current distributions in the nucleon; the interpretation that F_{ch} and F_{mag} measure the interaction with static charge and magnetic fields was given by Walecka [Wal59]. The following form FFs, F_{ch} and F_{mag} , were defined in Ref. [Ern60]:

$$F_{ch} = F_1 - \frac{Q^2}{2M} F_2 \quad \text{and} \quad F_m = \frac{1}{2M} F_1 + F_2. \quad (9)$$

A similar definition of FFs for charge and magnetization, G_E and G_M , which is the one in use today, was first discussed extensively by Hand, Miller and Wilson [Han63] who noted that with:

$$G_E = F_1 - \tau F_2, \quad \text{and} \quad G_M = F_1 + F_2, \quad (10)$$

where $\tau = Q^2/4M^2$, the scattering cross section in Eq. (7) can be written in a much simpler form, without interference term, leading to a simple separation method for G_{Ep}^2 and G_{Mp}^2 :

$$\frac{d\sigma}{d\Omega} = \left(\frac{\alpha}{2E \sin(\frac{\theta_e}{2})} \right)^2 \frac{E_e}{E_{beam}} \left(\frac{\cot^2(\frac{\theta_e}{2})}{1 + \tau} [G_E^2 + \tau G_M^2] + 2\tau G_M^2 \right), \quad (11)$$

G_{Ep} , G_{Mp} , G_{En} and G_{Mn} are now customarily called the electric- and magnetic Sachs FFs, for the proton and neutron, respectively; at $Q^2=0$ they have the static values of the charge and magnetic moments, of the proton and neutron, respectively:

$$\begin{aligned} G_{Ep}(0) &= 1, & G_{Mp}(0) &= \mu_p, \\ G_{En}(0) &= 0, & G_{Mn}(0) &= \mu_n. \end{aligned}$$

2.1.3 Isovector and isoscalar nucleon form factors

In the theoretical analysis of nucleon form factors, it is often convenient to consider combinations of nucleon electromagnetic FFs which correspond to a good isospin states. In this way, one defines isoscalar (F_i^S) and isovector (F_i^V) Dirac ($i = 1$) and Pauli ($i = 2$) FFs, which are obtained from the corresponding proton and neutron FFs as:

$$\begin{aligned} F_i^S &= F_{ip} + F_{in}, \\ F_i^V &= F_{ip} - F_{in}. \end{aligned} \tag{12}$$

Their values at $Q^2 = 0$ are given by : $F_1^S(0) = 1$, $F_1^V(0) = 1$, $F_2^S(0) = -0.12$, $F_2^V(0) = 3.70$ (nuclear magnetons).

Analogously, one can define isoscalar and isovector Sachs electric FFs as :

$$\begin{aligned} G_E^S &= G_{Ep} + G_{En}, \\ G_E^V &= G_{Ep} - G_{En}, \end{aligned} \tag{13}$$

and likewise for the Sachs magnetic FF.

2.1.4 Form factors in the Breit frame

The physical meaning of the electric and magnetic form factors, G_E and G_M , is best understood when the hadronic current is written in the Breit frame. In that frame the scattered electron transfers momentum \vec{q}_B but no energy ($\omega_B=0$). Therefore, the proton likewise undergoes only a change of momentum, not of energy, from $-\vec{q}_B/2$ to $+\vec{q}_B/2$; thus $Q^2 = q_B^2$. The four components of the hadronic current in the Breit frame are:

$$J^0 = ie2m\chi'^\dagger\chi(F_1 - \tau\kappa F_2) = ie2M\chi'^\dagger\chi G_E, \tag{14}$$

$$\vec{J} = -e\chi'^\dagger(\vec{\sigma} \times \vec{q}_B)\chi(F_1 + \kappa F_2) = -e\chi'^\dagger(\vec{\sigma} \times \vec{q}_B)\chi G_M. \tag{15}$$

Only in the Breit frame can the electric and magnetic FFs G_E and G_M be associated with charge and magnetic current density distributions through a Fourier transformation. Given the artificiality of the Breit frame - there is a Breit frame for each Q^2 value- and the fact that for Q^2 -values larger than few GeV^2 , the Breit frame moves with relativistic velocities in the laboratory, a discussion in terms of charge and magnetic current densities is not valid. A model dependent procedure to transform these distributions from the Breit- to the Lab frame has, however, been recently developed by Kelly [Kel02], with interesting results to be discussed later in section 4.3.

2.2 Rosenbluth form factor separation method

The Rosenbluth method has been the only technique available to obtain separated values for G_E^2 and G_M^2 for proton and neutron until the 1990s. The method requires measuring the cross section for eN scattering at a number of electron scattering angles, for a given value of Q^2 ; this is obtained by varying both the beam energy and the electron scattering angle over as large a range as experimentally feasible.

The cross section for ep scattering in Eq. (7), when written in terms of the electric- and magnetic FFs, G_E and G_M , takes the following form:

$$\frac{d\sigma}{d\Omega} = \left(\frac{d\sigma}{d\Omega} \right)_{Mott} \times \left(G_E^2 + \tau \left[1 + 2(1 + \tau) \tan^2 \frac{\theta}{2} \right] G_M^2 \right) / (1 + \tau), \quad (16)$$

and in the notation preferred today, this cross section can be re-written as:

$$\frac{d\sigma}{d\Omega} = \left(\frac{d\sigma}{d\Omega} \right)_{Mott} \times \left[G_E^2 + \frac{\tau}{\epsilon} G_M^2 \right] / (1 + \tau), \quad (17)$$

where $\epsilon = [1 + 2(1 + \tau) \tan^2 \frac{\theta}{2}]^{-1}$ is the virtual photon polarization.

In early versions of the Rosenbluth separation method for the proton, a correspondingly defined reduced cross section was plotted either as a function of $\cot^2 \frac{\theta_e}{2}$ [Han63, Wil64] or $\cos \theta_e$ [Ber71]. For example in Ref. [Han63], the following function was defined:

$$R(Q^2, \theta_e) = [G_{Ep}^2 + \tau G_{Mp}^2] \cot^2 \frac{\theta_e}{2} + \tau(1 + \tau) G_{Mp}^2. \quad (18)$$

In 1973 Bartel *et al.* chose a form linear in $\cos \frac{\theta_e}{2}$, namely $\cos^2 \frac{\theta_e}{2} \times \left(\frac{d\sigma}{d\Omega} \right) / \left(\frac{d\sigma}{d\Omega} \right)_{Mott}$ [Bar73]. Neither of these linearization procedures fully disentangles G_{Ep}^2 and G_{Mp}^2 .

The modern version of the Rosenbluth separation technique takes advantage of the linear dependence in ϵ of the FFs in the reduced cross section based on Eq. (17) and is defined as follows:

$$\left(\frac{d\sigma}{d\Omega} \right)_{reduced} = \frac{\epsilon(1 + \tau)}{\tau} \left(\frac{d\sigma}{d\Omega} \right)_{exp} / \left(\frac{d\sigma}{d\Omega} \right)_{Mott} = G_M^2 + \frac{\epsilon}{\tau} G_E^2. \quad (19)$$

A fit to several measured reduced cross section values at the same Q^2 , but for a range of ϵ -value, gives independently $\frac{1}{\tau} G_{Ep}^2$ as the slope and G_{Mp}^2 as the intercept, as shown in Fig. 3; the data displayed in this figure are taken from Ref. [And94].

2.2.1 Proton form factor measurements

Figure 4 shows all Rosenbluth separation results performed in the 1970's as the ratio $\mu_p G_{Ep} / G_{Mp}$; it is noteworthy that these results strongly suggest a decrease of the ratio with increasing Q^2 , a fact noted in all three references [Ber71, Bar73, Han73]. As will be seen in section 3.5, the slope of this decrease is about half the one found in recent recoil polarization experiments, except for the data of Ref. [Han73], which is statistically compatible with the new polarization data. Left out of this figure are the data of Litt *et al.* [Lit70], the first of a series of SLAC experiments which were going to lead to the concept of “scaling” based on Rosenbluth separation results, namely the empirical relation $\mu_p G_{Ep} / G_{Mp} \sim 1$. Predictions of the G_{Ep} / G_{Mp} ratio made in

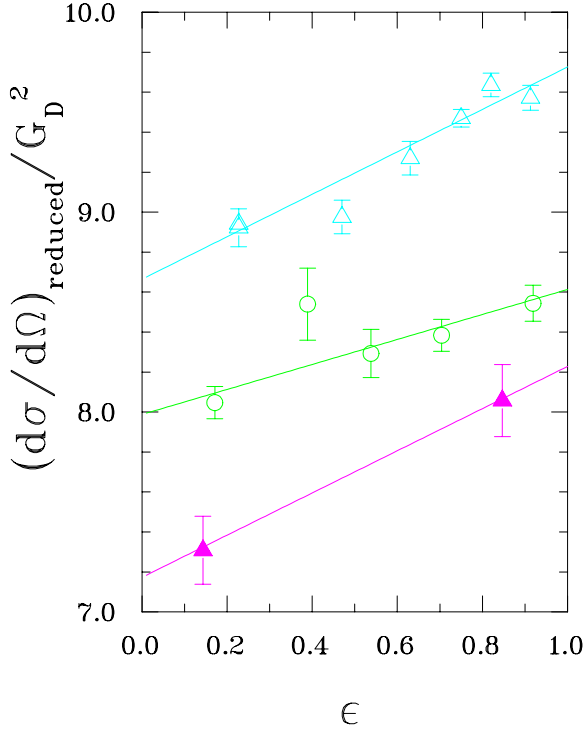


Figure 3: Demonstration of the Rosenbluth separation method based on the data from Ref. [And94]. The Q^2 values shown are 2.5 (open triangle), 5.0 (circle) and 7.0 (filled triangles) GeV^2 .

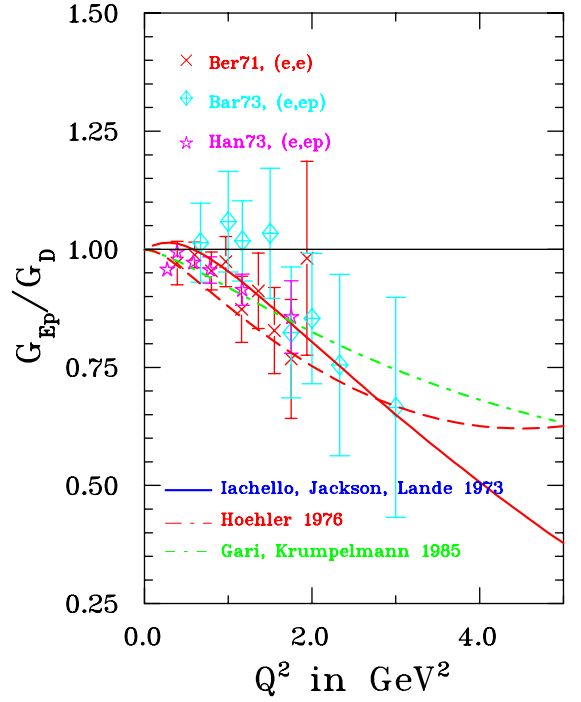


Figure 4: Early Rosenbluth separation data for G_{Ep} , up to 1973 [Ber71, Bar73, Han73], but not including the 1970 SLAC experiment of Litt et al [Lit70].

the same period and shown in Fig. 4 are from Refs. [Iac73, Hoh76, Gar85], all based on a dispersion relation description of the FFs, and related to the vector meson dominance model (VMD).

A compilation of all G_{Ep} and G_{Mp} data obtain by the the Rosenbluth separation technique is shown in Figs. 5 and 6; in these two figures both G_{Ep} and G_{Mp} have been divided by the dipole FF G_D given by Eq. (23). It is apparent from Fig. 5 that the cross section data have lost track of G_{Ep} above $Q^2 \sim 1$. In sharp contrast with the situation for G_{Ep} , the $G_{Mp}/\mu_p G_D$ ratios shown in Fig. 6 display excellent internal consistency, up to $Q^2=30 \text{ GeV}^2$, for the G_{Mp} -values obtained from cross section data; note that the large Q^2 -data in Ref. [Arn86] were obtained without Rosenbluth separation, with the assumption that $G_{Ep} = G_{Mp}/\mu_p$; the ratio $G_{Mp}/\mu_p G_D$ becomes distinctly smaller than 1 above $\sim 5 \text{ GeV}^2$.

It is difficult to obtain G_E^2 for large Q^2 values by Rosenbluth separation from ep cross section data for several reasons; first, the factor $\frac{1}{\tau}$ multiplying G_E^2 in Eq. (19) automatically reduces the contribution of this term to the cross section as Q^2 increases; and second, even at small Q^2 , $G_M^2 \sim \mu_p^2 G_E^2$, hence the contribution of G_E^2 to the cross section is reduced by a factor 7.80.

It was first observed by Arnold et al [Arn86] that the proton magnetic FF, G_{Mp} follows the pQCD prediction of Brodsky and Farrar [Bro75], as illustrated in Fig. 7; the pQCD prediction is based on quark counting rules. Indeed $Q^4 G_{Mp}$ becomes nearly constant starting at $Q^2=8 \text{ GeV}^2$. However, the $1/Q^4$ -behavior of the proton magnetic form fact was first mentioned by Coward *et al.* [Cow68], based on their data extending to 20

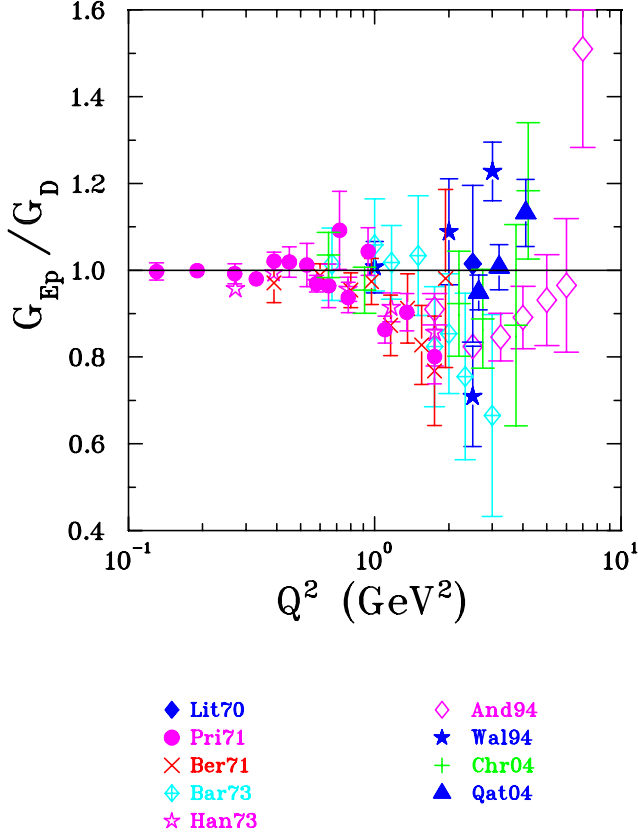


Figure 5: Data base for G_{Ep} obtained by the Rosenbluth separation method; the references are [Lit70, Pri71, Ber71, Bar73, Han73, And94, Wal94, Chr04, Qat04].

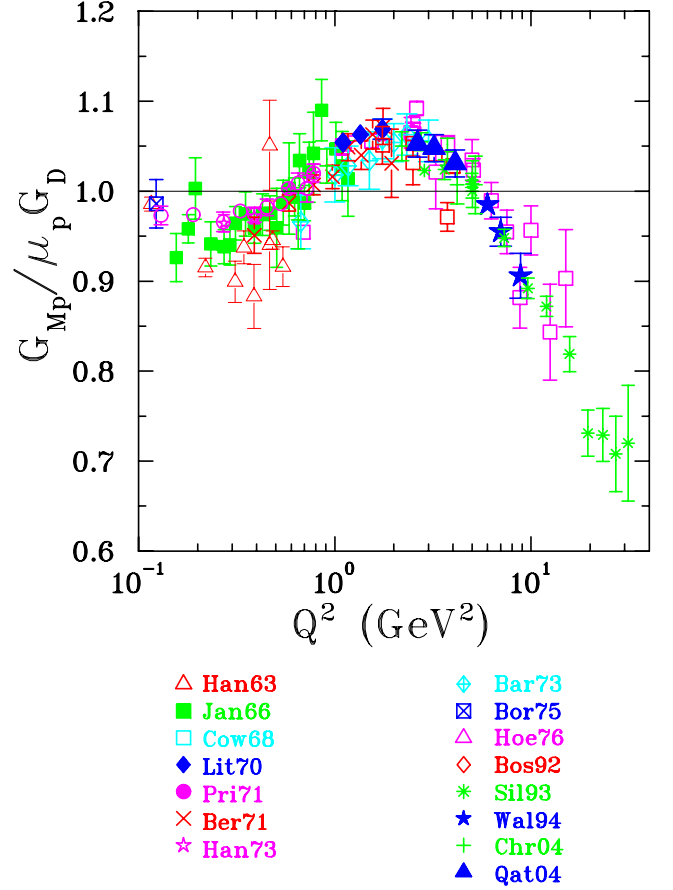


Figure 6: Data base for G_{Mp} obtained by the Rosenbluth; the references are [Han63, Jan66, Cow68, Lit70, Pri71, Ber71, Han73, Bar73, Hoh76, Arn86, Wal94, Chr04, Qat04].

GeV^2 ; these authors discussed the $1/Q^4$ behavior in light of the vector meson exchange prevailing at the time [Schw67].

2.2.2 Neutron electric form factor measurements

The “neutrality” of the neutron requires the electric form factor to be zero at $Q^2=0$, and small at non-zero Q^2 ; historically, the fact that the electric FF is non-zero has been explained in terms of a negatively charged pion cloud in the neutron, which surrounds a small positive charge [Fer47].

Early attempts to determine the neutron FF were based on measurements of the elastic ed cross section. The scattering by an electron from the spin 1 deuteron requires 3 FFs in the hadronic current operator, for the charge, quadrupole and magnetic distributions, G_C , G_Q and G_M , respectively. In the original, impulse approximation (IA) form of the cross section developed by Gourdin [Gou64], the elastic ed cross section is:

$$\frac{d\sigma}{d\Omega} = \frac{d\sigma}{d\Omega_{Mott}} \left(A(Q^2) + B(Q^2) \tan^2\left(\frac{\theta_e}{2}\right) \right), \quad (20)$$

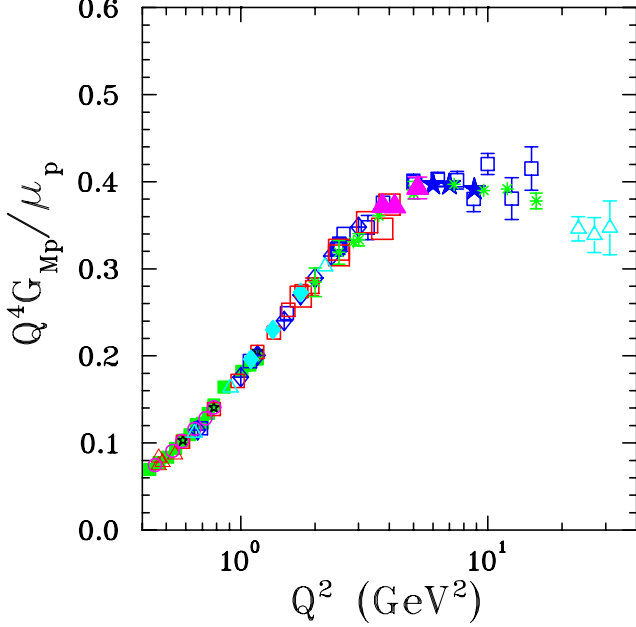


Figure 7: The G_{Mp} data follow the pQCD scaling law, $G_{Mp} \propto \frac{1}{Q^4}$, as was first demonstrated in Arnold *et al.* [Arn86]; the data shown are the same as in Fig. 6

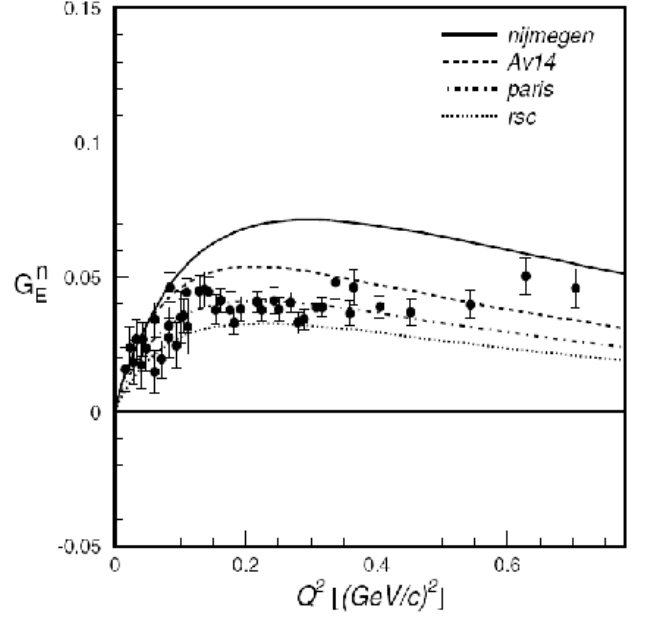


Figure 8: The 1990 Platchkov data [Pla90] for G_{En} , with various fits; this Fig. taken from Ref. [Pla90]

where $A(Q^2) = G_C^2(Q^2) + \frac{8}{9}\eta^2 G_Q^2(Q^2) + \frac{2}{3}\eta(1+\eta)G_M^2(Q^2)$ and $B(Q^2) = \frac{3}{4}\eta(1+\eta)^2 G_M^2(Q^2)$, with $\eta = Q^2/4M_D^2$. The charge, quadrupole and magnetic FFs can be written in terms of the iso-singlet electric and magnetic FFs as defined in Eq. (13) as follows:

$$G_C = G_E^S C_E, \quad G_Q = G_E^S C_Q \quad \text{and} \quad G_M = \frac{M_D}{M_p}(G_M^S C_S + \frac{1}{2}G_E^S C_L),$$

where the coefficients C_E, C_Q, C_L and C_S are Fourier transforms of specific combinations of the S- and D-state deuteron wave function, $u(r)$ and $w(r)$ [Gou64].

The 1971 DESY experiment of Galster *et al.* [Gal71] measured elastic ed cross sections up to 0.6 GeV² with reasonable accuracy and provided a good data base for the extraction of G_{En} ; it had been preceded by a series of experiments started at the Stanford MARK III accelerator, including McIntyre and Dahl [McI57], Friedman, Kendall and Gram [Fri60], Drickey and Hand [Dri62], Benaksas, Drickey and Grossetete [Ben64], and Grossetete, Drickey and Lehmann [Gro66a]. Analyzing all of these data, and using Hamada-Johnston [Ham62] and Lomon-Feshbach [Fes67] deuteron wave functions, it was concluded in Ref. [Gal71] that G_{En} could be fitted well with the form:

$$G_{En}(Q^2) = -\frac{\mu_n}{1 + 5.6\tau} G_{Ep}(Q^2). \quad (21)$$

The often quoted Galster fit uses Eq. (21) with G_{Ep} replaced by the dipole FF G_D (see Eq. (23)).

The next and last experiment to measure the elastic ed cross section to determine G_{En} is that of Platchkov *et al.* [Pla90]. These data extend to Q^2 of 0.7 GeV², with significantly smaller statistical uncertainties than all

previous experiments. The data from Platchkov *et al.* [Pla90] are shown in Fig. 8. In this range of Q^2 , $A(Q^2)$ is very sensitive to the deuteron wave function, and therefore to the NN interaction. Furthermore, the shape of $A(Q^2)$ cannot be explained by the IA alone. Corrections beyond the IA including final state interaction (FSI) and meson exchange currents (MEC) were found to significantly improve the agreement between calculations and the shape of $A(Q^2)$ observed. The authors suggest a modified form of the Galster fit using several NN potentials, and including MEC as well as relativistic corrections, of the form;

$$G_{En}(Q^2) = -a \frac{\mu_n}{1 + b\tau} G_{Ep}(Q^2). \quad (22)$$

For the Paris NN potential for example, $a=1.25$ and $b=18.3$; this fit will be compared with the double-polarization data shown later in this review, in Fig. 20. Starting in 1994 all G_{En} measurements have used either polarization transfer or beam-target asymmetry to take advantage of the interference nature of these observables: terms proportional to $G_{En}G_{Mn}$ are measured, instead of the G_{En}^2 contribution to the cross section; these experiments will be reviewed in section 3.3.

2.2.3 Neutron magnetic form factor measurements

In an early experiment Hughes *et al.* [Hug65] performed a Rosenbluth separation of quasi elastic $d(e, e')$ cross sections in the range $Q^2=0.04$ to 1.17 GeV^2 ; they observed non-zero values of G_{En} only below 0.2 GeV^2 but measured G_{Mn} up to 1.17 GeV^2 ; the technique consisted in comparing quasi-elastic ed - with elastic ep cross sections. The several experiments following Hughes' can be subdivided into 3 groups: cross section measurements in quasi-elastic ed scattering (single arm) [Gro66b, Han73, Bar73], which requires large final state interaction (FSI) corrections at small Q^2 ; elastic ed cross section measurements [Ben64, Gro66a]; and cross section measurements in $^2H(e, e'p)^1H$ [Bud68, Dun66], or ratio of cross sections $^2H(e, e'n)^2H/{}^2H(e, e'p)^1H$ [Ste66, Bro05b], which is less sensitive to the deuteron wave function, FSI and MEC.

All results published prior to 1973 are displayed in Fig. 9, to be compared with the proton data from the same period in Fig. 4. All more recent cross section results are in Fig. 10, allowing for a comparison of the progress made in this period for the neutron. In Fig. 10 all G_{Mn} data obtained from cross section measurements are displayed, including the SLAC experiments [Roc82, Lun93], which measured inclusive quasi-elastic ed cross sections. The more recent NIKHEF [Bru95] and Mainz [Ank94, Ank98, Kub02] experiments are simultaneous measurements of the cross section for quasi elastic scattering on the neutron and proton in the deuteron, $^2H(e, e'n)^1H$ and $^2H(e, e'p)^1H$; the systematics is then dominated by the uncertainty in the neutron detector efficiency; much attention was given to that calibration in these experiments. In the NIKHEF experiment [Bru95] protons and neutrons were detected in the same scintillator, and the neutron efficiency was determined *in situ* with the neutrons from $^1H(\gamma, \pi)$. It has been argued in [Jou97] that 3-body electro-production contributes significantly and does not necessarily lead to a neutron at the 2-body kinematic angle; these data points are shown as \diamond in Fig.10; a refutation of these arguments is in [Bru97]. In the Mainz experiments the dedicated neutron detector was calibrated in a neutron beam at SIN. The new data from Hall B at JLab, Ref. [Bro05b] are shown as filled triangles in Fig. 10; for these data from Hall B, in addition to the measurements of cross section ratio with the 2H target, an in-line 1H target was used for an in-situ determination of the neutron counter efficiency via π^+ electro-production.

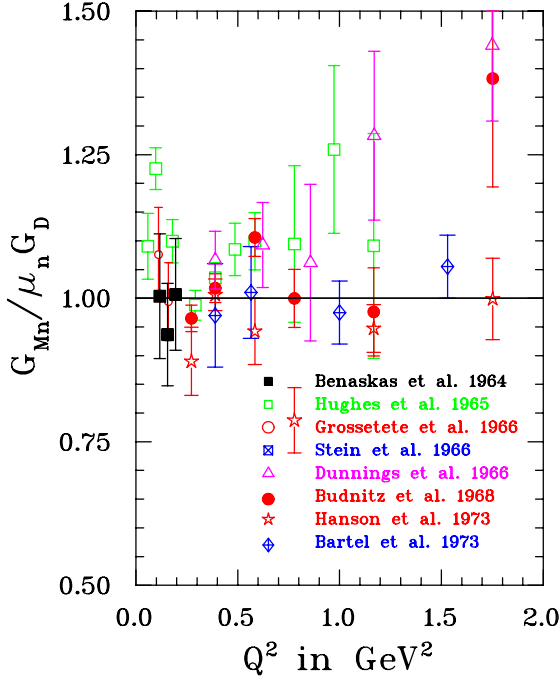


Figure 9: Early Rosenbluth separation data for G_{Mn} , up to 1973 [Ben64, Hug65, Gro66b, Ste66, Dun66, Bud68, Han73, Bar73].

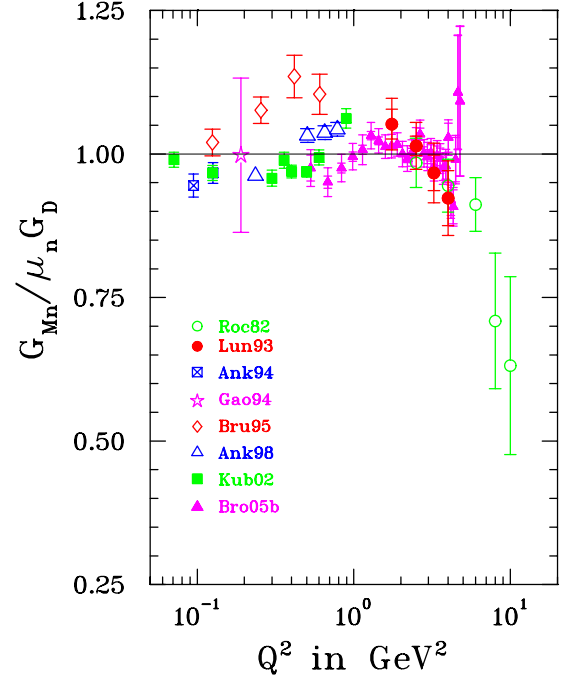


Figure 10: Recent G_{Mn} data divided by $\mu_n G_D$, from cross section data only, starting in 1982 [Roc82, Lun93, Ank94, Bru95, Ank98, Kub02, Bro05b].

2.2.4 Rosenbluth results and dipole form factor

In figures 11, 12 and 13 the Rosenbluth separation results G_{Ep} , G_{Mp} and G_{Mn} are shown in double logarithmic plots for $Q^2 < 2 \text{ GeV}^2$ (5 GeV^2 for G_{Mn}), to emphasize the excellent agreement of these data, in this Q^2 -range, with the dipole formula:

$$G_D = \frac{1}{(1 + Q^2/0.71)^2} \quad \text{with} \quad G_{Ep} = G_D, \quad G_{Mp} = \mu_p G_D \quad \text{and} \quad G_{Mn} = \mu_n G_D. \quad (23)$$

Noticeable is the lack of G_{Mp} data below Q^2 of 0.02 GeV^2 , a consequence of the dominance of the electric FF at small Q^2 for the proton, as seen in Eq. (17).

Although Hofstadter was the first to note that the proton FF data could be fitted by an “exponential model”, which corresponds to the “dipole model” for FF in momentum space, it appears that the usage of dividing data by G_D was introduced first by Goitein *et al.* [Goi67].

The possible origin of the dipole FF has been discussed in a number of early papers. Within the framework of the dispersion relation, an approximate dipole term can occur for the isovector and isoscalar parts of a FF, $G_{E,M}^{V,S} = \sum_i \frac{\alpha_i^{V,S}}{1 + Q^2/(M_i^{V,S})^2}$, where $G_{E,M}^V$, $G_{E,M}^S$ were defined previously, Eq. (13), and $M_i^{V,S}$ and $\alpha_i^{V,S}$ are the masses and residua of the isovector-, isoscalar mesons, respectively.

Within the model of a general conserved four-vector current operator, Barut *et al.* [Bar68] had shown in 1968, using constraints based on the data available at the time, that G_{Ep} could be expressed as a dipole term multiplied by a quadratic function of Q^2 ; this quadratic factor has a zero at $Q^2 \sim 3.6 \text{ GeV}^2$ (and a second zero in the time-like region); this is perhaps the first prediction that G_{Ep} might become negative at some large Q^2 .

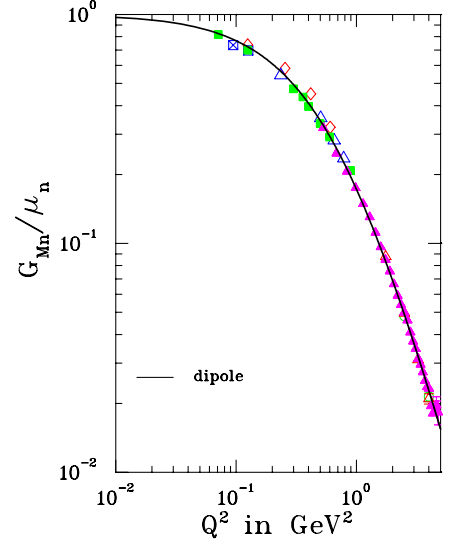
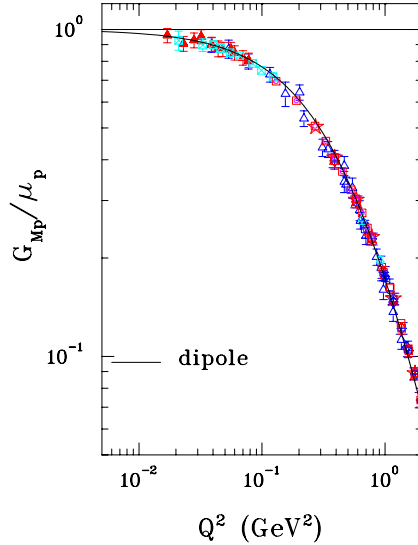
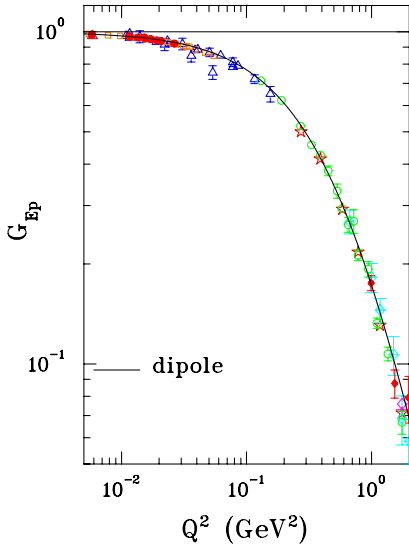


Figure 11: Illustration of the quality of the dipole fit for G_{Ep} ; the data included are from Refs. [Han63, Hoh76, Lit70, Ber71, Han73, Bar73, Mur74, Sim80, Wal94, And94, Qat04] in the range $0.005\text{--}2\text{ GeV}^2$.

Figure 12: Same as Fig. 11 for G_{Mp} ; the data of Refs. [Han63, Hoh76, Lit70, Ber71, Bar73, Wal89, Arn86] in the range $0.005\text{--}2\text{ GeV}^2$ are included here.

Figure 13: Illustration of the quality of the dipole fit for G_{Mn} ; the data included are from Refs. [Roc92, Lun93, Ank94, Bru95, Ank98, Kub02, Bro05b] in the Q^2 -range $0.07\text{--}4.8\text{ GeV}^2$.

2.3 Nucleon size

The first experiments which determined the FF $|F(q)|^2$ according to Eq. (1) are discussed in [McA56, Hof56]; these results indicated that $F^2(q)$ for the proton could be fitted equally well with an exponential as with a Gaussian charge distribution $\rho(r)$. These results led to the earliest evaluation of the root mean square charge radius, $\langle r^2 \rangle^{\frac{1}{2}} = 0.8\text{ fm}$.

The first measurement of the neutron size was reported by Yearian and Hofstadter [Yea58] in 1958. Their result for the magnetic root mean squared radius of the neutron, $\langle r_n^2 \rangle^{\frac{1}{2}}$, was $0.85 \pm 0.1\text{ fm}$; it was obtained from 6 data points for F_{2n} , from quasi-elastic ed differential cross sections, with the assumption $F_{1n}=0$, in the Q^2 -range $0.26\text{ to }0.59\text{ GeV}^2$. This result was quite surprising at the time as the early results of low energy ne -scattering, and theoretical considerations by Schiff [Schi49] and others, had led to the expectation that the charge radius of the neutron was either very small or negative.

At very small four-momentum transfer squared, the electron probes the outer region of the proton charge distribution, and the FF G_{Ep} , G_{Mp} , G_{Mn} and G_{En} can be expanded as a power series:

$$\begin{aligned} G_{Ep} &= 1 - \frac{1}{6} \langle r^2 \rangle_{Ep} Q^2 + \frac{1}{120} \langle r^4 \rangle_{Ep} Q^4 + \dots, \\ \frac{G_{MN}}{\mu_N} &= 1 - \frac{1}{6} \langle r^2 \rangle_{MN} Q^2 + \frac{1}{120} \langle r^4 \rangle_{MN} Q^4 + \dots, \text{ with } N = p \text{ or } n, \\ G_{En} &= -\frac{1}{6} \langle r^2 \rangle_{En} Q^2 + \frac{1}{120} \langle r^4 \rangle_{En} Q^4 + \dots \end{aligned}$$

where the root-mean square nucleon radius is $r_N = \sqrt{\langle r^2 \rangle_N}$. In the case of the neutron charge radius r_{En} Isgur [Isg99] has shown that an extra term present in the constituent quark model is exactly canceled by the Foldy term, restoring the usual interpretation of the FF as the Fourier transform of the charge distribution in the neutron rest frame.

nucleon	rms p	uncertainty	rms n	uncert.	Ref.
p,n	0.7-0.8*	**	0.8	**	[Hof56, Hof58]
n			0.85	0.1	[Yea58]
p,n	0.836	0.01	0.840	**	[Hoh76]
p	0.862	0.012			[Sim80]
p,n	0.847	0.01	0.889	**	[Mer96]
p	0.880	0.015			[Ros00]
p	0.871	0.012			[Pac96]
p	0.895	0.018			[Sic05]
p	0.855 [†]	**			[Bro05a]

Table 1: Time evolution of the nucleon root-mean-square radius obtained from low Q^2 data.

* First number for exponential, second for Gaussian model for $\rho(r)$.

** No uncertainty given.

[†] One of several fits

The earliest and only very accurate determination of r_p from ep -scattering at small Q^2 is based on the data of Simon *et al.* [Sim80] and produced a significantly larger r_p -value than the original Stanford analysis of [Hof56]. After the work of Ref. [Sim80] it became increasingly evident that r_p values obtained from ep -scattering must be corrected for Coulomb distortion. In particular Rosenfelder [Ros00], Pachucki [Pac96] and Sick [Sic05] have made detailed analysis of the various corrections required. At present the Coulomb-corrected value of r_p is in the range 0.880-0.895 fm, and the smallest uncertainty achievable on r_p , including the theoretical uncertainty associated with the Coulomb correction, is about 0.01 fm. A selection of value of r_p and r_n can be found Table 1.

Measurements of the Lamb shift in hydrogen currently achieve error bars for r_p similar to those in ep measurements. Recent results from Bourseix *et al.* [Bou96] quote a value of 0.862(12); these and the results of Schwobe *et al.* [Schw99] have been used by Melnikov *et al.* [Mel00] to obtain a value $r_p=0.883(14)$ after evaluation of the energy correction up to α^7 .

Potentially more accurate are the determinations of the 2S-2P splitting in muonic hydrogen. This energy split can be measured with an accuracy of 30 ppm, with a projected ability to determine r_p to 1 part in 10^{-3} ; an experiment to measure this energy split in hydrogen is under way at the Paul Scherrer Institute [Hau98].

The compatibility with the Zemach radius of the proton determining the hydrogen hyper-fine separation (HFS) has been recently revisited by Brodsky *et al.* [Bro05a] and by Friar and Sick [Fri05]. The Zemach radius determines most of the difference in the HFS in hydrogen and muonium, which is mostly due to the finite proton size, versus the point-like nature of the μ . The Zemach radius is determined by an integral over $Q = \sqrt{Q^2}$ of the product $G_{Ep}G_{Mp}$:

$$\langle r \rangle_Z = -\frac{4}{\pi} \int_0^\infty \frac{dQ}{Q^2} \left[\frac{G_{Ep}G_{Mp}}{1 + \kappa_p} - 1 \right], \quad (24)$$

and can therefore also be determined from separated elastic ep -data. In Ref. [Bro05a] the authors show that values of the Zemach radius can be obtained from the ep -data base which agree well with atomic measurements.

3 Nucleon form factors from double polarization observables

It was pointed out in 1968 by Akhiezer and Rekalov [Akh68] that “for large momentum transfers the isolation of the charge FF of the proton is difficult” using the elastic ep reaction with an unpolarized electron beam, for several reasons: one being $G_{Mp}^2/G_{Ep}^2 \geq \mu_p^2$ at any Q^2 value and the other is that at large Q^2 the contribution from the τG_{Mp}^2 term in $G_{Ep}^2 + (\tau/\epsilon)G_{Mp}^2$ increases (see Eq.(17)) and makes the separation of the charge form factor practically impossible. In the same paper the authors also pointed out that the best way to obtain the proton charge form factor is with polarization experiments, especially by measuring the polarization of the recoil proton. Further in a review paper in 1974 Akhiezer and Rekalov [Akh74] discussed specifically the interest of measuring an interference term of the form $G_E G_M$ by measuring the transverse component of the recoiling proton polarization in the $\vec{e}p \rightarrow e\vec{p}$ reaction at large Q^2 , to obtain G_E in the presence of a dominating G_M . In 1969, in a review paper Dombey [Dom69] also discussed the virtues of measuring polarization observables in elastic and inelastic lepton scattering; however his emphasis was to do these measurements with polarized lepton on polarized target. Furthermore in 1982 Arnold, Carlson and Gross emphasized that the best way to measure the electric FF of the neutron would be to use the $^2H(\vec{e}, e'\vec{n})p$ reaction. Both a polarized target, and a focal plane polarimeter (to measure recoil polarization), have been used to obtain nucleon FFs. We discuss below both methods to measure the elastic nucleon FFs, highlighting advantages and disadvantages of using polarized target and focal plane polarimeter.

3.1 Polarization transfer

Figure 14 shows the kinematical variables for the polarization transfer from a longitudinally polarized electron to a struck proton in the one-photon exchange approximation.

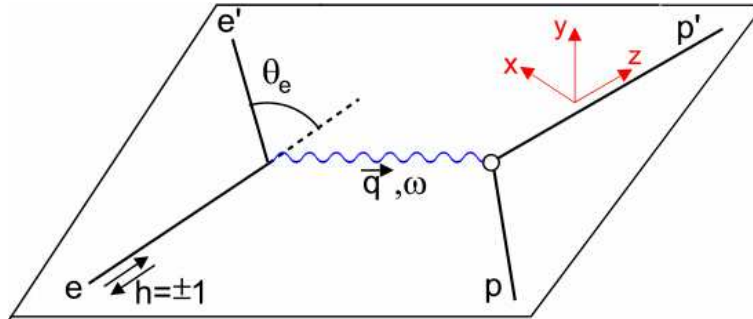


Figure 14: Kinematical variables for polarization transfer from a longitudinally polarized electron to a proton with exchange of a virtual photon.

The electron vertex in Fig. 14 can be described by basic Quantum Electrodynamics (QED) rules that involves the electron current, ℓ_μ , and the proton vertex can be described by QCD and hadron electrodynamics involving the hadronic current J^μ . The current $J^\mu = \chi^\dagger F_\mu \chi$, where $\mu = 1, 2$, has simple relations to the electric and magnetic nucleon form factor FFs in the Breit frame as given by Eq. (15).

For elastic ep scattering with longitudinally polarized electrons, the hadronic tensor, $W_{\mu\nu} = J_\mu J_\nu^*$, has four possible terms depending upon the polarization of the target and of the recoil proton:

$$W_{\mu\nu} = W_{\mu\nu}^{(o)} + W_{\mu\nu}(\mathbf{P}_1) + W_{\mu\nu}(\mathbf{P}_2) + W_{\mu\nu}(\mathbf{P}_1, \mathbf{P}_2), \quad (25)$$

where the first term in the equation corresponds to unpolarized protons, the second and the third term correspond to the vector polarization of the initial and the final proton, respectively, and the last term describes the reaction when both, the initial and the final protons are polarized.

When we consider the case where only the polarization of the final proton is measured, we get the following expression for $W_{\mu\nu}(\mathbf{P})$:

$$W_{\mu\nu}(\mathbf{P}) = \frac{1}{2} \text{Tr} F_\mu F_\nu^\dagger \vec{\sigma} \cdot \mathbf{P}, \quad (26)$$

where $F_\mu = 2mG_E$, for $\mu = 0$ and $F_\mu = i\sigma \times \mathbf{q}_B mG_M$, for $\mu = x, y, z$. For the scattering of longitudinally polarized electrons off an unpolarized target, in the one-photon exchange approximation, there are only two non-zero polarization components, transverse, P_x , and longitudinal, P_z ; and these components are obtained by calculating the tensors $W_{\mu\nu}(P_x) = \frac{1}{2} \text{Tr} F_\mu F_\nu^\dagger \sigma_x \sim 2mG_E G_M$ and $W_{\mu\nu}(P_z) = \frac{1}{2} \text{Tr} F_\mu F_\nu^\dagger \sigma_z \sim G_M^2$. Then one can find the expressions [Akh74, Arn81] for the polarization components P_x and P_z in terms of the electric FF G_E , and magnetic, G_M ; for 100 % longitudinally incident polarized electrons, the proton polarization components are :

$$I_0 P_x = -2\sqrt{\tau(1+\tau)} G_E G_M \tan \frac{\theta_e}{2} \quad (27)$$

$$I_0 P_z = \frac{1}{M} (E_e + E_{e'}) \sqrt{\tau(1+\tau)} G_M^2 \tan^2 \frac{\theta_e}{2}, \quad (28)$$

where E_e and $E_{e'}$ are the energy of the incident and scattered electrons, respectively, θ_e is the scattered electron angle in the laboratory frame, and I_0 is:

$$I_0 = G_E^2(Q^2) + \tau G_M^2(Q^2) [1 + 2(1+\tau) \tan^2 \frac{\theta_e}{2}]. \quad (29)$$

Eqs. (27) and (28) show that the transverse and longitudinal polarization components are proportional to $G_E G_M$ and G_M^2 , respectively. The ratio G_E/G_M then can be obtained directly from the ratio of the two polarization components P_x and P_z as follows:

$$\frac{G_E}{G_M} = -\frac{P_x}{P_z} \frac{(E_e + E_{e'})}{2M} \tan\left(\frac{\theta_e}{2}\right). \quad (30)$$

Equation (30) makes clear that this method offers several experimental advantages over the Rosenbluth separation: (1) for a given Q^2 , only a single measurement is necessary, if the polarimeter can measure both components at the same time. This greatly reduces the systematic errors associated with angle and beam energy change, and (2) the knowledge of the beam polarization and of the analyzing power of the polarimeter is not needed to extract the ratio, G_E/G_M .

3.2 Asymmetry with polarized targets

It was first pointed out by Dombey [Dom69] that the nucleon FFs can be extracted from the scattering of longitudinally polarized electrons off a polarized nucleon target. In the one photon exchange approximation,

following the approach of Donnelly and Raskin [Don86, Ras86], the elastic $e - N$ cross section can be written as a sum of an unpolarized part and a polarized part; the latter is non-zero only if the electron beam is longitudinally polarized:

$$\sigma^{pol} = \Sigma + h\Delta, \quad (31)$$

where h is the electron beam helicity, Σ is the elastic un-polarized cross section given by Eq. (17), and Δ is the polarized part of the cross section with two terms related to the directions of the target polarization. The expression for Δ can be written as [Don86, Ras86]:

$$\Delta = -2\sigma_{Mott} \tan(\theta_e/2) \sqrt{\frac{\tau}{1+\tau}} \left\{ \sqrt{\tau[1 + (1+\tau) \tan^2(\theta_e/2)]} \cos \theta^* (G_M)^2 + \sin \theta^* \cos \phi^* G_E G_M \right\}, \quad (32)$$

where θ^* and ϕ^* are the polar and azimuthal laboratory angles of the target polarization vector with \vec{q} in the \vec{u}_z direction and \vec{u}_y normal to the electron scattering plane, as shown in Figure 15.

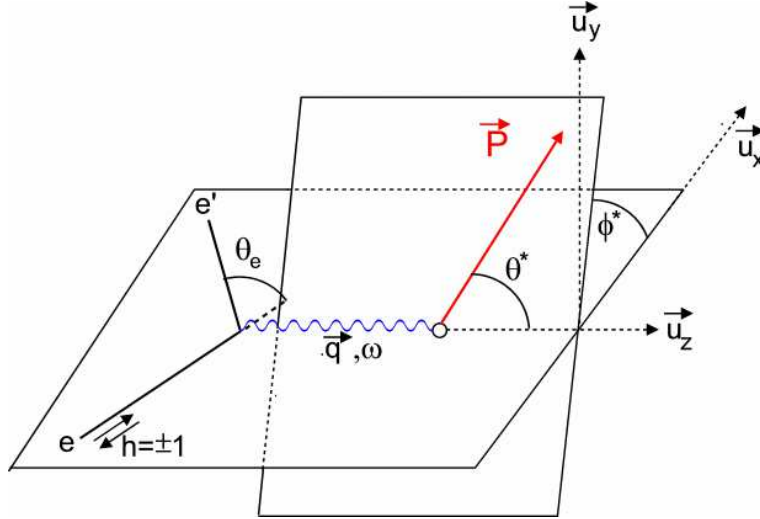


Figure 15: Polarized electron scattering from a polarized target.

The physical asymmetry A is then defined as

$$A = \frac{\sigma_+ - \sigma_-}{\sigma_+ + \sigma_-} = \frac{\Delta}{\Sigma}, \quad (33)$$

where σ_+ and σ_- are for the two beam helicities.

For a polarized target, the measured asymmetry, A_{meas} , is related to the physical asymmetry A by

$$A_{meas} = P_{beam} P_{target} A, \quad (34)$$

where P_{beam} and P_{target} are electron beam- and target polarization, respectively, and the physical asymmetry A is,

$$A = -\frac{2\sqrt{\tau(1+\tau)} \tan(\theta_e/2) \sin \theta^* \cos \phi^* G_E G_M}{(G_E)^2 + \tau [1 + 2(1+\tau) \tan^2(\theta_e/2)] (G_M)^2} - \frac{2\sqrt{\tau(1+\tau)} \{ \sqrt{\tau [1 + (1+\tau) \tan^2(\theta_e/2)]} \cos \theta^* (G_M)^2}{(G_E)^2 + \tau [1 + 2(1+\tau) \tan^2(\theta_e/2)] (G_M)^2}. \quad (35)$$

It is evident from Eq. (35) that to extract G_E , the target polarization in the laboratory frame must be perpendicular with respect to the momentum transfer vector \vec{q} and within the reaction plane, with $\theta^* = \pi/2$ and $\phi^* = 0^\circ$ or 180° . For these conditions, the asymmetry A in Eq. (35) simplifies to:

$$A_{perp} = \frac{-2\sqrt{\tau(1+\tau)} \tan(\theta_e/2) \frac{G_E}{G_M}}{\frac{(G_E)^2}{(G_M)^2} + \tau [1 + 2(1+\tau) \tan^2(\theta_e/2)]}. \quad (36)$$

As G_E^2/G_M^2 is quite small, A_{perp} is approximately proportional to G_E/G_M . Also, the second term in Eq. (35) is not strictly zero due to finite acceptance of detectors, but these effects are small and depend on kinematics only in first order and can be corrected for, so the ratio G_E/G_M is not affected directly.

The discussion described above is only applicable to a free nucleon; corrections are required if nuclear targets, like 2H or 3He , are used instead in quasi-elastic scattering to obtain the FFs.

3.3 Double polarization experiments

The polarization method, using polarized targets and focal plane polarimeter with longitudinally polarized electron beam, has been used to measure both the proton and the neutron electromagnetic FFs. Below we first describe the polarization experiments that measured the proton FFs and next those that measured the neutron FFs.

3.3.1 Proton form factors from polarization experiments

The first experiment to measure the proton polarization observable in ep elastic scattering was done at the Stanford Linear Accelerator Center (SLAC) by Alguard *et al.* [Alg76]. They measured the anti-parallel-parallel asymmetry in the differential cross sections by scattering longitudinally polarized electrons on polarized protons. From their result they concluded that the signs of G_{Ep} and G_{Mp} are the same; they also mentioned in their conclusion that the usefulness of using polarized beam on polarized target is severely limited by low counting rates.

Next, the recoil polarization method to measure the proton electromagnetic FF was used at MIT-Bates laboratory [Mil98, Bar99]. In this experiment the proton FF ratio G_{Ep}/G_{Mp} was obtained for a free proton and a bound proton in a deuterium target at two Q^2 values, 0.38 and 0.5 GeV^2 using polarization transfer from longitudinally polarized electron to the proton in the target, and measuring the polarization of the recoiling proton with a focal plane polarimeter (FPP). The conclusion from these measurements was that the polarization transfer technique showed great promise for future measurements of G_{Ep} and G_{En} at higher Q^2 values.

The ratio G_{Ep}/G_{Mp} in the elastic reaction $^1H(\vec{e}, e'\vec{p})$ reaction was also measured at the Mainz Microtron (MAMI) in a dedicated experiment [Pos01], and also as a calibration measurement [Die01] at a Q^2 of ≈ 0.4

GeV². They found a ratio value in agreement with other polarization measurements as well as Rosenbluth measurements.

Starting in late 1990's, the proton FF ratios G_{Ep}/G_{Mp} were measured in two successive dedicated experiments in Hall A at JLab for Q^2 from 0.5 to 5.6 GeV² [Jon00, Gay02, Pun05]. Other measurements were also conducted in Hall A [Gay01, Str03, Hu06] at lower Q^2 values, as calibration measurements for other polarization experiments, and one measurement in Hall C [MacL06].

In the first JLab experiment the ratio, G_{Ep}/G_{Mp} , was measured up to Q^2 of 3.5 GeV² [Jon00, Pun05]. Protons and electrons were detected in coincidence in the two high-resolution spectrometers (HRS) of Hall A [Alc04]. The polarization of the recoiling proton was obtained from the asymmetry of the azimuthal distribution after the proton re-scattered in a focal plane polarimeter using a graphite analyzer.

The ratio, G_{Ep}/G_{Mp} , was measured at $Q^2 = 4.0, 4.8$ and 5.6 GeV² with an overlap point at $Q^2 = 3.5$ GeV² [Gay02], in the second JLab experiment. To extend the measurement to higher Q^2 , two changes were made from the first experiment. First, to increase the figure-of-merit (FOM) of the FPP, a CH₂ analyzer was used instead of graphite; hydrogen has much higher analyzing power [Spi83, Mil77] than carbon [Che95] (see Fig. 22). Second, the thickness of the analyzer was increased from 50 cm of graphite to 100 cm of CH₂ to increase the fraction of events with a second scattering in the analyzer. Third, the electrons were detected in a lead-glass calorimeter with a large frontal area, to achieve complete solid angle matching with the HRS detecting the proton. At the largest Q^2 of 5.6 GeV² the solid angle of the calorimeter was 6 times that of the HRS.

Proton polarimeters are based on nuclear scattering from an analyzer material like graphite or CH₂; the proton-nucleus spin-orbit interaction results in an azimuthal asymmetry in the scattering distribution which can be analyzed to obtain the proton polarization. The detection probability for a proton scattered by the analyzer with polar angle ϑ and azimuthal angle φ is given by:

$$f^\pm(\vartheta, \varphi) = \frac{\epsilon(\vartheta, \varphi)}{2\pi} \left(1 \pm A_y(P_x^{fpp} \sin \varphi - P_y^{fpp} \cos \varphi) \right). \quad (37)$$

where \pm refers to the sign of the beam helicity, P_x^{fpp} and P_y^{fpp} are transverse and normal polarization components in the reaction plane at the analyzer, respectively, and $\epsilon(\vartheta, \varphi)$ is an instrumental asymmetry that describes non-uniformities in detector response that might result from misalignments of the FPP tracking detectors or from inhomogeneities in detector efficiency. Physical asymmetries are obtained from the difference distribution of f^\pm ,

$$D_i = (f_i^+ - f_i^-)/2 = \frac{1}{2\pi} \left(A_y P_t^{fpp} \sin \varphi_i - A_y P_n^{fpp} \cos \varphi_i \right), \quad (38)$$

and the sum distribution of f^\pm separates the instrumental asymmetries,

$$E_i = (f_i^+ + f_i^-)/2 = \frac{\epsilon_i}{2\pi}. \quad (39)$$

The values of the two asymmetries at the FPP, $A_y P_x^{fpp}$ and $A_y P_y^{fpp}$, can be obtained by doing a Fourier analysis of the difference distribution D_i ; however to calculate the ratio G_{Ep}/G_{Mp} , the proton polarization components P_x and P_z are needed at the target.

As the proton travels from the target to the focal plane through the magnetic elements of the HRS, its spin precesses, and therefore the polarization components at the FPP and at the target are different. The hadron HRS in Hall A consists of three quadrupoles and one dipole with shaped entrance and exit edges, as well as a

radial field gradient. The polarization vectors at the polarimeter, \vec{P}^{fpp} , are related to those at the target, $h\vec{P}$, through a 3-dimensional rotation matrix, (S) , as follows:

$$\begin{pmatrix} P_y^{fpp} \\ P_x^{fpp} \\ P_z^{fpp} \end{pmatrix} = \begin{pmatrix} S_{yy} & S_{yx} & S_{yz} \\ S_{xy} & S_{xx} & S_{xz} \\ S_{zy} & S_{zx} & S_{zz} \end{pmatrix} \begin{pmatrix} P_y \\ P_x \\ P_z \end{pmatrix}$$

The spin transport matrix elements S_{ij} can be calculated using a model of the HRS with quadrupoles, fringe fields, and radial field gradient in the dipole, for each tuning of the spectrometer setting, and event by event with the differential-algebra-based transport code COSY [Ber95]. The spin transport method to obtain the two asymmetries at the target, $hA_y P_x$ and $hA_y P_z$, was developed by Pentchev and described in detail in Ref. [Pen03], and also discussed in Ref. [Pun05]. The ratio G_{Ep}/G_{Mp} was calculated from the two asymmetries at the target from Eq. (30). The fact that both beam polarization, and polarimeter analyzing power cancel out of this equation contributes to the reduction of the systematic uncertainties, however their values do influence the statistical errors.

The most recent acquisition of the FF ratio G_{Ep}/G_{Mp} has been made at a Q^2 of 1.51 GeV² by measuring the beam-target asymmetry in an experiment in Hall C at JLab in elastic ep scattering [Jon06]. This is the highest Q^2 at which the G_{Ep}/G_{Mp} ratio has been obtained from a beam-target asymmetry measurement.

3.3.2 Results from recoil polarization experiments

The results from the two JLab experiments, and other polarization measurements [Mil98, Gay01, Pos01, Die01, Str03, Hu06, MacL06, Jon06], are plotted in Fig. 16 as the ratio $\mu_p G_{Ep}/G_{Mp}$ versus Q^2 . All data show only the statistical uncertainty; the systematic uncertainty for the data of [Gay01, Pun05] are shown separately as a polygon; they are typical for all polarization data obtained in Hall A at JLab. The new asymmetry data from BATES [Cra06] are not in this figure as they are in the range of Q^2 -values smaller than 0.6 GeV²; they appear in Fig. 23. As can be seen from figure 16, data from different experiments are in excellent agreement and the statistical uncertainty is small for all data points; this is unlike G_{Ep} obtained from cross section data and shown in Fig. 5, where we see a large scatter in results from different experiments as well as large statistical uncertainty at higher Q^2 values, underlining the difficulties in obtaining G_{Ep} by the Rosenbluth separation method.

The results from the two JLab experiments [Jon00, Pun05, Gay02] showed conclusively for the first time a clear deviation of the proton FF ratio from unity, starting at $Q^2 \simeq 1$ GeV². The most important feature of the data from JLab, is the sharp decline of the ratio $\mu_p G_{Ep}/G_{Mp}$ from 1 starting at $Q^2 \approx 1$ GeV² to a value of ~ 0.28 at $Q^2 = 5.6$ GeV², which indicates that G_{Ep} falls faster with increasing Q^2 than G_{Mp} . This was the first definite experimental indication that the Q^2 dependence of G_{Ep} and G_{Mp} is different. If the $\mu_p G_{Ep}/G_{Mp}$ -ratio continues the observed linear decrease with the same slope, it will cross zero at $Q^2 \approx 7.5$ GeV² and become negative.

In Fig. 17 all the ratio data obtained from the Rosenbluth separation method are plotted together with the results of the two JLab polarization experiments. There are recent proton FF results obtained with the Rosenbluth separation method from two JLab experiments [Chr04, Qat04]; these results agree with previous Rosenbluth results [Lit70, Ber71, Pri71, Wal94, And94] and confirm the discrepancy between the ratios obtained with the Rosenbluth separation method and the recoil polarization method. The two methods give definitively different results; the difference cannot be bridged by either simple re-normalization of the Rosenbluth data [Arr03], or by variation of the polarization data within the quoted statistical and systematic uncertainties. This

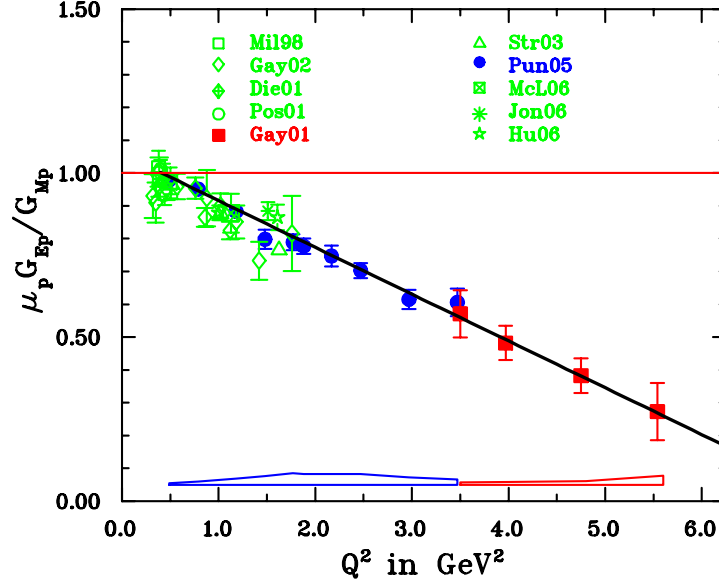


Figure 16: The ratios $\mu_p G_{Ep}/G_{Mp}$ from the two JLab experiments, together with all other polarization transfer experiments. The systematic uncertainties apply to the JLab data only.

discrepancy has been known for past several years and is currently the subject of intense discussion. A possible explanation is the hard two-photon exchange process, which affects both cross section and polarization transfer components at the level of only a few percents; however, in some calculations [Afa01, Blu03] the contribution of the two-photon process has drastic effect on the Rosenbluth separation results, whereas in others it does not [Bys06]; in either case it modifies the ratio obtained with polarization method by a few percent only (this will be discussed in Appendix A). There are several experiments planned at JLab [Sul04, Arr04] to investigate the two-photon effects in the near future.

3.3.3 Measurements of neutron form factors with polarization experiments

Measurements of the FFs of the neutron are far more difficult than for the proton, mainly because there are no free neutron targets. Neutron FF measurements were started at about the same time as for the proton, but the data are generally not of the same quality as for the proton, especially in the case of the electric FF of the neutron; the Q^2 range is limited also. The early measurements of the FFs of the neutron are discussed in sections 2.2.2 and 2.2.3; in this section we discuss only measurements made with longitudinally polarized electron beams on polarized 2H - or 3He -targets, and polarization transfer in the $^2H(\vec{e}, e'\vec{n})p$ reaction. First we discuss the many measurements of the charge FF, G_{En} , and then the relatively few measurements of the magnetic FF, G_{Mn} .

The first measurement of the charge FF of the neutron, G_{En} , by the polarization method was made at MIT-Bates using the exclusive $^2H(\vec{e}, e'\vec{n})p$ reaction [Ede94]. The advantage of polarization measurements on the deuteron in the quasi free kinematics is that the extracted neutron FF is quite insensitive to the choice of deuteron wave functions, and also to higher order effects like final state interaction (FSI), meson exchange currents (MEC) and isobar configurations (IC), when the momentum of the knocked out neutron is in the direction of three-momentum transfer \vec{q} [Are87, Rek89, Lag91].

For a free neutron the polarization transfer coefficient P_x is given by Eq. (27). The relation between polar-

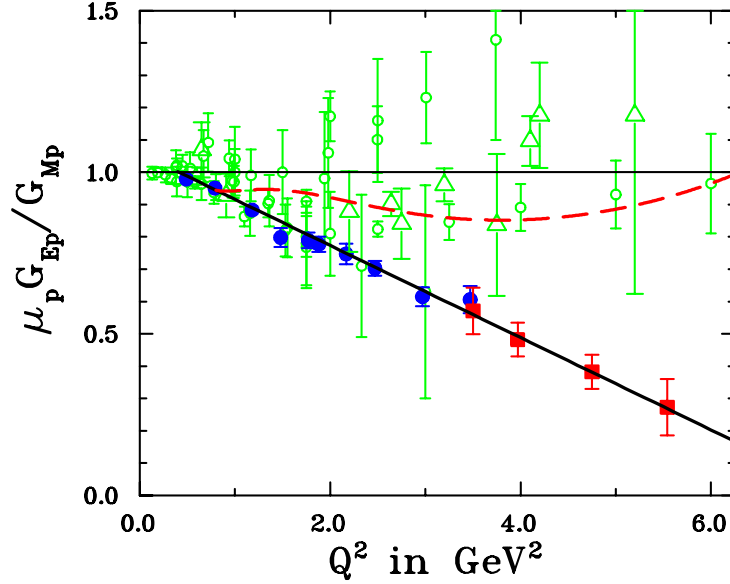


Figure 17: The ratios $\mu_p G_{Ep}/G_{Mp}$ from two JLab polarization experiments compared to the FFs obtained using the Rosenbluth separation method. The recent JLab results using Rosenbluth method from Refs. [Chr04, Qat04] are shown as open, filled triangles, respectively. The rest of the cross section data are as in Figs. 5 and 6 and are shown as open circles. The straight line is a fit to the JLab data only, Eq. (41). The dashed curve is the re-fit of the Rosenbluth data by Arrington [Arr03].

ization transfer coefficient P_x , the beam polarization, P_e , and the measured neutron polarization component, P'_x , is $P'_x = P_e P_x$. The form FF G_{En} was extracted at a Q^2 of 0.255 GeV² in this experiment from the measured transverse polarization component P'_x of the recoiling neutron, and known beam polarization, P_e . This early experiment demonstrated the feasibility of extracting G_{En} from the quasi-elastic $^2H(\vec{e}, e'\vec{n})p$ reaction with the recoil polarization technique, with the possibility of extension to larger Q^2 values.

Next, this same reaction $^2H(\vec{e}, e'\vec{n})p$ was used to determine G_{En} at MAMI [Her99, Ost99] by measuring the neutron recoil polarization ratio P_x/P_z , at a Q^2 of 0.15 and 0.34 GeV². The ratio P_x/P_z is related to G_E/G_M as shown in Eq. (30). The measurement of the ratio, P_x/P_z , has some advantage, as discussed earlier for the proton, over the measurement of P_x only, because in the ratio the electron beam polarization and the polarimeter analyzing power cancel; as a result the systematic uncertainty is small. In yet another experiment at MAMI the ratio of polarization transfer components, P_x/P_z , was measured using the same reaction $^2H(\vec{e}, e'\vec{n})p$ and the electric FF G_{En} was obtained at $Q^2 = 0.3, 0.6$ and 0.8 GeV² [Gla05]; the authors concluded that their results were in good agreement with all other G_{En} double-polarization measurements.

The experiment at JLab by Madey *et al.* [Mad03, Pla05] obtained the neutron FF ratios G_E/G_M at Q^2 values of 0.45, 1.13 and 1.45 GeV² using the same method of measuring the recoil neutron polarization components P_x and P_z simultaneously, using a dipole with vertical B-field to precess the neutron polarization in the reaction plane, hence obtaining directly the ratio G_{En}/G_{Mn} ; The best-fit values of G_{Mn} were used to calculate values of G_{En} from the ratio measurements. This is the first experiment that determined the value of G_{En} with small statistical and systematic uncertainty and at the relatively high Q^2 values up to 1.45 GeV².

Passchier *et al.* [Pas99] reported the first measurement of spin-correlation parameters A_{ed}^V at a Q^2 of 0.21 GeV² in $^2\vec{H}(\vec{e}, e'n)p$ reaction at NIKHEF; this experiment used a stored polarized electron beam and an internal vector polarized deuterium gas target; they extracted the value of G_{En} from the measured sideways

spin-correlation parameter in quasi-free scattering.

Experiment E93-026 at JLab extracted the neutron electric FF at $Q^2 = 0.5$ and 1.0 GeV^2 [Zhu01, War04] from measurements of the beam-target asymmetry using the $^2\vec{H}(\vec{e}, e'n)p$ reaction in quasi elastic kinematics; in this experiment the polarized electrons were scattered off a polarized deuterated ammonia (ND_3) target. This experiment was the first to obtain G_{En} at a relatively large Q^2 using a polarized target.

Blankleider and Woloshyn, in a paper in 1984 [Bla84], proposed that a polarized 3He target could be used to measure G_{En} or G_{Mn} . They argued that the 3He ground state is dominated by the spatially symmetric S-state in which the two proton spins point in opposite directions, hence the spin of the nucleus is largely carried by the neutron. Therefore, the 3He target effectively serves as a polarized neutron target; and in the quasi-elastic scattering region the spin-dependent properties are dominated by the neutron in the 3He target.

There were experiments in the early 1990's at MIT-Bates Laboratory that used a polarized 3He target and measured the asymmetry with polarized electrons in spin-dependent quasi-elastic scattering [Jon91, Tho92], and extracted the value of G_{En} using the prescription of Blankleider and Woloshyn [Bla84], at a $Q^2=0.16$ and 0.2 GeV^2 . However, Thompson *et al.* [Tho92] pointed out that significant corrections are necessary at $Q^2=0.2 \text{ GeV}^2$ for spin-dependent quasi elastic scattering on polarized 3He according to the calculation of Laget [Lag91]; hence no useful information on G_{En} could be extracted from these measurements; but the authors of this paper concluded that at higher Q^2 values the relative contribution of the polarized protons becomes significantly less and a precise measurements of G_{En} using polarized 3He targets will become possible.

Starting in the early 1990's, the neutron electric FF G_{En} has been obtained in several experiments at MAMI, by measuring the beam-target asymmetry in the exclusive quasi-elastic scattering of electrons from polarized helium in $^3\vec{He}(\vec{e}, e'n)pp$ reaction [Mey94, Bec99, Roh99, Ber03]. In the first of these experiments at MAMI, [Mey94], G_{En} was obtained at $Q^2 = 0.31 \text{ GeV}^2$. In the next several experiments at MAMI, G_{En} was extracted at Q^2 of 0.35 GeV^2 [Bec99] and 0.67 GeV^2 [Roh99, Ber03] using the same reaction $^3\vec{He}(\vec{e}, e'n)pp$. In a paper by Bermuth *et al.*, it was concluded that the data had greatly improved the accuracy of G_{En} because the total FSI correction to G_{En} is small at 0.67 GeV^2 . All the G_{En} data from polarization experiments are shown in Fig. 18.

Only two experiments have obtained the magnetic FF of the neutron, G_{Mn} , from polarization observables; both experiments used a polarized $^3\vec{He}$ target. The first experiment at the MIT-Bates laboratory, extracted G_{Mn} from the measured beam-target asymmetry in inclusive quasi-elastic scattering of polarized electrons from polarized $^3\vec{He}$ target at Q^2 of 0.19 GeV^2 [citegao1]; the uncertainty on G_{Mn} was dominated by the statistics, with a relatively small contribution from model dependence of the analysis. The second experiment at JLab obtained G_{Mn} for Q^2 values between 0.1 and 0.6 GeV^2 , by measuring the transverse asymmetry in the $^3\vec{He}(\vec{e}, e')$ reaction in quasi-free kinematics [Xu00, Xu03, And06]. The values of G_{Mn} were extracted in the plane wave impulse approximation (PWIA) at Q^2 of 0.3 to 0.6 GeV^2 , and from a full Fadeev calculation at Q^2 of 0.1 and 0.2 GeV^2 . The authors of this paper asserted that the PWIA extraction of G_{Mn} is reasonably reliable in the Q^2 range of 0.3 to 0.6 GeV^2 ; however, a more precise extraction of G_{Mn} requires fully relativistic three-body calculations. The G_{Mn} values from both experiments are shown in Fig. 19.

In Fig. 20 and 21 we compare all the data available now for G_{En} and G_{Mn} , obtained from cross section and polarization observables. The G_{En} data obtained in double polarization show reasonable consistency above 0.5 GeV^2 ; they are systematically higher than the older cross section results represented in Fig. 20 by the 3 Platchkov fits [Pla90]. The revision by Kelly [Kel04] of the Galster fit [Gal71] gives an excellent representation of the data available today. Much is expected from the recent experiment in Hall A at JLab that measured G_{En}

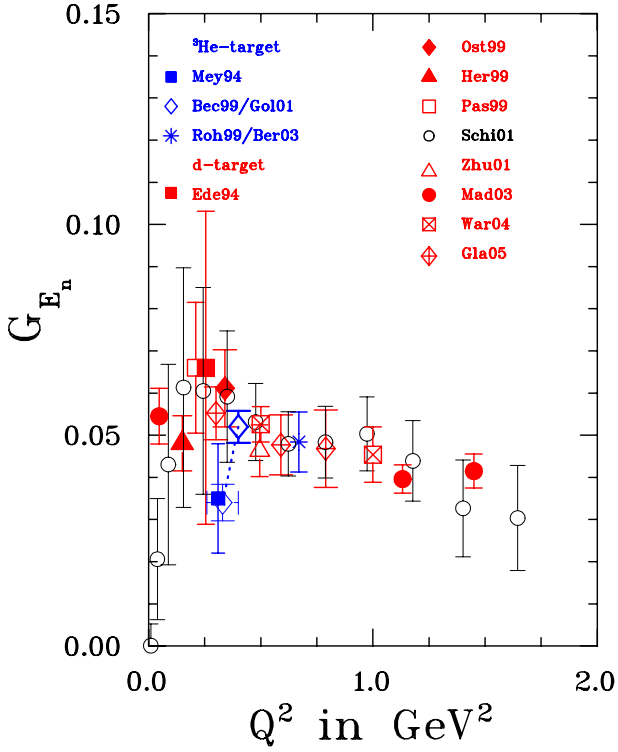


Figure 18: The data base for G_{En} from all polarization experiments, including beam asymmetry with polarized ^3He , and recoil polarization with deuterium target.

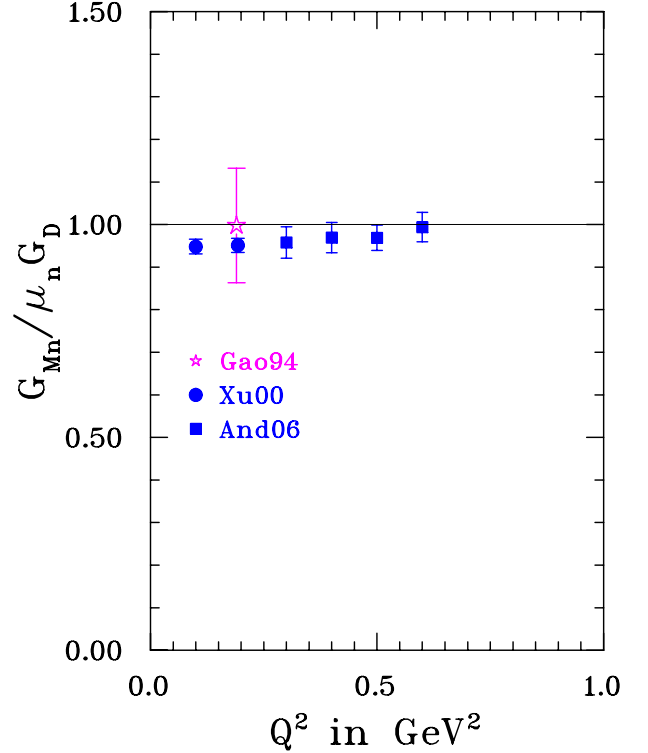


Figure 19: G_{Mn} from the two polarization experiments which have been performed so far, at Bates [Gao94] and JLab [Xu00, Xu03, And06], respectively.

up to Q^2 of 3.4 GeV^2 .

The G_{Mn} data has been augmented by the recent polarization data from Hall A as well as the preliminary new cross section data from simultaneous measurements of $^2\text{H}(e, e'n)$ and $^2\text{H}(e, e'p)$ reactions in Hall B at JLab. In addition to the ^2H target, an in-line ^1H target was used for an in-situ determination of the neutron counter efficiency via π^+ electro-production. As can be seen in Fig. 21 there is some disagreement between the results of different experiments in the Q^2 range of 0.3 to 1.5 GeV^2 .

3.4 Relative merit of recoil polarization versus target asymmetry measurements

We compare in this section the performances of double scattering experiments using focal plane polarimeters and polarized targets, and discuss their figure of merit (FOM), defined as the product of luminosity times either the analyzing power or the target polarization, squared; the discussion is separated into a proton- and a neutron FF measurement part, respectively.

3.4.1 Proton form factors

Both techniques described in sections 3.1 and 3.2, obtain information on G_{Ep} in the presence of a dominant G_{Mp} contribution to the cross section, by measuring the $G_{Ep}G_{Mp}$ interference term present in the transverse

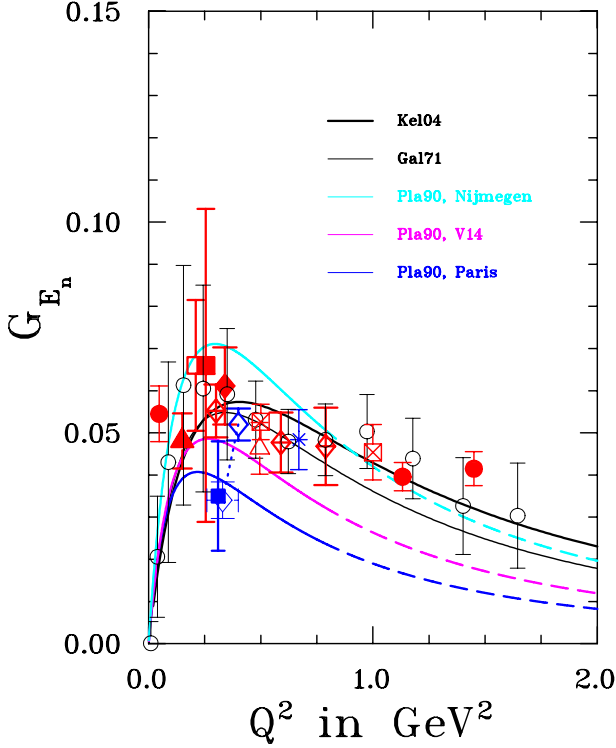


Figure 20: The same G_{En} data as in Fig. 18, compared to various fits. The thick solid line is the fit by Kelly [Kel04], and the thin solid line the fit by Galster [Gal71]. The fits by Platchkov *et al.* to the data shown in Fig. 8, for Reid soft core (dotted-line) [Rei68], Paris (dot-dashed) [Lac81] and Argonne V14 (long dashes) [Wir84] NN potentials, respectively.

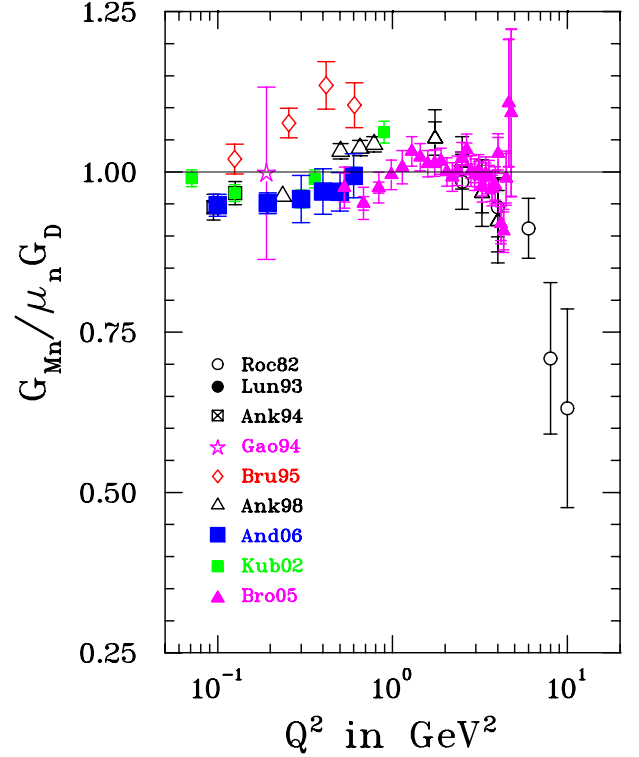


Figure 21: The complete data base for G_{Mn} , from cross section and polarization measurement. Shown as a solid curve is the fit by Kelly [Kel04]; note that in this fit does not include the recent data of Ref. [Bro05b].

component of the recoil proton polarization, or in the asymmetry measured when the target proton polarization is oriented perpendicular to the momentum transfer \vec{q} , in the reaction plane. In both experiments the electron beam helicity is flipped periodically to cancel systematics due to drifts in beam polarization and detector efficiency; in recoil polarization experiments, this beam helicity reversal also cancels possible systematic asymmetries in the polarimeter, as was explained in section 3.3.1.

The two techniques differ in a number of ways which affect their ultimate performance, or “figure of merit” (FOM), particularly at large Q^2 .

For recoil polarization experiments, the maximum possible luminosity, \mathcal{L} , which is the product of the number of target nucleons per cm^2 times the incident electrons flux (sec^{-1}), is limited by the maximum target length compatible with a spectrometer acceptance, typically 20 cm of LH_2 , and the maximum current resulting in acceptable target density fluctuations, $100\mu\text{A}$ with present technology.

With target asymmetry measurements one benefits from a large target polarization, independent of Q^2 , but has a big disadvantage due to limitations on the luminosity imposed by beam current and target thickness. Taking the ammonia target technology perfected by the University of Virginia/University of Basel/SLAC group

[Cra95] as an example, which uses frozen ammonia, $^{15}\text{NH}_3$, as target material in the form of granules immersed in LH_4 , the maximum beam intensity is about 100 nA on a 2.5 cm thick target with a packing fraction $f=0.7$.

Considering only the highest Q^2 , which will come within reach with the upgrade of the JLab accelerator to a beam energy of 12 GeV , in the range $12\text{--}14\text{ GeV}^2$, the decisive factor is the analyzing power of the reaction used to measure the recoil proton polarization. Extrapolating data obtained in Dubna [Azh04] and shown in Fig. 22 up to a proton momentum of $5.3\text{ GeV}/c$, to the required momentum of $7.3\text{--}8.3$ corresponding to these Q^2 -values, one can anticipate $A_y \sim 0.05$; the new polarimeter in Hall C will have an efficiency larger than 0.5 , the largest ever obtained in this momentum range.

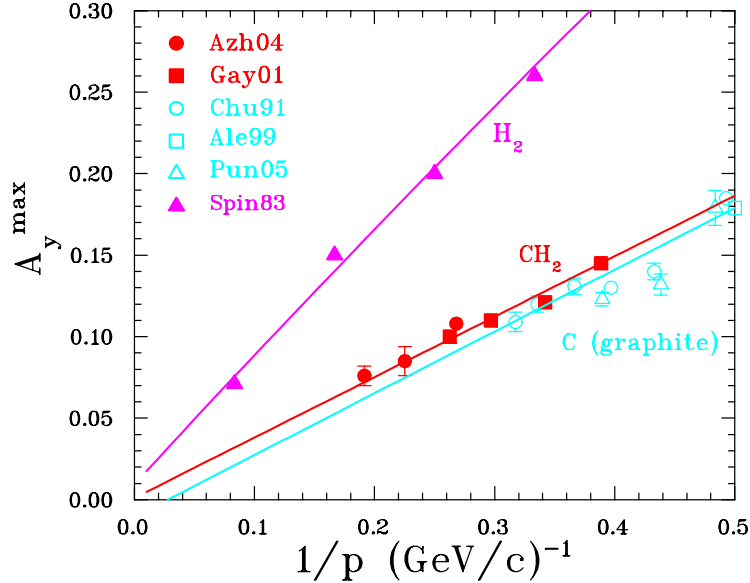


Figure 22: Data base for the maximum analyzing power, A_y^{max} , for polarized proton in graphite, CH_2 and hydrogen. The $1/p$ representation nearly linearizes A_y^{max} . An extrapolation of the CH_2 -data indicates analyzing powers larger than 0.05 exist up to at least $8\text{ GeV}/c$ proton momentum, corresponding to $Q^2 \sim 13\text{ GeV}^2$.

For ammonia ($^{15}\text{NH}_3$) targets, a polarization of $A_{target}=0.8$ is currently standard, but the technique requires periodical target annealing and target material changes, resulting in a usable time fraction of $\sim 90\%$. The number of protons in the target is reduced by the packing fraction. The measured target asymmetry is smaller than the physics asymmetry by the target polarization dilution factor, f' , because of the presence of unpolarized components in the target (^4He , N ,...); for ammonia, $^{15}\text{NH}_3$; the dilution factor is close to 1 in coincidence experiments.

The figure of merit is defined as $FOM = \mathcal{L}A^2$, where A is either the average polarimeter analyzing power for recoil polarization, A_y , or the polarization of the proton in the target, A_{tgt} , and \mathcal{L} is the luminosity. Typical luminosities and FOMs for proton FF experiments are given in Table 2, with information about target thickness, analyzing power or target polarization, and overall efficiency. This discussion has been limited to target- and polarimeter performance; other factors, like detector acceptance and efficiency, will contribute significantly and differently to the overall performance of a particular experiment.

reaction	target length (cm)	\mathcal{L}	polarization or analyzing power	“efficiency”	FOM
$^1H(\vec{e}, e'p)$	20	5.3×10^{38}	0.05	0.5	6.6×10^{35}
$N\vec{H}_3(\vec{e}, e'p)$	2.5	1.2×10^{35}	0.8	0.6	4.6×10^{34}
$^2H(\vec{e}, e'n)$	15	3.3×10^{38}	0.2	1.2×10^{-3}	1.6×10^{34}
$N\vec{D}_3(\vec{e}, e'n)$	2.5	1.1×10^{35}	0.25	0.6	3.8×10^{33}
$^3\vec{He}(\vec{e}, e'n)$	40	5.0×10^{35}	0.5	0.9	1.1×10^{35}

Table 2: Relative merit of recoil polarization, and beam-target asymmetry measurement for proton and neutron FF measurements. The numbers for the first entry are for $Q^2=13 \text{ GeV}^2$.

3.4.2 Neutron form factors

Double scattering experiments have recently been performed at JLab to measure the electric FF of the neutron, G_{En} ; three different target types have been used: the first experiment measured the target asymmetry from a polarized deuterated ammonia target in $N\vec{D}_3(\vec{e}, e'n)$ [War04], the second measured the recoil polarization of the neutron, with an unpolarized LD_2 target in $^2H(\vec{e}, e'n)$ [Pla05], and the third and most recent was a determination of the target asymmetry with a polarized 3He -target in $^3\vec{He}(\vec{e}, e'n)$ [Cat03]. Next we compare the figure of merits (FOM) of these three experiments.

The ammonia target used in the measurement of G_{En} up to 1 GeV^2 [War04] is the same one discussed in previous section, NH_3 replaced by ND_3 ; its FOM is reduced relative to that for NH_3 because of the smaller polarization of the deuterium compared to hydrogen.

In the recoil polarization measurement of G_{En} up to 1.5 GeV^2 [Mad03, Pla05] a standard 15 cm liquid deuterium target was used, and the polarization of the recoil proton measured in a polarimeter preceded by a dipole with vertical magnetic field, to precess the two in-plane components of the polarization in the horizontal plane. The polarimeter consisted of an analyzer block made of scintillator plastic, 42.6 cm thick, preceded by an iron shield, and two sets of scintillator detectors to detect up-down asymmetry. The overall polarimeter efficiency was 1.2×10^{-3} , the average analyzing power for neutrons was ~ 0.2 .

In the most recent measurement of G_{En} with a 40 cm long polarized 3He -target [Cat03] operated at 10 times the STP density, the luminosity was limited by detector rates; with smaller detector solid angles the luminosity can be twice the number in Table 2; the target polarization was $A_{target} \sim 0.5$.

The luminosities and FOMs for these 3 experiments are given in Table 2. The evident advantage of the $^3\vec{He}$ target over $N\vec{D}_3$ for target asymmetry measurement on the neutron, and over the recoil polarization experiment, is due to recent progress in polarized 3He target performance, and translates into promising future measurements of the neutron FF. This situation is to be contrasted with the one for proton FF measurements, for which currently the recoil polarization technique has a definite advantage over polarized target technique, up to a Q^2 of $\sim 13 \text{ GeV}^2$. Note that proton polarimeters have typical efficiencies of 0.3 to 0.5, contrasting with the 1.2×10^{-3} of the polarimeter in [Pla05]. The overall efficiency of the neutron recoil polarimeter can probably be improved in a future design. As Fig. 22 demonstrates, the proton analyzing power is expected to remain large enough up to momenta of $8 \text{ GeV}/c$, corresponding to a $Q^2 \sim 13 \text{ GeV}^2$. In neutron FF experiments the advantage of deuterium over helium as a target material, due to the smaller nuclear structure corrections,

is getting less significant at the increasing Q^2 's of future experiments.

3.5 Discussion of the form factor data

Probably the most important advance in the characterization of the FFs of the nucleon made in the last 10 years has been the realization that the so-called “scaling”-behavior of the proton FFs:

$$G_{Ep} \sim G_{Mp}/\mu_p \sim G_D, \quad (40)$$

was limited to values of Q^2 smaller than 2 GeV². The recoil polarization data obtained at JLab in 1998 and 2000 proved beyond any doubt that for Q^2 -values larger than 2 GeV², G_{Ep} decreases faster than G_{Mp}/μ_p with a slope of -0.14 per GeV². What we now have are distinctly different Q^2 -dependences for G_{Ep} and G_{Mp} ; in the Q^2 region investigated so far, the scaling-behavior is violated by a factor of $3.66^{+1.71}_{-0.88}$ at 5.54 GeV². The deviation of G_{Ep} from the dipole FF is illustrated in Fig. 23, where only polarization results are shown. Of course it was well known that the dipole FFs, when Fourier transformed, produce unphysical distributions of charge or magnetization, with a discontinuity at zero radius. Nevertheless there were valid reasons, based on the dispersion relation approach, to believe that the dipole FF may actually describe the FFs G_{Ep} , G_{Mp} and G_{Mn} of the nucleon. The data no longer support such expectations, as can be concluded by comparing the results in Figs. 5 and 23.

The discrepancy is related to the techniques used: all Rosenbluth separation of cross section data including the 2 new measurements from JLab [Chr04, Qat04] give $\mu_p G_{Ep}/G_{Mp}$ ratios close to the scaling behavior, except the early data shown in Fig. 3; all recoil polarization results for the same ratio are clustered along an approximately straight line versus Q^2 , with a best fit valid above $Q^2 \sim 0.4$ GeV² given by:

$$\mu_p G_{Ep}/G_{Mp} = 1.0587 - 0.14265Q^2. \quad (41)$$

A number of observations relative to this difference in results follows. First, there is one well established difference between the two techniques, cross section versus recoil polarization, and it is the relative importance of the radiative corrections required for them, as discussed in detail in section 3.6. The total radiative corrections as routinely calculated in cross section measurements is typically 10 to 30%, and the corrections are strongly ϵ dependent; this ϵ dependence affects primarily the results for G_{Ep}^2 , and for increasing Q^2 the accuracy requirement for the correction becomes very demanding. Second, polarization observables, in recoil polarization or target asymmetry measurements, being ratios of cross sections, are only minimally affected by radiative corrections, and the ratio G_E/G_M even less being a ratio of ratios. Nevertheless polarization data ultimately will require radiative corrections, particularly as experiments continue into the domain of yet larger Q^2 . So is the discrepancy between Rosenbluth and polarization data entirely due to inaccuracy or incompleteness in the radiative correction? An immediate consequence of the previous statements is that radiative corrections for elastic ep scattering in general have to be reexamined, as in their presently practiced form they are unable to reconcile the cross section results with polarization results.

Encouraging progress has been made including the one process certainly neglected in all previous radiative corrections, the exchange of two photons, neither one of them “soft” (this will be further discussed in section 3.6). Several calculations [Gui03, Afa05, Blu03] suggest that this one diagram may contribute significantly to the ϵ -dependence of the cross section; other considerations lead to the conclusion that the contribution from the two-photon term is too small at the Q^2 -values of interest [Bys06], and/or leads to a definite non-linearity in the Rosenbluth plot which has not been seen in the data so far [Tom05a].

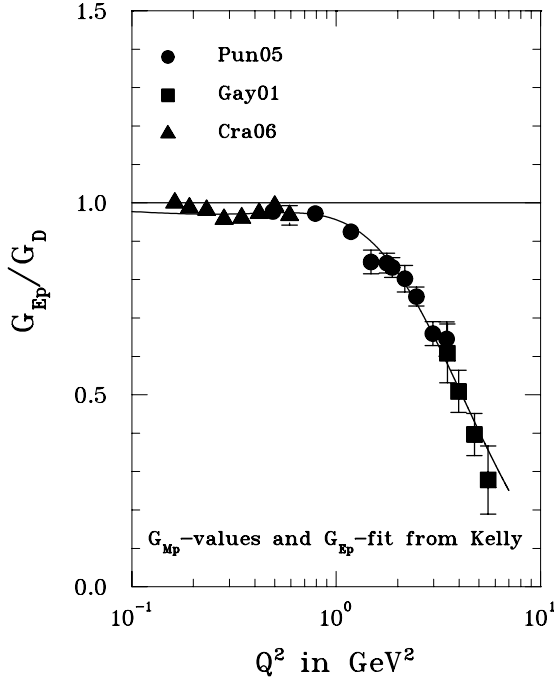


Figure 23: Polarization data presented as G_{Ep}/G_D , where G_{Ep} is obtained from the ratio G_{Ep}/G_{Mp} obtained from polarization data in [Pun05, Gay01, Cra06], multiplied by G_{Mp} from the Kelly fit [Kel04].

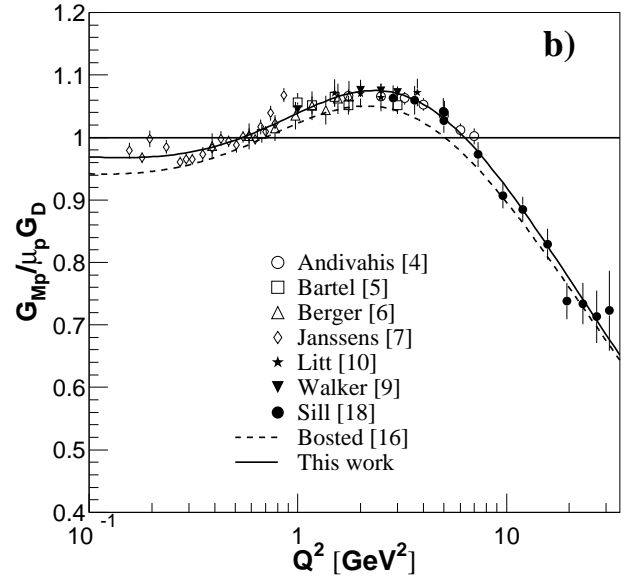


Figure 24: The G_{Mp} data were refitted in Ref. [Bra02] imposing the value of the G_{Ep}/G_{Mp} from the recoil polarization data of Refs. [Pun05, Gay01], leaving out Rosenbluth separation data above 1 GeV^2 .

Further, it has been argued by Tomasi-Gustafsson that the Rosenbluth separation method may not work for larger Q^2 values, as the correlation between the 2 parameters of the linear fit to the reduced cross section data from Eq. (19) increases, when the error bars increase, or G_{Ep}^2 becomes small relative to G_{Mp}^2 ; as shown in the statistical analysis in Ref. [Tom06] for the Rosenbluth separation data of Walker *et al.* [Wal94], the correlation between the two parameters of the linear fit, slope and intercept, becomes close to -1, indicating that only one parameter can be obtained from the data.

Following the acquisition of the JLab recoil polarization G_{Ep}/G_{Mp} ratios up to 5.54 GeV^2 , the entire data base for the two proton FFs has been reanalyzed by Brash *et al.* [Bra02], leaving all Rosenbluth separated data above $Q^2 = 1 \text{ GeV}^2$ out, but using the data from [Jon00, Gay01] above this value of Q^2 , and allowing for relative renormalization of all cross section data so as to minimize the χ^2 of a global fit for G_{Mp} . The fitting function is the inverse of a polynomial of order 5. The renormalized values of G_{Mp} show significantly less scatter than the original data base, and the net effect of imposing the recoil polarization results is to renormalize all G_{Mp} data upward by 1.5-3% when compared with the older Bosted parametrization [Bos95], as shown in Fig. 24.

Another useful fit to all 4 FFs which gives a good representation of the data is the one by Kelly [Kel04]. This fit uses ratios of polynomials with maximum powers chosen such that G_{Ep} , G_{Mp} and G_{Mn} have the asymptotic $1/Q^4$ behavior required by pQCD; in [Kel04] G_{En} was also re-fitted with a Galster FF, as shown in Fig. 20.

Recently, more and better data have been obtained for G_{En} , exclusively by the polarization method, either recoil polarization transfer or target asymmetry, with deuterium and ^3He targets and up to $Q^2=1.5\text{ GeV}^2$. No drastic change of the general behavior of G_{En} has been observed to this point in time. There is a new measurement of G_{En} at JLab up to a Q^2 of 3.4 GeV^2 , but the data have yet to be analyzed. In general all polarization data for G_{En} have given results larger than those obtained from elastic scattering; these earlier data required considerable nuclear structure corrections, as illustrated in Fig. 18; the sensitivity to the deuteron wave function, therefore to the NN potential used, was extensively discussed at the time in Ref. [Pla90].

The data for G_{Mn} come mostly from cross section measurements, except two polarization measurements, using polarized ^3He target, one at MIT-Bates lab for low Q^2 with large uncertainty [Gao94] and the other recent measurement at JLab [Xu00, Xu03, And06]. The most recent Hall B results [Bro05b], which extend to Q^2 of nearly 5 GeV^2 , and used quasi-elastic scattering on deuterium, reveal some internal inconsistency in the data base near 1 GeV^2 as shown in Fig. 21. These measurements will be extended to 14 GeV^2 after the JLab upgrade to 12 GeV ; similarly, the measurement of G_{Ep}/G_{Mp} will be continued to 13 GeV^2 after the upgrade.

Several experiments are planned at JLab to resolve the dichotomy in the G_{Ep}/G_{Mp} ratio. One experiment will measure the ratio of the e^-p and e^+p cross sections, which determines directly the real part of the two-photon amplitude ([Afa04]). Another experiment will measure the ratio G_{Ep}/G_{Mp} at fixed $Q^2=2.5\text{ GeV}^2$ [Sul04], as a function of ϵ , with the goal of detecting direct evidence for the two hard photon contribution as a variation of this ratio; the ratio must be constant in Born approximation as both G_{Ep} and G_{Mp} are functions of Q^2 only; non constancy would be related to the real part of the two-photon amplitude. A third experiment will be a high statistics search of non-linearity in the Rosenbluth plot in ep -scattering, which should also reveal the contribution of the two-photon process ([Arr05]). Measurements of the induced polarization in $ep \rightarrow e\vec{p}$ (a byproduct of the experiment from Ref. [Sul04]), and of the single spin asymmetry in quasi elastic scattering on the neutron in $^3\text{He}^\uparrow(e, e')$ for target polarization normal to the reaction plane [Ave05], will measure the imaginary part of the two-gamma contribution. It is possible, in principle with an appropriate model, to connect the imaginary part to the real part of the amplitude which contribute to the cross sections.

3.6 Rosenbluth results and radiative corrections

All cross section measurements have been single arm experiments, (e, e') , except three early experiments at Cambridge [Pri71, Han73] and DESY [Bar73] in which both proton and electron were detected, $(e, e'p)$ and the most recent one of Qattan *et al.* [Qat04], in which only the proton was detected, (e, p) . These measured raw cross sections need to be corrected for QED processes to first order in $\alpha_{em} = e^2/4\pi$ before accessing the cross section corresponding to one-photon exchange, or Born term. Only to the extent that these corrections remain relatively small, can one hope to obtain the Born term FFs G_E^2 and G_M^2 , which are functions of Q^2 only, using the Rosenbluth method.

The effect of the radiative correction on the cross section is typically in the range 10-30%; what is important however, is the fact that overall, the radiative corrections are ϵ -dependent; i.e. they affect the slope of the Rosenbluth plot. Although radiative corrections have been applied to all data taken after 1966 using the “recipe” of Tsai [Tsa61], Mo and Tsai [MoT69] and [Tsa71], not all corrections were applied in all data sets. This point was recently reviewed by Arrington [Arr03], who reanalyzed some of the cross section data; the fit to the re-analyzed data is included in Fig. 17. Furthermore, in the references [Tsa61, MoT69, Tsa71] the effect of the structure of the nucleon was ignored, and a number of approximations were made. In more recent work on radiative corrections, Maximon and Tjon [Max00] have included the structure of the proton by introducing the proton FF, and they also eliminated some of the soft-photon approximations made by [Tsa61, Tsa71, MoT69].

In the current energy range of JLab, the difference for δ , the radiative correction, used in $\frac{d\sigma}{d\Omega} = (1 + \delta) \frac{d\sigma^{Born}}{d\Omega}$ up to corrections of order α^3 , between the older and the new calculation is at the level of several %.

The various internal radiative correction diagrams involving the electron are shown in Fig. 25. The first order virtual radiative processes are the vertex diagram and the self-energy for the electron, as well as the photon self-energy diagram; the first order real radiative processes include emission of a real photon by either the initial or the final electron. Similarly diagrams for the proton are shown in Fig. 26. In addition there are external radiative corrections due to the emission of real photons by the incoming and scattered electrons in the material of the target, as well as due to the energy loss by ionization.

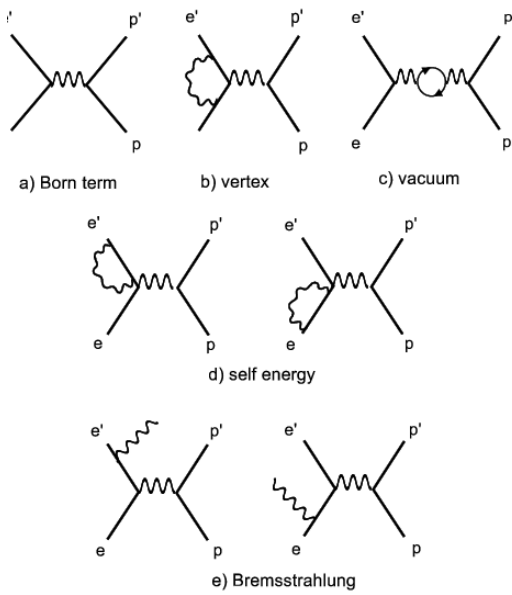


Figure 25: Born term and lowest order radiative correction graphs for the electron in elastic ep .

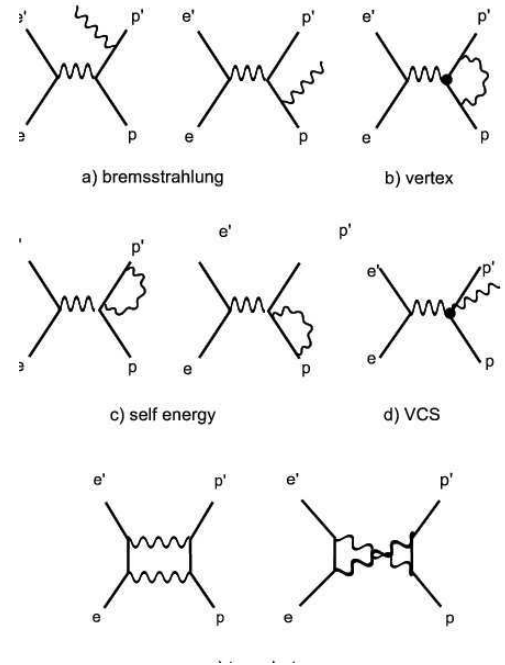


Figure 26: Lowest order radiative correction for the proton side in elastic ep scattering.

The virtual part of the internal radiative corrections depend exclusively upon Q^2 , thus does affect all kinematics for a given Q^2 identically; it generates no ϵ -dependence and hence does not modify the value of G_{Ep}^2 , but modifies the value of G_{Mp}^2 directly.

The radiative correction for real photon emission (bremsstrahlung) is energy, and therefore ϵ dependent, and it also results in a changed value of Q^2 . In general the scattered electron energy spectrum is integrated up to a maximum energy loss which is kept below the pion threshold. The correction might be different for different experiments, depending on the “recipe” used to integrate over the scattered electron energy, or missing mass squared spectrum.

The contributions due to real photon emission by the initial and final proton, as well as the proton vertex and two-photon exchange with one soft- and one hard photon are relatively small, but strongly ϵ -dependent.

The external part of radiative corrections includes only real photon emission by the incident and scattered electron, and is not coherent with the ep interaction. Although the correction for the incoming electron in the target is energy independent, and it can be averaged to a value at the center of the active area of the target for all kinematics of a given experiment, the correction for the scattered electron in the target depends directly upon

the scattering angle, therefore the target length and diameter which determines the amount of target material traversed. As the desired range of ϵ values is obtained by changing the electron scattering angle, this correction has ϵ -dependence. For the data of Andivahis *et al.* [And94] the external corrections are one fourth to one half as large as the internal corrections from the smallest to the largest ϵ -values as shown in Fig. 27. The calculation of the external correction requires information on the spectrometer acceptance and on the target geometry, and is an integral part of the analysis of the data; it cannot be repeated on the basis of published data. However, it is potentially a significant source of uncertainty in the ϵ -dependence of the total radiative correction.

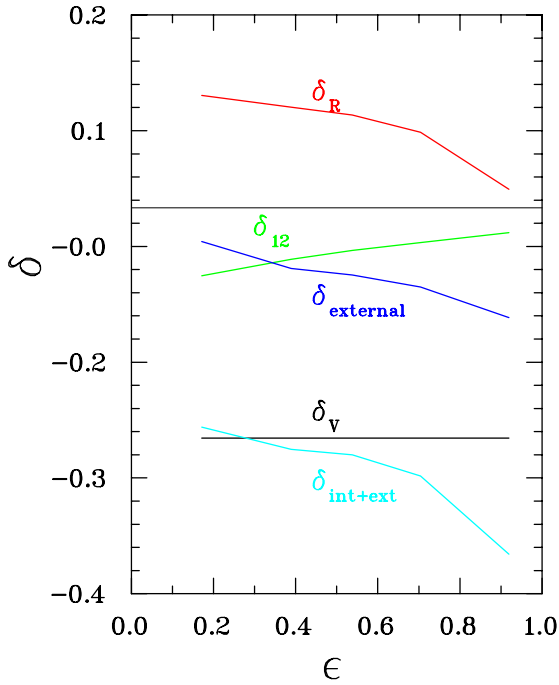


Figure 27: The various contributions to the correction factor δ at $Q^2=5 \text{ GeV}^2$, calculated with the code from [Vdh00] based on the work of Maximon and Tjon [Max00], including the external correction for a 15 cm target, taken from Ref. [And94],

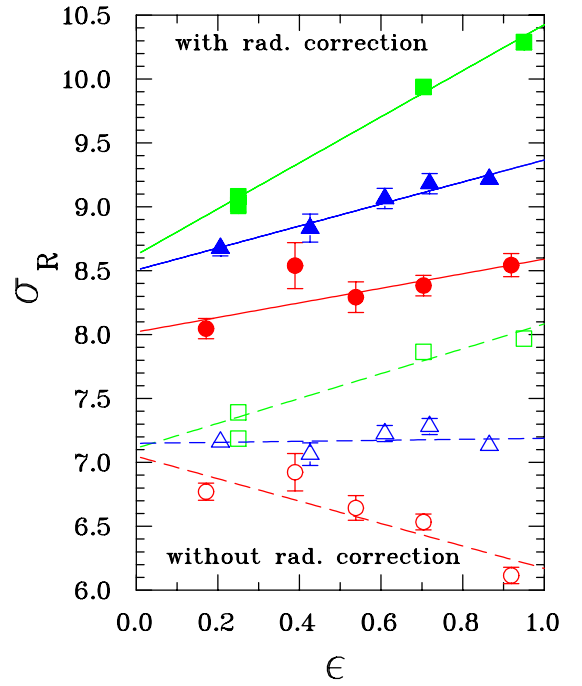


Figure 28: The Rosenbluth plot for the data of Andivahis *et al.* [And94] showing at the bottom the data before correction for radiative effects, at the top after radiative correction. The filled squares, triangles and circles correspond to 1.75, 3.25 and 5 GeV^2 , respectively; the corresponding empty symbols show the uncorrected data.

To gain some appreciation of what term might be most strongly affecting the final result of the radiative correction, we show the values δ_{real} , $\delta_{virtual}$, δ_{12} and $\delta_{external}$ separately in Fig 27, where δ_R and δ_V refer to the real and virtual corrections on the electron side (Fig.25), and δ_{12} refers to the real plus virtual radiative correction on the proton side (Fig.26). The curve in Fig. 27 labeled $\delta_{int+ext}$ determines the overall correction. Its slope versus ϵ is due to the combined effect of the real and external-contributions, with the proton contribution reducing it somewhat.

The importance of calculating the contributions to the radiative correction which are ϵ -dependent accurately is illustrated in Fig. 28. Shown in this figure are reduced cross sections defined in terms of the $(\frac{d\sigma}{d\Omega})_{reduced}$ from

Eq. (19) as:

$$\sigma_R = \left(\frac{d\sigma}{d\Omega} \right)_{\text{reduced}} / G_D^2 = \frac{\epsilon}{\tau} \frac{G_{Ep}^2}{G_D^2} + \frac{G_{Mp}^2}{G_D^2}, \quad (42)$$

as a function of ϵ for the data of Andivahis *et al.* [And94]. If both FFs are functions of Q^2 only, the intercept of a straight line fit is $G_{Mp}^2/G_D^2 \sim \mu_p^2$, the slope is $\frac{1}{\tau} \frac{G_{Ep}^2}{G_D^2}$. Most noticeable in this figure is the negative slope of the uncorrected data, above $Q^2=3 \text{ GeV}^2$. This figure dramatically illustrates the importance of the radiative correction and gives a measure of the accuracy that is required to obtain the FFs with the desired accuracy. The final value of G_{Ep}^2 obtained from cross section data depends directly upon the value and the accuracy of the ϵ -dependent part of the radiative correction. Note that the radiative corrections for data of Ref. [And94] were made following Mo and Tsai [Tsa61, MoT69, Tsa71], in which only the infrared divergent part from the contribution of the proton vertex and two-gamma exchange were included.

More recently Maximon and Tjon [Max00] have reconsidered the radiative correction calculation, and included additional terms with explicit emphasis of the hadronic effects. A similar reexamination of the Mo-Tsai procedure was made by Vanderhaeghen *et al.* [Vdh00] in the process of a detailed calculation of radiative corrections for virtual Compton (VCS). Also recently Ent *et al.* [Ent01] and Weissbach *et al.* [Wei04] have published improvements and detailed studies of the radiative correction calculation technique for coincidence experiments (e,e'p).

Most recently Bystritskiy *et al.* [Bys06] have calculated the radiative corrections for elastic *ep* scattering using the Drell-Yan electron structure function approach; no co-linearity approximation is made in such a calculation, but the proton vertex corrections have not been included so far; the diagram with two hard photons is included but has been found to make a negligible contribution. The results in [Bys06] differ from the standard radiative corrections [Tsa61, MoT69, Tsa71] applied in Ref. [And94] by -4 % at $Q^2=5 \text{ GeV}^2$ and $\epsilon=1$, as shown in Fig. 29 (dashed line); in the same figure, the dotted line represents the results from Afanasev *et al.* [Afa05] who calculates the two-photon diagram with the help of Generalized Parton Distributions (GPD) fitted to the proton-neutron FF data base; also shown in Fig. 29 is the result of applying the radiative correction based on Ref. [Vdh00] as the dash-dotted line, and the results of the recoil polarization experiments from Eq. (41) (thin solid line).

All three corrections are different, and each one of them brings the Rosenbluth results closer to the recoil polarization results, indicating that present uncertainties in the calculations of the radiative corrections of the cross section are at the level of 0.5%.

In addition to the above considerations, Afanasev [Afa05b] has shown that including a previously neglected spin-dependent term to the hard part of the bremsstrahlung contribution, resulted in an additional ϵ -dependent correction at the 1% level.

Following the important discrepancy between the determinations of G_{Ep}/G_{Mp} using the polarization transfer and Rosenbluth techniques, the role of two hard photon exchange effects, beyond those which have already been accounted for in the standard treatment of radiative corrections has been studied. A general study of two- (and multi)-photon exchange contributions to the elastic electron-proton scattering observables was given in Ref. [Gui03]. In that work, it was noted that the interference of the two-photon exchange amplitude with the one-photon exchange amplitude could be comparable in size to the $(G_{Ep})^2$ term in the unpolarized cross section at large Q^2 . In contrast, it was found that the two-photon exchange effects do not impact the polarization-transfer extraction of G_{Ep}/G_{pM} in an equally significant way. Thus a missing and un-factorisable part of the two-photon exchange amplitude at the level of a few percent may well explain the discrepancy between the two methods.

Realistic calculations of elastic electron-nucleon scattering beyond the Born approximation are required in order to demonstrate in a quantitative way that 2γ exchange effects are indeed able to resolve this discrepancy.

Recently, several model calculations of the 2γ exchange amplitude have been performed. In Ref. [Blu03], a calculation of the 2γ exchange when the hadronic intermediate state is a nucleon was performed. It found that the 2γ exchange correction with intermediate nucleon can partially resolve the discrepancy between the two experimental techniques. Subsequently, it was found in Ref. [Kon05] however that the effect is partly canceled when including the next hadronic intermediate state, the $\Delta(1232)$ resonance. The 2γ exchange contribution to elastic eN scattering has also been estimated at large momentum transfer [Che04, Afa05], through the scattering off a parton in a proton by relating the process on the nucleon to the generalized parton distributions. This approach effectively sums all possible excitations of inelastic nucleon intermediate states. Applying the two-photon exchange corrections to the unpolarized data (see dotted curve in Fig. 29), yields a much flatter slope for the Rosenbluth plot, hence a much smaller value of G_E . The two-photon exchange corrections to the Rosenbluth process can therefore substantially reconcile the two ways of measuring G_E/G_M (compare dotted with thin solid curves in Fig. 29).

To push the precision frontier further in electron scattering, one needs a good understanding, of 2γ exchange mechanisms, and of how they may or may not affect different observables. This justifies a systematic study of such 2γ exchange effects, both theoretically and experimentally. Experimentally, the real part of the 2γ exchange amplitude can be accessed through the difference between elastic electron and positron scattering off a nucleon. Such experiments are planned in the near future.

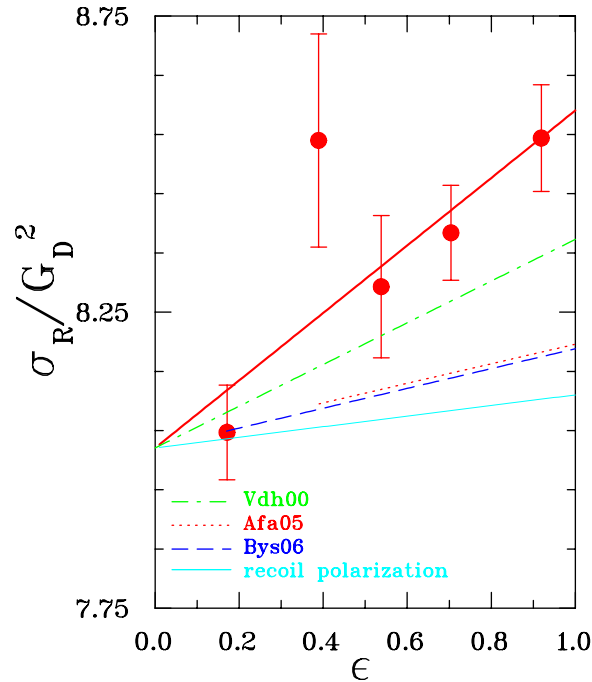


Figure 29: The $Q^2 = 5 \text{ GeV}^2$ data of [And94], with their best fit (thick solid line), compared with the results of the various calculations of the radiative corrections described in the text.

To conclude, on the one hand the discussion above makes it clear that the radiative corrections, including two hard photon exchange, for the cross section data are not complete at this point in time. Therefore, the FFs

G_E^2 and G_M^2 obtained using the Rosenbluth method above Q^2 of 2 GeV^2 are not correct. On the other hand, all the authors cited above agree that radiative corrections change the longitudinal and transverse polarization components, P_t and P_ℓ , in $\vec{e} + p \rightarrow e + \vec{p}$, similarly, with the ratio P_t/P_ℓ affected only at the level of a few percent. The radiative corrections specifically calculated for the JLab polarization data by Afanasev *et al.* [Afa01] found that the corrections are $\sim 1\%$, whereas the hard two photon exchange effects are at the few percent level [Che04, Afa05]. Hence the polarization transfer method gives correct values for the FFs.

4 Theoretical interpretation of nucleon electromagnetic form factors

In this section we give an overview of the theoretical understanding of the nucleon e.m. FFs. These FFs encode the information on the structure of a strongly interacting many-body system of quarks and gluons, such as the nucleon. This field has a long history and many theoretical attempts have been made to understand the nucleon FFs. This reflects the fact that a direct calculation of nucleon FFs from the underlying theory, Quantum Chromodynamics (QCD), is complicated as it requires, in the few GeV momentum transfer region, non-perturbative methods. Hence, in practice it involves approximations which often have a limited range of applicability. Despite their approximations and limitations, some of these non-perturbative methods do reveal some insight in the nucleon structure.

The earliest models to explain the global features of the nucleon FFs, such as its approximate dipole behavior, were vector meson dominance (VMD) models which are discussed in Sect. 4.1. In this picture the photon couples to the nucleon through the exchange of vector mesons. Such VMD models are a special case of more general dispersion relation fits, which allow to relate time-like and space-like FFs, and which are discussed subsequently.

To understand the structure of the nucleon in terms of quark and gluon degrees of freedom, constituent quark models have a long history. We discuss the intricacies in describing a bound system of relativistic constituent quarks and review the resulting predictions for FFs in Sect. 4.2. Despite some of their successes, models based on quarks alone do suffer from the evident shortcoming that they do not satisfy the global chiral symmetry of QCD when rotating left and right handed light quarks in flavor space. This chiral symmetry is broken spontaneously in nature, and the resulting Goldstone bosons are pions. Since they are the lightest hadrons, they dominate the low momentum transfer behavior of form factors, and manifest themselves in a pion cloud surrounding the nucleon. Such pion cloud models will also be discussed in Sect. 4.2.

In Sect. 4.3, we discuss the spatial information which can be obtained from the nucleon FFs, and discuss both radial densities and the issue of shape of the nucleon.

Sect. 4.4 describes the chiral effective field theory of QCD and their predictions for nucleon FFs at low momentum transfers, where such perturbative expansions are applicable.

In Sect. 4.5, we shall discuss the lattice QCD simulations, which have the potential to calculate nucleon FFs from first principles. This is a rapidly developing field and important progress has been made in the recent past. Nevertheless, the lattice calculations are at present still severely limited by available computing power and in practice are performed for quark masses sizably larger than their values in nature. We will discuss the issues in such calculations and compare recent results. It will also be discussed how the chiral effective field theory can be useful in extrapolating present lattice QCD calculations to the physical pion mass.

In Sect. 4.6, we discuss the quark structure of the nucleon and discuss generalized parton distributions (GPDs) of the nucleon. These GPDs are being accessed in hard exclusive reactions, which allow to remove in a controlled way a quark from the initial nucleon and implanting instead another quark in the final nucleon. The resulting GPDs can be interpreted as quark correlation functions and have the property that their first moments exactly coincide with the nucleon FFs. We discuss the information which has been obtained on GPDs from fits of their first moments to the precise FF data set.

Finally, in Sect. 4.7, we discuss the nucleon FFs in the framework of perturbative QCD. These considerations are only valid at very small distances, where quarks nearly do not interact. In this limit, the nucleon FFs correspond with a hard photon which hits a valence quark in the nucleon, which then shares the momentum with the other (near collinear) valence quarks through gluon exchange. We discuss the predictions made in this limit and confront them with the experimental status for Dirac and Pauli FFs at large momentum transfers.

4.1 Dispersion theory

4.1.1 Vector Meson Dominance (VMD)

The starting point in understanding the interaction of a vector probe such as the photon with a hadronic system is provided by the observation that the lowest lying hadrons with vector quantum numbers are the vector mesons $\rho(770)$, $\omega(782)$ and $\phi(1020)$. In the process $e^+e^- \rightarrow \text{hadrons}$, these vector mesons show up as prominent resonances at the corresponding values of the e^+e^- squared *c.m.* energy $q^2 > 0$. One therefore expects that in the elastic electron scattering process on the nucleon, $eN \rightarrow eN$, the nucleon electromagnetic FFs at low space-like momentum transfers, $q^2 < 0$, will be dominated by these lowest lying singularities from the time-like region. A large class of models for F_1 and F_2 are based on this vector meson dominance (VMD) hypothesis, as depicted in Fig. 30.

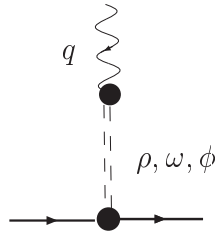


Figure 30: The vector meson dominance picture for the coupling of the photon (with four-momentum q) to a nucleon.

Within such VMD models, the approximate dipole behavior of the nucleon e.m. FFs, see Eq. (23), can be understood as being due to the contribution of two nearby vector meson poles which have opposite residues. Assume that one considers two vector meson pole contributions in Fig. 30 (with masses m_{V_1} and m_{V_2} and residues of equal magnitude and opposite sign a and $-a$ respectively), one obtains :

$$\begin{aligned} F_{1,2}(q^2) &\sim \frac{a}{q^2 - m_{V_1}^2} + \frac{(-a)}{q^2 - m_{V_2}^2}, \\ &= \frac{a(m_{V_1}^2 - m_{V_2}^2)}{(q^2 - m_{V_1}^2)(q^2 - m_{V_2}^2)}. \end{aligned} \quad (43)$$

An early VMD fit was performed by Iachello *et al.* [Iac73] which predicted a linear decrease of the proton G_{Ep}/G_{Mp} ratio, which is in basic agreement with the result from the polarization transfer experiments. Such VMD models have been extended by Gari and Krümpelmann [Gar85] to include the perturbative QCD (pQCD) scaling relations [Lep80] for the nucleon electromagnetic FFs, which state that, see Sect. 4.7, $F_1 \sim 1/Q^4$, and $F_2/F_1 \sim 1/Q^2$.

In more recent years, extended VMD fits which provide a relatively good parameterization of all nucleon e.m. FFs have been obtained. An example is Lomon's fit [Lom01], which uses $\rho(770)$, $\omega(782)$, $\phi(1020)$, and $\rho'(1450)$ mesons and contains 11 parameters. Another such recent parameterization by Björker and Iachello [Bij04] including $\rho(770)$, $\omega(782)$, and $\phi(1020)$ mesons only achieves a good fit by adding a phenomenological contribution attributed to a quarklike intrinsic qqq structure (of *rms* radius ~ 0.34 fm) besides the vector-meson exchange terms. The pQCD scaling relations are built into this fit which has 6 free parameters which are fit to the data. In contrast to the early fit of Ref. [Iac73], the new fit of Ref. [Bij04] gives a very good description of the neutron data at the expense of a slightly worse fit for the proton data.

It will be interesting to check the resulting VMD fits for the neutron FFs to larger Q^2 . In this regard, an interesting “prediction” can be drawn when the FFs F_2 and F_1 obtained directly from double polarization experiments are shown in the same graph for the proton and the neutron, as in Fig. 31. It is remarkable that both F_1 and F_2 tend toward the same value for proton and neutron, and may meet at a Q^2 value which will soon be accessible for the neutron. This conclusion is influenced by the VMD fits shown in the same figure, and rests on their extrapolation for the neutron to larger Q^2 . Note that the VMD fits shown include all data for p and n, but selects the recoil polarization over the Rosenbluth results for Q^2 larger than 1 GeV^2 .

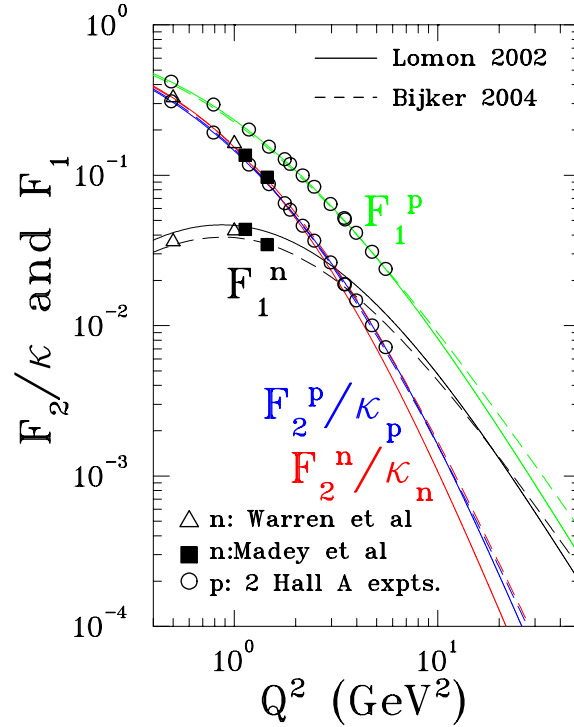


Figure 31: The ratio F_2/F_1 for the proton and the neutron obtained from double polarization experiments only. The curves are the VMD fits of Lomon [Lom01] and of Bijker and Iachello [Bij04].

4.1.2 Dispersion analyses

Despite the relatively good fits obtained by the VMD models, it was already pointed out in 1959 by Frazer and Fulco [Fra59] that such an approach is at odds with general constraints from unitarity. Assuming an unsubtracted dispersion relation (DR), the nucleon e.m. FFs $F(q^2)$, where F generically stands for any of the four FFs, can be obtained as :

$$F(q^2) = \frac{1}{\pi} \int_{t_0}^{\infty} dq'^2 \frac{\text{Im}F(q'^2)}{q'^2 - q^2}. \quad (44)$$

The dispersion analyses are performed separately for nucleon isoscalar and isovector FFs, defined in Eqs. (12,13). In the vector-isovector spectral function $\text{Im}F(q'^2)$ one notices a large non-resonant contribution starting from

$t_0 = 4m_\pi^2$ and extending under the ρ -peak. Such a non-resonant contribution arises due to the two-pion continuum. For the isoscalar spectral function, the integral starts at $t_0 = 9m_\pi^2$, corresponding with 3π intermediate states. The two-pion continuum contribution was estimated by Höhler and collaborators [Hoh76] by using pion time-like FF data and $\pi\pi \rightarrow N\bar{N}$ amplitudes which were determined by extrapolating πN partial waves to the time-like region [Hoh75].

Höhler's analysis has been updated by Mergell, Meissner, and Drechsel [Mer96] in the mid-nineties and extended to include the nucleon time-like FF data [Ham96]. The inclusion of recent neutron FF data in such dispersion relation analysis has been performed in Ref. [Ham04]. The resulting analysis describes the nucleon isovector FFs through the 2π continuum (including the $\rho(770)$), and three additional vector isovector meson poles : $\rho'(1050)$, $\rho''(1465)$, $\rho'''(1700)$. The isoscalar FFs are described by four vector isoscalar meson poles : $\omega(770)$, $\phi(1020)$, $S'(1650)$ and $S''(1680)$. In this approach, the masses of the mesons ρ' , ρ'' , ρ''' , S' , S'' and the 14 residua (one for both the vector (F_1) and tensor (F_2) channels for each meson) are fitted and the pQCD scaling behavior is parameterized through three additional parameters. Note that for the isovector channel, the fitted masses for ρ'' and ρ''' correspond with physical particles listed by the Particle Data Group (PDG), whereas enforcing the correct normalization of all FFs, the experimental value for the neutron charge radius, as well as the pQCD scaling behavior, requires the inclusion of an unphysical ρ' meson with mass 1050 MeV. The analysis of Hammer and Meissner [Ham04] also finds that the residua for both isovector FFs F_1^V and F_2^V of ρ'' and ρ''' are relatively close in magnitude and opposite in sign, required by the approximate dipole behavior of the isovector FFs. For the isoscalar FFs F_1^S and F_2^S , the fit also drives the residua of the nearby poles S' and S'' to values very close in magnitude and of opposite signs, required by the approximate dipole behavior of the isoscalar FFs. Using such an analysis, Ref. [Ham04] obtained a good description of most FF data with the exception of the G_{Ep}/G_{Mp} polarization data at $Q^2 > 3 \text{ GeV}^2$, which is overpredicted.

The dispersion relation analysis of nucleon e.m. FFs has been further improved by Belushkin *et al.* [Bel06]. In addition to the 2π continuum present in the isovector spectral functions of the previous DR analyses, also the $\rho\pi$ and $K\bar{K}$ continua were included as independent input in the isoscalar spectral functions. In Ref. [Bel06], the 2π continuum was reevaluated using the latest experimental data for the pion FFs in the time-like region [Bel05]. The $K\bar{K}$ continuum was obtained from an analytic continuation of KN scattering data [Ham99]. Following the work of Ref. [Mei97], the $\rho\pi$ continuum was approximated in the DR analysis by an effective pole term for a fictitious ω' meson with mass : $m_{\omega'} = 1.12 \text{ GeV}$. This approximate $\rho\pi$ continuum is found to yield an important negative contribution to F_1^S . The remaining contributions to the spectral functions are parameterized by vector meson poles from a fit to the FF data. The parameters in the fit were constrained to yield the correct normalization of the FFs at zero momentum transfers. The asymptotic constraints from pQCD were included in two different forms : either as a superconvergence relation or by adding an explicit continuum term with the imposed pQCD behavior. A simultaneous fit to the world data for all four FFs in both the space-like and time-like regions was performed. Fig. 32 shows this fit for the nucleon space-like FFs where for G_{Ep}/G_{Mp} at larger Q^2 the JLab/Hall A polarization data have been used, and were for G_{Mn} the preliminary JLab/CLAS data [Bro05b] have been included. In this fit, the pQCD limit was imposed through an explicit continuum term and the minimum number of poles in addition to the $\pi\pi$, $\rho\pi$ and $K\bar{K}$ continua were chosen to fit the data. In addition to the $\omega(782)$, the fit yields two more isoscalar poles ($m_{s1} \simeq 1.05 \text{ GeV}$ and $m_{s2} \simeq 1.4 \text{ GeV}$), and three additional isovector poles ($m_{v1} \simeq 1.0 \text{ GeV}$, $m_{v2} \simeq 1.6 \text{ GeV}$, and $m_{v3} \simeq 1.8 \text{ GeV}$). The resulting 15 parameter fit shown in Fig. 32 has a total $\chi^2/\text{d.o.f.}$ value of 2.2.

It will be interesting to confront the most recent and sophisticated DR fit of Ref. [Bel06] with upcoming data for G_{Ep}/G_{Mp} out to 8.5 GeV^2 [Bra04]. In all discussed VMD and DR fits starting with Gari-Krümpelmann [Gar85] the asymptotic pQCD limit $F_2/F_1 \sim 1/Q^2$ was built in, although the data do not

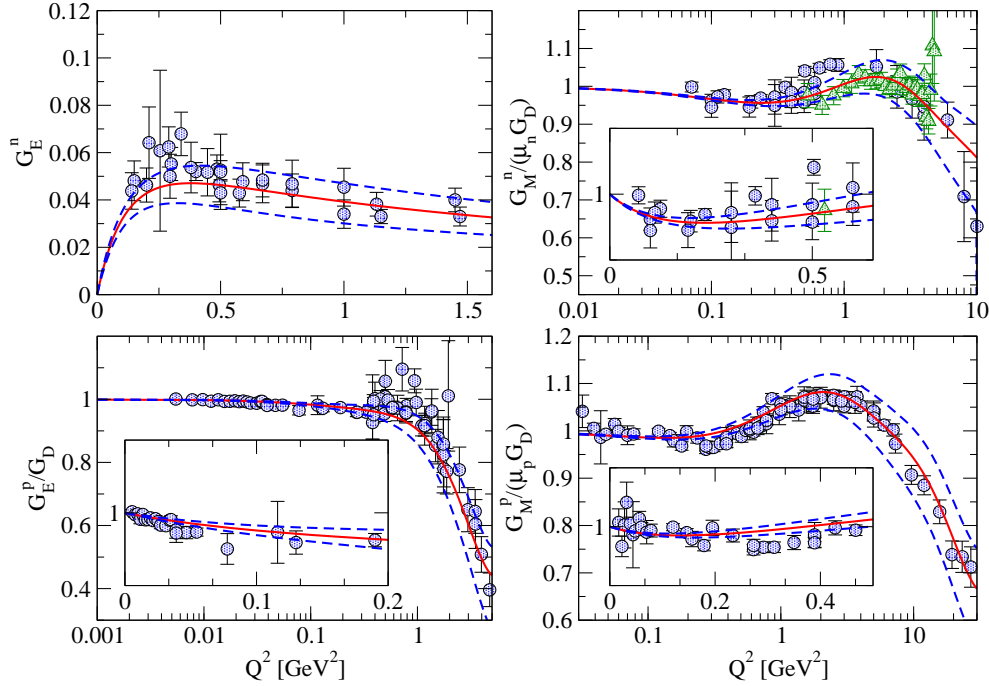


Figure 32: Dispersion relation (15 parameter) fit for the four nucleon (space-like) e.m. FFs compared with the world data (circles) including the JLab/CLAS data for G_{Mn} (triangles) [Bro05b]. The dashed curves indicate the 1σ deviation from the fit, given by the solid curves. Figure from Ref. [Bel06].

support this limit at available momentum transfers, see Fig.54 in Sect. 4.7. Besides, there is various theoretical work indicating that the pQCD prediction, in particular for F_{2p} , might only set in at significantly larger values of Q^2 , of the order of several tens of GeV^2 . It might therefore be worthwhile to investigate how the DR analysis changes by removing the bias $F_2/F_1 \sim 1/Q^2$ from the analysis, when fitting data in the range up to $Q^2 \sim 10 \text{ GeV}^2$.

4.2 Quark models versus pion-cloud models

4.2.1 Non-relativistic constituent quark models

In our quest to understand the structure of the nucleon in terms of the quark and gluon degrees of freedom which appear in the QCD Lagrangian, constituent quark models (CQMs) have a long history, which predates the establishment of the theory of strong interactions, QCD. In a CQM, the nucleon appears as the ground state of a quantum-mechanical three-quark system in a confining potential. In such a picture, the ground state baryons (composed of the light up (u), down (d) and strange (s) quark flavors) are described by $SU(6)$ spin-flavor wave functions, supplemented by an antisymmetric color wave function.

In the Isgur-Karl model [Isg78], the constituent quarks move in a harmonic oscillator type confining potential. For the ground state baryons, the three constituent quarks are in the $1s$ oscillator ground state, corresponding with the $[56]$ -plet of $SU(6)$. The harmonic oscillator states can be represented by $|B^{2S+1}L_J\rangle_t$, where B stands for either N or Δ states, S specifies the spin, L the orbital angular momentum ($L = S, P, D, \dots$ in the common spectroscopic notation), and J the total angular momentum of the three-quark state. Further-

more, $t(= S, M, A)$ refers to the symmetry type : symmetric (S), mixed symmetric (M) or anti-symmetric (A) under exchange of the quarks in both the spin-flavor and space parts of the baryon wave function. In the Isgur-Karl model, the long-range confining potential is supplemented by an interquark force corresponding with one-gluon exchange. The one-gluon exchange leads to a color hyperfine interaction between quarks i and j of the form:

$$H_{hyperfine}^{ij} = \frac{2}{3} \frac{\alpha_s}{m_i m_j} \left\{ \frac{8\pi}{3} \mathbf{S}_i \cdot \mathbf{S}_j \delta^3(\mathbf{r}_{ij}) + \frac{1}{r_{ij}^3} \left[\frac{3(\mathbf{S}_i \cdot \mathbf{r}_{ij})(\mathbf{S}_j \cdot \mathbf{r}_{ij})}{r_{ij}^2} - \mathbf{S}_i \cdot \mathbf{S}_j \right] \right\}, \quad (45)$$

with α_s the strong coupling constant, $\mathbf{S}_i(m_i)$ the spin (mass) of quark i , and where $\mathbf{r}_{ij}(r_{ij})$ specify the vector (distance) between quarks i and j . The first term in Eq. (45) corresponds with a zero-range spin-spin interaction, whereas the second term corresponds with a tensor force. The color hyperfine interaction of Eq. (45) breaks the $SU(6)$ symmetry and leads to a mass splitting between $N(939)$ and $\Delta(1232)$, often referred to as the hyperfine splitting. It was found that it also predicts well the mass splittings between octet and decuplet baryons [DeR75]. Furthermore, the tensor force in Eq. (45) will produce a D -state ($L = 2$) admixture in the N (as well as Δ) ground states [Kon80, Isg82]. Because of this hyperfine interaction, the $N(939)$ is described as a superposition of $SU(6)$ configurations. Including configurations up to the $2\hbar\omega$ oscillator shell, they are given by (using the spectroscopic notation mentioned above) :

$$|N(939)\rangle = a_S |N^2 S_{1/2}\rangle_S + a'_S |N^2 S'_{1/2}\rangle_S + a_M |N^2 S_{1/2}\rangle_M + a_D |N^4 D_{1/2}\rangle_M. \quad (46)$$

By diagonalizing the hyperfine interaction and fitting the results to the baryon spectrum, Isgur *et al.* [Isg82] obtained the following values for the wave-function coefficients:

$$a_S \simeq 0.93, \quad a'_S \simeq -0.29, \quad a_M \simeq -0.23, \quad a_D \simeq -0.04. \quad (47)$$

From these values it is evident that the S -wave component dominates the N wave function in a constituent quark model. Using $SU(6)$ spin-flavor symmetry, *i.e.*, setting $a_S = 1$ and $a'_S = a_M = a_D = 0$ in Eq. (46), yields for the ratio of proton to neutron magnetic moments :

$$\frac{\mu_p}{\mu_n} = -\frac{3}{2}, \quad (\text{SU(6)-symmetric quark model}), \quad (48)$$

within 3 % of the empirical number.

The small non-zero values of a_D in Eq. (47) implies that the D -wave probability in the nucleon ground state is below 1 %. As a result of such D -wave components in a wave function, charge densities of baryons become non-spherical. For a static charge distribution, a measure of the non-sphericity (or deformation) is given by its quadrupole moment. Since the nucleon has spin 1/2, any intrinsic quadrupole moment of the nucleon cannot be directly measured because angular momentum conservation forbids a non-zero matrix element of a ($L = 2$) quadrupole operator between spin 1/2 states. However this quadrupole deformation may reveal itself in an electromagnetically induced transition from the spin 1/2 N to the spin 3/2 Δ state. In this way, the tensor force between quarks gives rise to non-zero values for the electric quadrupole ($E2$) and Coulomb quadrupole ($C2$) transitions¹.

Empirically, the $N \rightarrow \Delta$ quadrupole transitions are found to be a few percent of the dominant $M1 \gamma N \Delta$

¹ The relation between the tensor force, D -wave admixture, and the electromagnetic $N \rightarrow \Delta$ transition was already pointed out in the early paper of Glashow [Gla79].

transition. The $E2 \gamma N \Delta$ transition has been obtained through dedicated measurements of single pion photo-production reactions on the proton [Bec97, Bla97], and as a result of such measurements the PDG quotes as value for the $E2/M1$ ratio : $E2/M1 = -(2.5 \pm 0.5) \%$ [Yao06]. This value can equivalently be expressed in terms of a $N \rightarrow \Delta$ transition quadrupole moment as [Tia03] :

$$Q_{p \rightarrow \Delta^+} = -(0.0846 \pm 0.0033) \text{ fm}^2. \quad (49)$$

4.2.2 Relativistic constituent quark models

The non-relativistic CQM, despite its simplicity, is quite successful in predicting the spectrum of low-lying baryons, and gives a relatively good description of static properties such as the octet baryon magnetic moments. To calculate the form factors of a system of constituents with constituent masses small compared with the confinement mass scale necessitates however a relativistic treatment even for low momentum transfers. For momentum transfers several times the nucleon mass squared a relativistic description becomes crucial.

In contrast to the calculation of the spectrum, which uses eigenfunctions of a Poincaré invariant mass operator, a calculation of the nucleon electromagnetic FFs requires the relation between the rest frame spin and momenta (in the three-quark wave function) and those in the moving frame. This requires an extension of eigenfunctions of the spin and mass operators, so as to transform consistently under the unitary representations of the Poincaré group. The way to implement relativity into a Hamiltonian formalism (describing e.g. a system of three interacting constituent quarks) has been laid out by Dirac [Dir49]. There are three *forms of dynamics* (so called instant, point, and light-front forms) which differ in the choice of the kinematical subgroup of the Poincaré group. This is the subgroup of the Poincaré group whose commutator relations are not affected by the interactions between the constituents. The three (unitarily equivalent) forms therefore differ by which of the ten generators of the Poincaré group (four space-time translations, three spatial rotations, and three boosts) are kinematical (i.e. interaction free), and which are dynamical, i.e. depend on the interactions and necessarily have to be approximated in a practical calculation.

In the *instant form*, the dynamical generators are the time component of the four-momentum and the three boost operators. Rotations do not contain interactions, which makes it easy to construct states of definite angular momentum in this form.

In the *point form*, both boosts and rotations are kinematical. The point-form therefore has the important technical advantage that the angular momenta and Lorentz boosts are the same as in the free case. However all four components of the four-vector operator are dynamical in this form.

In the *light-front form*, seven of the generators of the Poincaré group are kinematical (this corresponds to the symmetry group of a null plane), which is the maximum number. The remaining three dynamical generators which contain the interactions are one component of the four-momentum operator (the so-called light-cone Hamiltonian) and 2 transverse rotations. Light-front (as well as point form) calculations for relativistic CQMs are convenient as they allow to boost quark wave functions independently of the details of the interaction. The drawback of the light-front calculations however is that because two generators of rotations are dynamical, the construction of states with good total angular momentum becomes interaction dependent.

Any practical calculation in one of the three forms approximates the current operator. The common (so-called impulse) approximation is that the photon interacts with a single quark in the nucleon.

The light-front form calculation of nucleon FFs has been pioneered by Berestetsky and Terentev [Ber76], and more recently developed by Chung and Coester [Chu91]. In practise one starts from a rest frame nucleon wave function for the three-quark state which ideally is fitted to the baryon spectrum. The nucleon wave function in the light-front form (so-called light-front wave function) is obtained by a Melosh rotation [Mel74]

of each of the quark spinors, connecting the instant and light-front forms. When performing the front form calculation in a (Drell-Yan) frame where the photon light-cone momentum² component $q^+ = 0$, the space-like virtual photon only connects Fock components in the nucleon light-front wave functions with the same number of constituents, i.e. matrix elements between qqq and $qqqq\bar{q}$ states which would be present in an instant form calculation are zero in the light-front calculation. This property allows for a consistent calculation within the light-front formalism when truncating the Fock space to only the three-quark state.

In Ref. [Chu91] a Gaussian wave function in the quark internal (transverse) momentum variables was used. Although this model yields a surprisingly good agreement for the observed G_{Ep}/G_{Mp} ratio, see Fig. 33, it yields nucleon FFs which drop too fast at larger Q^2 values when using constituent quark masses around 330 MeV. Schlumpf [Schl93] allowed for high momentum components in the nucleon light-front wave function by adopting a power law dependence in the quadratic quark internal momentum variables. The two parameters in Schlumpf's wave function were fitted to magnetic moments and semi-leptonic decays of the baryon octet. The resulting e.m. FF calculations reproduce reasonably well the power behavior of the FF at larger Q^2 . The phenomenological wave function of Schlumpf was also used by Frank, Jennings, and Miller [Fra96, Mil02a]. They showed that using a light-front wave function one cannot expect the pQCD prediction of hadron helicity conservation to apply and instead one finds that F_{2p}/F_{1p} drops less fast than $1/Q^2$ [Mil02a] in agreement with the G_{Ep}/G_{Mp} polarization data.

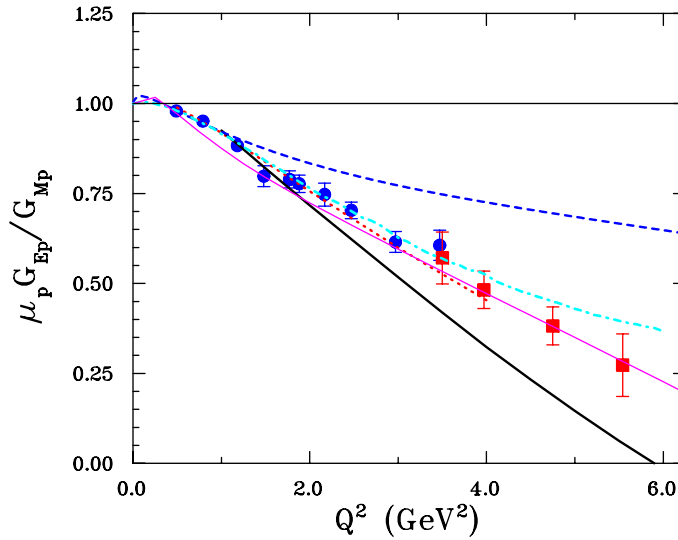


Figure 33: Comparison of relativistic constituent quark model calculations with the data for the ratio $\mu_p G_{Ep}/G_{Mp}$. Dotted curve : front form calculation of Chung and Coester [Chu91] with point-like constituent quarks; thick solid curve : front form calculation of Frank *et al.* [Fra96]; dot-dashed curve : front form calculation of Cardarelli *et al.* [Car95, Car00] with point-like constituent quarks; dashed curve : point form calculation of Boffi *et al.* [Bof01] in the Goldstone boson exchange model with point-like constituent quarks; thin solid curve : covariant spectator model of Gross and Agbakpe [Gro06]. The data are from Refs. [Pun05] (solid circles) and [Gay02] (empty squares).

The wave functions in the calculations described above were however not constructed from a detailed fit

²Defining light-cone components as $x^\pm = (x^0 \pm x^3)/\sqrt{2}$ and defining the null-plane by $x^+ = 0$.

to the baryon spectrum. Cardarelli *et al.* subsequently performed a more “microscopic” light-front calculation [Car95, Car00] where the light-front wave function was obtained from a rest frame wave function which provided a fit to the spectrum. The rest frame wave function was taken from the relativized Capstick-Isgur model [Cap86], based on the picture of three quarks moving in a confinement potential, supplemented by an interquark hyperfine interaction due to one-gluon exchange (OGE), Eq. (45). The parameters were adjusted to fit the baryon spectrum. When expanding this wave function in a harmonic oscillator basis, one obtains a nucleon wave function qualitatively similar to the non-relativistic three-quark state of Eq. (46), and finds a dominant S -wave state with probability : $P_S \simeq 98\%$, and a mixed-symmetric S -wave state S' with probability : $P_{S'} \simeq 1.7\%$. This wave function includes a small non-zero D -wave probability : $P_D \simeq 0.2\%$. Using this wave function, the constituent quark momentum distribution in the nucleon was found to yield an important content of high-momentum components (prominently due to the mixed-symmetry component in the wave function), which are generated by the short-range part of the quark-quark interaction, which is due to one-gluon exchange in the Capstick-Isgur model. These components are completely absent if one only considers the linear confinement potential in the model.

In a CQM calculation, the effect of other degrees of freedom beyond three quarks are buried within the constituent quarks, which are considered as quasi-particles. In the absence of a microscopic calculation, such effects are parameterized in terms of constituent quark form factors. In Ref. [Pet03], it was shown that the data for the proton forward structure function F_2 at low momentum transfers exhibits a new scaling property and can be interpreted as quasi-elastic scattering off extended constituent quarks inside the proton described by a constituent quark FF. The resulting constituent size is around 0.2 - 0.3 fm. Using such effective constituent quark FF in the light-front form calculation of Ref. [Car00], allows a good description of the individual nucleon FFs, see Ref. [Pac00]. Note however that the experimental G_{Ep}/G_{Mp} ratio can basically be reproduced using point-like constituent quarks, see Fig. 33. The suppression of the G_{Ep}/G_{Mp} ratio with respect to the dipole-fit as predicted in the light-front form CQM calculation is attributed to relativistic effects generated by the Melosh rotations of the constituent quark spins. These Melosh rotations introduce kinematical $SU(6)$ breaking effects in addition to the dynamical $SU(6)$ breaking due to the (hyperfine) one-gluon exchange potential.

A comparable amount of high-momentum components in the nucleon wave function was obtained in the Goldstone-boson-exchange (GBE) quark model [Glo98a, Glo98b]. This model relies on constituent quarks and Goldstone bosons, which arise as effective degrees of freedom of low-energy QCD from the spontaneous breaking of the chiral symmetry. The resulting CQM assumes a linear confinement potential supplemented by a quark-quark interaction based on the exchange of pseudoscalar Goldstone bosons, which is the source of the hyperfine interaction. The resulting wave function displays the same basic features as the OGE model, yielding as probabilities for the symmetric (S), and mixed-symmetric (S') components: $P_S \simeq 98.7\%$ and $P_{S'} \simeq 1.3\%$, respectively. It was shown in Refs. [Glo98a, Glo98b] that the GBE CQM yields a unified description of light- and strange-baryon spectra.

The GBE CQM was used in Refs. [Wag01, Bof01] to calculate the nucleon e.m. FFs in the point-form. The neutron charge radius is well described in this model and is driven by the mixed-symmetry component in the neutron wave function. In contrast to the light-front calculation [Car00, Pac00], it was found that when performing a point-form calculation of the nucleon e.m. FFs at larger Q^2 within the impulse approximation, i.e. considering only single-quark currents, a surprisingly good overall description of the nucleon e.m. FFs can be obtained, using point-like constituent quarks only. When looking at details of Refs. [Wag01, Bof01], the agreement is worse though for G_{Mp} which is underpredicted at larger Q^2 , and the ratio of G_{Ep}/G_{Mp} is overpredicted at larger Q^2 , see Fig. 33. Similar findings have also been obtained in the point-form calculation of Ref. [Wag05] for the OGE CQM. The overall success of the point-form result using point-like constituent

quarks was attributed in Refs. [Wag01, Bof01, Wag05] to the major role played by relativity. Such a finding is remarkable in view of the expected finite size of the constituent quarks, as discussed above.

An explanation for the above remarkable finding for the nucleon e.m. FFs in the point form, using the single-quark current approximation, has been suggested by Coester and Riska [Coe03]. When the spatial extent of the three-quark wave function is scaled (unitarily) to zero, both instant- and front-forms yield FFs independent of the momentum transfer. Therefore, to reproduce the experimental fall-off of the nucleon e.m. FFs at large momentum transfers requires the introduction of constituent quark FFs. In contrast, when the wave function in point form is scaled unitarily to zero (so-called point limit), a non-trivial scaling limit is obtained for the FFs, which depends on the shape of the wave function. At high values of momentum transfer, the scaled FFs decrease with an inverse power of the momentum transfer. The corresponding power is determined by the current operator and is independent of the wave function. An explicit comparative calculation of the baryon e.m. FFs between the three different forms was performed in Ref. [Jul04] using a simple algebraic form for the three-quark wave function, which depends on two parameters. It was verified that a qualitative description of the nucleon FF data demands a spatially extended wave function in the instant- and front-form descriptions, in contrast to the point-form description which demands a much more compact wave function.

A manifestly covariant CQM calculation within the Bethe-Salpeter formalism and using an instanton-induced interaction between quarks has been performed by Merten *et al.* [Mer02]. Although this model reproduces the baryon spectrum, it can only qualitatively account for the Q^2 dependence of the nucleon e.m. FFs.

Another covariant CQM calculation was performed by Gross and Agbakpe [Gro06], using a covariant spectator model. Assuming a simple pure S -wave form for the nucleon three-quark wave function, evaluating the current matrix element in a relativistic impulse approximation, and assuming constituent quark FFs including a phenomenological term which parameterizes the pion cloud, an eleven parameter description of the nucleon FF data was obtained, see Fig. 33.

As a next step for CQMs, it would clearly be very worthwhile to investigate the approximations in the current operator within each form. The quality of the commonly made impulse approximation may differ between the different forms. Within the context of a toy model calculation in Refs. [Des04, Des06], it has e.g. been shown that the neglect of two-body currents in the point form does affect the FFs in a more drastic way than their neglect in the instant or light-front forms.

The importance of two-body currents has also been shown in the work of De Sanctis *et al.* [DeS00]. In that work, a calculation within the hypercentral CQM was performed of the (two-body) quark pair contribution to the e.m. current resulting from the one-gluon exchange interaction between the quarks. This pair current contribution was found to lead to a sizeable reduction of G_{Ep} compared with G_{Mp} .

4.2.3 Pion cloud models

Despite their relative success in describing the spectrum and structure of low-lying baryons, models based on constituent quarks alone suffer from evident shortcomings as they do not satisfy all symmetry properties of the QCD Lagrangian. In nature, the up and down (current) quarks are nearly massless. In the exact massless limit, the QCD Lagrangian is invariant under $SU(2)_L \times SU(2)_R$ rotations of left (L) and right (R) handed quarks in flavor space. This *chiral symmetry* is spontaneously broken in nature leading to the appearance of massless Goldstone modes. For two flavors, there are three Goldstone bosons — pions, which acquire a mass due to the explicit breaking of chiral symmetry by the current quark masses.

Since pions are the lightest hadrons, they dominate the long-distance behavior of hadron wave functions and yield characteristic signatures in the low-momentum transfer behavior of hadronic form factors. There-

fore, a natural way to qualitatively improve on the above-mentioned constituent quark models is to include the pionic degrees of freedom. This was done in the already discussed CQM of Refs. [Glo98a, Glo98b], where the quark-quark interaction was provided by the exchange of Goldstone bosons.

An early quark model with implemented chiral symmetry is the *chiral* (or, *cloudy*) *bag model*. This model improves the early MIT bag model by introducing an elementary, perturbative pion which couples to quarks in the bag in such a way that chiral symmetry is restored [Tho82]. Within the cloudy bag model, Lu *et al.* [Lu98] performed a calculation of the nucleon e.m. FFs improving upon previous calculations by applying a correction for the center-of-mass motion of the bag. This calculation also implemented Lorentz covariance in an approximate way by using a prescription for the Lorentz contraction of the internal structure of the nucleon. Using a bag radius $R \simeq 1$ fm, this model provides a good description of the nucleon e.m. FFs in the range $Q^2 < 1 \text{ GeV}^2$.

To extend such a calculation to larger Q^2 , Miller performed a light-front cloudy bag model calculation [Mil02b]. This model extends his earlier calculation [Mil02a] in terms of constituent quarks, described by the light-front wave function of Schlumpf, to include the effects of the pion cloud. The latter are calculated through one-loop diagrams, including relativistic πNN vertex form factors. The model gives a relatively good global account of the data both at low Q^2 and larger Q^2 , though tends to show too much structure around the dipole form for the magnetic form factors at low Q^2 .

Another model which has both quark and pion degrees of freedom and interpolates between a constituent quark model and the Skyrme model (where the nucleon appears as a soliton solution of an effective nonlinear pion field theory) is the *chiral quark soliton model* (χ QSM). This model is based on the interaction of quarks with Goldstone bosons resulting from the spontaneous breaking of chiral symmetry. As for the Skyrme model, the χ QSM is essentially based on a $1/N_c$ expansion (with N_c the number of colors in QCD). Its effective chiral action has been derived from the instanton model of the QCD vacuum [Dia86], which provides a natural mechanism of chiral symmetry breaking and enables one to generate dynamically the constituent quark mass.

Although in reality the number of colors N_c is equal to three, the extreme limit of large N_c is known to yield useful insights. At large N_c the nucleon is heavy and can be viewed as N_c “valence” quarks bound by a self-consistent pion field (the “soliton”) whose energy coincides with the aggregate energy of the quarks of the negative-energy Dirac continuum [Dia88]. A successful description of static properties of baryons, such as mass splittings, axial constants, magnetic moments, form factors, has been achieved (typically at the 30 % level or better, see Ref. [Chr96] for a review of early results). After reproducing masses and decay constants in the mesonic sector, the only free parameter left to be fixed in the baryonic sector is the constituent quark mass. In Ref. [Chr95], the χ QSM was applied to the calculation of the nucleon e.m. FFs. When taking rotational ($1/N_c$) corrections into account, this model achieved a qualitative good description of the nucleon e.m. FFs in the range $Q^2 < 1 \text{ GeV}^2$, using a constituent quark mass around 420 MeV.

The chiral soliton model naturally accounts for the decrease of the G_{Ep}/G_{Mp} ratio with increasing Q^2 . This can be understood from the hedgehog structure in soliton models which couples spatial rotations with isorotations. In the soliton rest frame, the isovector electric FF G_E^V therefore measures the rotational inertia density $\rho^V(r)$, in contrast to the isoscalar electric FF G_E^S which measures the isoscalar baryon density $\rho^S(r)$. For a rigid rotor, the inertia density is obtained from the baryon density as $\rho^V = r^2/r_B^2 \rho^S$, with r_B a free parameter characterizing the spatial extent. Assuming a Gaussian density for $\rho^S(r)$, this relation translates into the form factor relation :

$$G_E^V(Q^2) = \left(1 - \frac{1}{9}Q^2 r_B^2\right) G_E^S(Q^2), \quad (50)$$

which yields for G_{Ep} , using Eq.(13) :

$$G_{Ep}(Q^2) = \left(1 - \frac{1}{18}Q^2 r_B^2\right) G_E^S(Q^2). \quad (51)$$

In the pure pionic soliton model and for a Gaussian baryon density $\rho^S(r)$, one furthermore finds that the relation $G_{Mp}(Q^2) = \mu_p G_E^S(Q^2)$ is satisfied to good accuracy, yielding :

$$\frac{\mu_p G_{Ep}(Q^2)}{G_{Mp}(Q^2)} = \left(1 - \frac{1}{18}Q^2 r_B^2\right). \quad (52)$$

With the choice $r_B^2 \approx (0.3 \text{ fm})^2$, one can obtain an excellent fit of the polarization data for G_{Ep}/G_{Mp} , see Fig. 34. Although in the chiral soliton model calculation the baryon density is not exactly Gaussian, and the rigid rotor calculation does not hold exactly, these relations can be considered as approximate relations [Hol96].

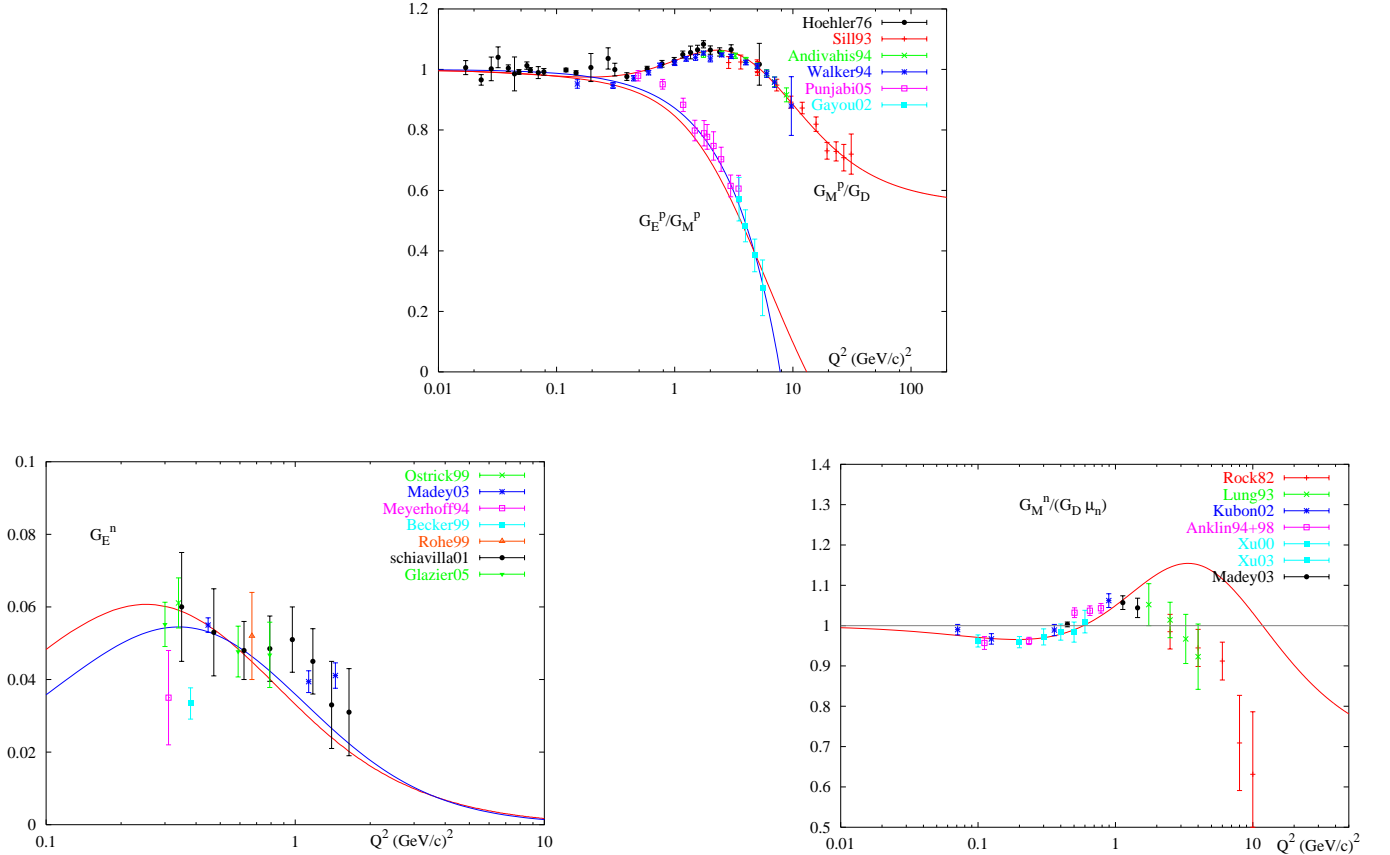


Figure 34: Nucleon e.m. FF calculations for proton (top panel) and neutron (lower panels) in the chiral soliton model [Hol96, Hol05]. For $\mu_p G_{Ep}/G_{Mp}$, the blue curve which fits the data is obtained from Eq. (52) for $r_B = 0.3 \text{ fm}$. For G_{En} the blue curve is the Galster parameterization [Gal71]. Figure from Ref. [Hol05].

Holzwarth [Hol96] extended the chiral soliton model by including the $\rho(\omega)$ meson propagators for the isovector (isoscalar) channels respectively. Furthermore, to extend the range in Q^2 of the predictions, he uses

a relativistic prescription to boost the soliton rest frame densities to the Breit frame. This prescription which is also used to extract radial charge and magnetization rest frame densities from experimental form factors will be explained in more detail in Sect. 4.3. Holzwarth takes the mass parameter which appears in the boost to be different from the nucleon mass M and treats it as a fit parameter. Using 4 fit parameters (one effective boost mass and three free parameters to fix the couplings of ρ and ω mesons), the resulting proton and neutron e.m. FFs are shown in Fig. 34. One sees that the model gives a good account of the detailed structure of the nucleon e.m. FFs in the low Q^2 region. In particular, for G_{Ep}/G_{Mp} it yields a decreasing ratio in good agreement with the data. At larger Q^2 , the boost prescription gives a reasonably good account of the data (except for G_{Mn}) and predicts a zero in G_{Ep} around 10 GeV². Due to the uncertainty introduced from the particular choice for the boost prescription, the high Q^2 behavior (for Q^2 larger than about $4M^2$) of the e.m. FFs is however not a profound prediction of the low-energy effective model. It is interesting to note however that the chiral soliton model calculation was one of the few calculations which truly predicted the decrease of G_{Ep}/G_{Mp} with increasing Q^2 . At the time of its prediction [Hol96], this was at variance with the available Rosenbluth data, and was only confirmed once the polarization data became available a few years later.

Recently, the nucleon e.m. FFs were calculated in a Lorentz covariant chiral quark approach [Fae06], where baryons are modeled as bound states of constituent quarks dressed by a cloud of pseudoscalar mesons. Although bare constituent quark FFs are fully parameterized in this approach in terms of 10 parameters, it was also found that a description of the nucleon e.m. FFs requires the inclusion of the meson-cloud contributions.

4.3 Radial distributions and shape of the nucleon

4.3.1 Radial distributions of charge and magnetization

As discussed in Sect. 2.1.4, in the Breit frame the nucleon charge operator depends only on the electric FF G_E , whereas the e.m. three-current operator depends only on the magnetic FF G_M . This suggests to interpret the Fourier transforms of G_E (G_M) as the nucleon charge (magnetization) densities. This identification is only appropriate for a non-relativistic (static) system however, as in general there is a variation of the Breit frame with Q^2 . For the nucleon, where form factor data have been obtained for Q^2 values much larger than M_N^2 , one needs to take the effect of relativity into account. Recently Kelly [Kel02] has used a relativistic prescription to relate the Sachs form factors to the nucleon charge and magnetization densities, which takes into account the Lorentz contraction of the densities in the Breit frame relative to the rest frame.

One starts from the spherical nucleon charge $\rho_{ch}(r)$ and magnetization $\rho_m(r)$ densities in the nucleon rest frame. These densities are normalized so as to yield the total charge for ρ_{ch} , or one for ρ_m (the magnetic moment is taken out of the density) as :

$$\begin{aligned} \int_0^\infty dr r^2 \rho_{ch}(r) &= Z, \\ \int_0^\infty dr r^2 \rho_m(r) &= 1, \end{aligned} \tag{53}$$

where $Z = 0, 1$ is the nucleon charge. From these intrinsic (rest frame) densities, one can construct intrinsic form factors $\tilde{\rho}(k)$ which are related through a Fourier-Bessel transform as :

$$\begin{aligned}\tilde{\rho}(k) &\equiv \int_0^\infty dr r^2 j_0(kr) \rho(r), \\ \rho(r) &= \frac{2}{\pi} \int_0^\infty dk k^2 j_0(kr) \tilde{\rho}(k),\end{aligned}\tag{54}$$

with $k \equiv |\vec{q}|$ is the wave vector in the nucleon rest frame. For a non-relativistic system, the intrinsic FFs are obtained from the Sachs form factors using $k \rightarrow Q$ as : $\tilde{\rho}_{ch}(k) \rightarrow G_E(Q^2)$, and $\mu_N \tilde{\rho}_m(k) \rightarrow G_M(Q^2)$.

To properly relate the intrinsic FFs evaluated in the rest frame to the Breit frame, where the nucleon moves with velocity $v = \sqrt{\tau/(1+\tau)}$ relative to the rest frame, with $\tau \equiv Q^2/(4M^2)$, involves a Lorentz boost with :

$$\gamma^2 = (1 - v^2)^{-1} = 1 + \tau.\tag{55}$$

This Lorentz boost leads to a contraction of the nucleon densities as seen in the Breit frame. Consequently, in the Fourier-transforms, this amounts to replace in the intrinsic FF arguments :

$$k^2 \rightarrow \frac{Q^2}{1 + \tau}.\tag{56}$$

To relate intrinsic form factors $\tilde{\rho}(k)$ with the Sachs form factors $G(Q^2)$ is not unambiguous however because the boost operator for a composite system depends on the interactions among its constituents. There exist different prescription in the literature which can be written in the form :

$$\tilde{\rho}_{ch}(k) = \gamma^{2n_E} G_E(Q^2) = (1 + \tau)^{n_E} G_E(Q^2),\tag{57}$$

$$\mu_N \tilde{\rho}_m(k) = \gamma^{2n_M} G_M(Q^2) = (1 + \tau)^{n_M} G_M(Q^2),\tag{58}$$

where k and Q^2 are related as in Eq. (56). For $Q^2 \rightarrow \infty$, the boost maps $G(Q^2 \rightarrow \infty)$ to $\tilde{\rho}(2M)$. One thus sees that there is a limiting wave vector $k_{max} = 2M$ determined by the nucleon Compton wavelength. In the rest frame, no information can be obtained on distance scales smaller than the Compton wavelength due to relativistic position fluctuations (also known as the *Zitterbewegung*). To account for the proper asymptotic $1/Q^4$ FF behavior of the nucleon e.m. FFs, Mitra and Kumari [Mit77] proposed the choice $n_E = n_M = 2$ ³. Kelly followed this choice when extracting the rest frame densities from the measured nucleon e.m. FFs in Ref. [Kel02].

In his analysis, Kelly furthermore minimized the model dependence of the fitted densities by using an expansion in a complete set of radial basis functions. For $Q^2 > 1 \text{ GeV}^2$ the G_{Ep} analysis used recoil polarization data from JLab [Jon00, Gay02] rather than the Rosenbluth separation data. Fig. 35 compares the fitted charge and magnetization densities for neutron and proton. The uncertainty bands include both statistical and incompleteness errors. The excess of negative charge near $r \sim 0.8 - 1.0 \text{ fm}$ is a characteristics of the π^- -meson cloud in the neutron. The proton charge density is significantly broader than the magnetization density, a direct consequence of G_{Ep} being softer than G_{Mp} in Q^2 -space.

To investigate the pion cloud as revealed through the neutron electric charge distribution further, Friedrich and Walcher [Fri03] have performed a phenomenological analysis of all four nucleon e.m. FFs. They performed a two-component fit of the four FFs starting from a smooth part (parameterized by a sum of two

³Note that this is also the choice made by Holzwarth [Hol05] in the most recent evaluation of the nucleon e.m. FFs in the chiral soliton model.

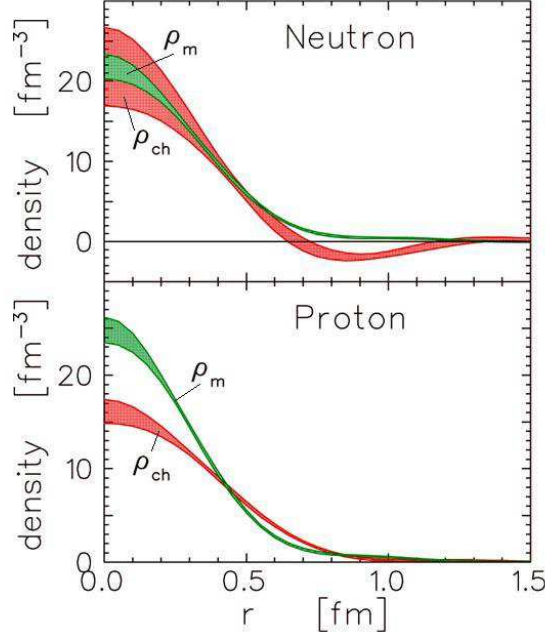


Figure 35: Radial distributions of charge ρ_{ch} and magnetization ρ_m in the proton and neutron from Ref. [Kel02]. These were obtained from the Fourier Bessel transforms Eq. (54) using the relativistic transformation of Eqs. (57,58) with $n_E = n_M = 2$, to relate the Sachs FFs to the intrinsic (rest frame) FFs. Note that the neutron charge distribution has been multiplied by a factor of 6 to emphasize the similarity in shape of charge and magnetization densities.

dipoles) and by adding on top of it a Gaussian “bump” structure. The choice of such a two-component form was triggered by the behavior of G_{En} at small Q^2 , and by the observation of the noticeable oscillations of the other three e.m. FFs around the dipole form. Their parameterization allows for 6 fit parameters for each FF, which provide an excellent fit to the FFs. The bump structure resulting from their fit is shown in Fig. 36. Friedrich and Walcher made the striking observation that all four FFs display such a bump structure around $Q^2 \approx 0.25 \text{ GeV}^2$. They interpret this structure as a signature of the pion cloud. Upon Fourier transforming, the corresponding Breit-frame densities, corresponding with the “bump” structure in the FFs, were found to extend as far out as 2 fm. It is interesting to compare this with the findings of the dispersion theory, in which the longest range part of the pion cloud contribution to the nucleon e.m. FFs is given by the 2π continuum. These 2π continuum contribution were found to be much more confined in coordinate space [Bel05]. In order to get a bump structure in G_{En} in the DR theory requires to introduce additional strength in the spectral functions below 1 GeV. New high precision data for G_{Ep}/G_{Mp} from the BLAST experiment at MIT-Bates [Cra06], shown in Fig. 23, confirms the dip structure around $Q^2 \approx 0.3 \text{ GeV}^2$. It will also be interesting to compare upcoming data of BLAST for G_{En} in the same range with a parameterization as in Fig. 36⁴.

⁴Preliminary data indicates that a bump structure for G_{En} is indeed present around $Q^2 \approx 0.3 \text{ GeV}^2$ [Wal06].

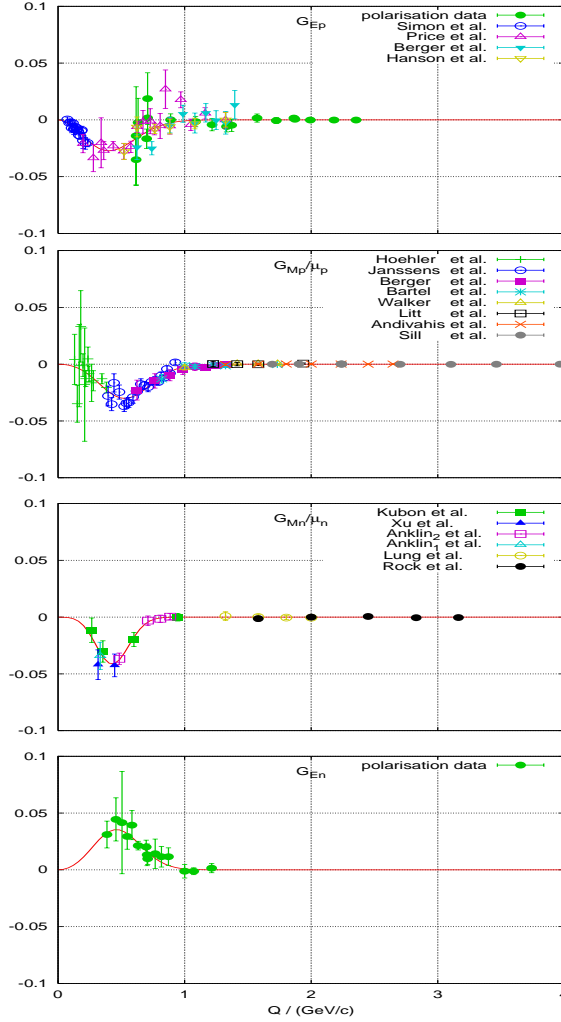


Figure 36: Phenomenological two-component fit of the nucleon e.m. FFs according to Friedrich and Walcher [Fri03]. The 6-parameter fit for each FF consists of a smooth part, described by a sum of two dipoles, and a Gaussian bump part. The latter is displayed in the figure.

4.3.2 Intrinsic quadrupole moment and the shape of the nucleon

The information on the shape of a charge distribution is encoded in its quadrupole moment. Buchmann and Henley [Buc01] discussed the intrinsic quadrupole moment of a baryon state, such as the nucleon or $\Delta(1232)$. The intrinsic quadrupole moment Q^0 of a static charge distribution $\rho_{ch}(\vec{r})$ is given by:

$$Q^0 = \int d^3\vec{r} \rho_{ch}(\vec{r}) (3z^2 - r^2), \quad (59)$$

which is defined w.r.t. the body fixed frame. A charge distribution concentrated along the z -axis (symmetry axis of the system) corresponds with $Q^0 > 0$ (prolate deformation), whereas a charge distribution concentrated in the equatorial xy -plane corresponds with $Q^0 < 0$ (oblate deformation). This intrinsic quadrupole moment has to be distinguished from a measured (or spectroscopic) quadrupole moment Q . As an example, for a rigid rotor (which was considered within the context of the collective nuclear shell model [Boh75]) these quantities

are related as:

$$Q = \frac{3J_z^2 - J(J+1)}{(J+1)(2J+3)} Q^0, \quad (60)$$

where J_z is the projection of the nucleon total spin J onto its symmetry axis (z -axis in a body fixed frame). The difference between Q^0 and Q represents the averaging of the nonspherical charge distribution due to its rotational motion as seen in the laboratory frame. One verifies from Eq. (60) that the multiplication factor is zero for a spin 1/2 particle, yielding $Q_p = 0$ for the proton. Eq. (60) does not preclude however that the proton has an intrinsic quadrupole moment Q_p^0 .

Within a model where the nucleon consists of a spherically symmetric quark core surrounded by a pion with orbital angular momentum $l = 1$, Buchmann and Henley expressed the proton and Δ^+ intrinsic quadrupole moments in terms of the neutron charge radius as [Buc01]:

$$Q_{\Delta^+}^0 = \langle r^2 \rangle_{En} = -Q_p^0. \quad (61)$$

Thus, the proton and Δ^+ have respectively a prolate and an oblate intrinsic deformation. In this hybrid (quark/pion-cloud) model, the pion cloud is fully responsible for the non-zero values of the quadrupole moments Q_p^0 and $Q_{\Delta^+}^0$, and hence for the non-spherical shape of these particles.

Estimates such as Eq. (61) of intrinsic quadrupole moments are surely useful to reveal details of a given model calculation and gain physical insight. One should keep in mind, however, that, even though a specific model such as the rigid rotor relates the intrinsic and total quadrupole moments, only the latter is directly related to observables. The Δ quadrupole moment and $N \rightarrow \Delta$ transition quadrupole moments are therefore observables. For the nucleon, which has no observable quadrupole moment, one should keep in mind that the intrinsic quadrupole moment is a model dependent concept.

Miller [Mil03] has defined spin-dependent quark densities as matrix elements of density operators in proton states of definite spin-polarization. Within a constituent quark picture, the spin-dependent density operator for a quark in the proton to be found at position \mathbf{r} and with spin-direction $\hat{\mathbf{n}}$ is given by :

$$\hat{\rho}(\mathbf{r}, \hat{\mathbf{n}}) = \sum_i \frac{e_i}{e} \delta(\mathbf{r} - \mathbf{r}_i) \frac{1}{2} (1 + \sigma_i \cdot \hat{\mathbf{n}}), \quad (62)$$

where the sum runs over the three constituent quarks i with fractional charge e_i/e . Relative to the spin-direction $\hat{\mathbf{s}}$ of the proton, Miller then studied the distribution of quarks for different quark spin orientations $\hat{\mathbf{n}}$. The so defined densities may become non-spherical as shown in Refs. [Mil03, Kvi06]. Averaging over quark spin $\hat{\mathbf{n}}$ or over nucleon spin $\hat{\mathbf{s}}$ yields a spherical distribution [Gro06].

4.4 Chiral perturbation theory

At low momentum transfers Q^2 , the nucleon e.m. FFs can also be studied within chiral perturbation theory (χ PT) expansions based on chiral Lagrangians with pion and nucleon fields. In χ PT, the short-distance physics is parameterized in terms of low-energy-constants (LECs) which ideally can be determined by matching to QCD but in practice are fitted to experiment. In the calculation of the nucleon e.m. FFs, the LECs can be fitted to the nucleon charge radii and the anomalous magnetic moments. Once they are fixed, the Q^2 dependence of the FFs follows as a prediction.

To calculate the nucleon e.m. FFs in χ EFT involves a simultaneous expansion in soft scales : Q^2 and

m_π , which are understood to be small relative to the chiral symmetry breaking scale $\Lambda_{\chi SB} \sim 1$ GeV. Several expansion schemes (also called power-counting schemes) have been developed in the literature. They all yield the same non-analytic dependencies (e.g. terms proportional to m_π , m_π^3 , $m_\pi^2 \ln m_\pi^2$, ...) but differ in analytic terms (e.g. terms proportional to m_π^2 , m_π^4 , ...).

Because the first nucleon excitation, the $\Delta(1232)$ resonance, has an excitation energy of only about $\Delta \equiv M_\Delta - M \simeq 300$ MeV, the Δ resonance is often included as an explicit degree of freedom in the theory. The resulting chiral effective theory (χ EFT) includes pion, nucleon, and Δ fields. When including the Δ as an explicit degree of freedom in the chiral Lagrangian, the counting scheme has to specify how the expansion parameter $\varepsilon \equiv m_\pi/\Lambda_{\chi SB}$ is counted relative to $\delta \equiv \Delta/\Lambda_{\chi SB}$. In the small scale expansion (SSE) [Hem97], also called ε -expansion, the pion mass and the $M_\Delta - M_N$ mass difference are counted on the same footing, i.e. $\varepsilon \sim \delta$. The recently developed δ -expansion scheme, see Ref. [Pas06b] for a review and applications, counts the pion mass as $\varepsilon \sim \delta^2$, which is the closest integer power relation between these parameters in the real world.

Early calculations of the nucleon e.m. FFs in the SSE at order ε^3 have been performed in Ref. [Ber98]. Because such an approach is based on a heavy baryon expansion it is limited to Q^2 values much below 0.2 GeV^2 .

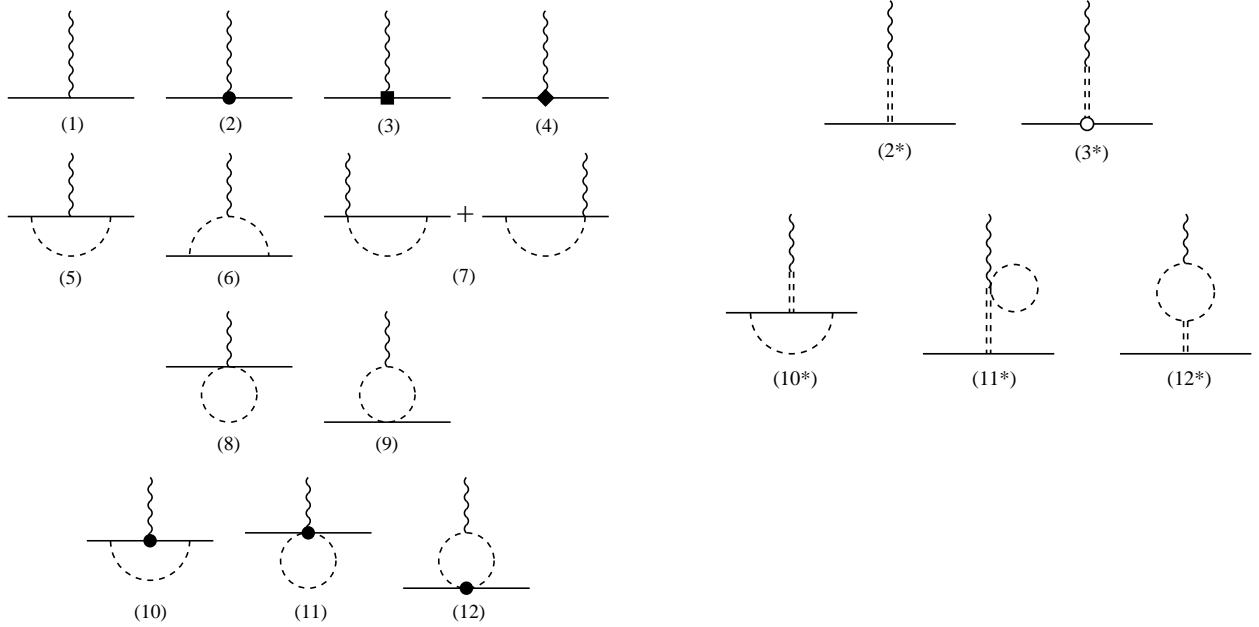


Figure 37: The Feynman diagrams calculated in relativistic χ PT to fourth order [Kub01]. Left diagrams show LECs (1-4) as well as one-loop diagrams (5-12) involving pions (dashed lines), nucleons (solid lines) and photons (wiggly lines). The dots/squares/diamonds refer to insertions of second/third/fourth order in the chiral Lagrangian. Right diagrams are the vector meson (indicated by double dashed lines) contributions to fourth order included in the calculation of Ref. [Kub01].

Subsequently, several calculations of the nucleon e.m. FFs have been performed in manifestly Lorentz invariant χ PT. Kubis and Meissner [Kub01] performed a calculation to fourth order (p^4) in relativistic baryon χ PT, employing the infrared regularization scheme. To this order, this corresponds with the pion loop diagrams of Fig. 37. They showed that the convergence of the chiral expansion is improved as compared to a heavy baryon χ PT results. Schindler *et al.* [Schi05] also performed a manifestly Lorentz invariant calculation to

fourth order, employing the extended on-mass shell renormalization scheme. Both groups found that when including pion and nucleon degrees of freedom alone, one is not able to describe the nucleon e.m. FFs over any significant range of Q^2 . In both calculations, the proton electric FF would cross zero for Q^2 values as low as 0.4 GeV^2 . Both calculations also confirm that a realistic description of the nucleon e.m. FFs is only obtained once the vector mesons are included as explicit degrees of freedom in the chiral Lagrangian. The vector meson loop diagrams were found to play only a minor role, the dominant contribution coming from the pole diagrams shown in Fig. 37, confirming the findings of VMD models and dispersion theory.

The corresponding results for the four nucleon e.m. FFs in the covariant baryon χ PT including vector mesons of Ref. [Kub01] are shown in Fig. 38 at both third and fourth order. The electric FFs of proton and neutron require fixing one LEC for each, corresponding with the charge radii. One sees from Fig. 38 that the resulting fourth order results, including vector mesons, give a good description of the Q^2 dependence of the data up to Q^2 around 0.4 GeV^2 . For the magnetic FFs, at third order the two LECs are fixed from the corresponding proton and neutron magnetic moments, whereas at fourth order two more LECs are fixed from the magnetic radii. Also for the magnetic FFs, a good description is only obtained once the vector mesons are included. Schindler *et al.* [Schi05] confirmed this finding and were also able to obtain a good description of all four nucleon e.m. FFs up to Q^2 around 0.4 GeV^2 in a covariant χ PT calculation to fourth order including vector mesons. Again the explicit vector meson contributions were shown to play a major role at the higher end of this momentum transfer range.

In both of the covariant fourth order baryon χ PT calculations described above, the Δ degrees of freedom have been integrated out. A covariant χ PT calculation of the FFs including explicit Δ degrees of freedom would be desirable in the near future.

4.5 Lattice QCD and chiral extrapolation

4.5.1 Lattice simulations

Lattice QCD calculations of nucleon structure quantities have matured considerably in the recent past. They provide an *ab initio* calculation of quantities such as the nucleon electromagnetic form factors from the underlying theory of QCD.

Lattice QCD is a discretized version of QCD formulated in terms of path integrals on a space-time lattice [Wil74] with only parameters the bare quark masses and the coupling constant. One recovers the continuum theory by extrapolating results obtained at finite lattice spacing a to $a = 0$. In order to perform the continuum extrapolation a separate calculation at several values of a is required. As lattice calculations necessarily are performed for a finite lattice size, one must keep the size of the box large enough to fit the hadrons inside the box. This requires to increase the number of sites as one decreases a . On the other hand, to keep finite volume effects small one must have a box that is much larger than the Compton wavelength of the pion. Present lattice QCD calculations take $Lm_\pi \gtrsim 5$ where L is the spatial length of the box and m_π the pion mass. As the computational costs of such calculations increase like m_π^{-9} , one uses quark mass values for the u and d quarks which are larger than in the real world. This enables the inversion of the fermionic matrix, which is needed for the calculation of hadronic matrix elements, with currently available resources.

State-of-the-art lattice calculations for nucleon structure studies use $a \lesssim 0.1 \text{ fm}$ and $L \sim 3 \text{ fm}$ and reach pion mass values down to about 350 MeV . To connect those results with the physical world requires an extrapolation down to the physical quark masses (note that m_q is proportional to m_π^2 for small quark mass values). This so-called chiral extrapolation will be discussed further on. It is only very recently that pion mass values

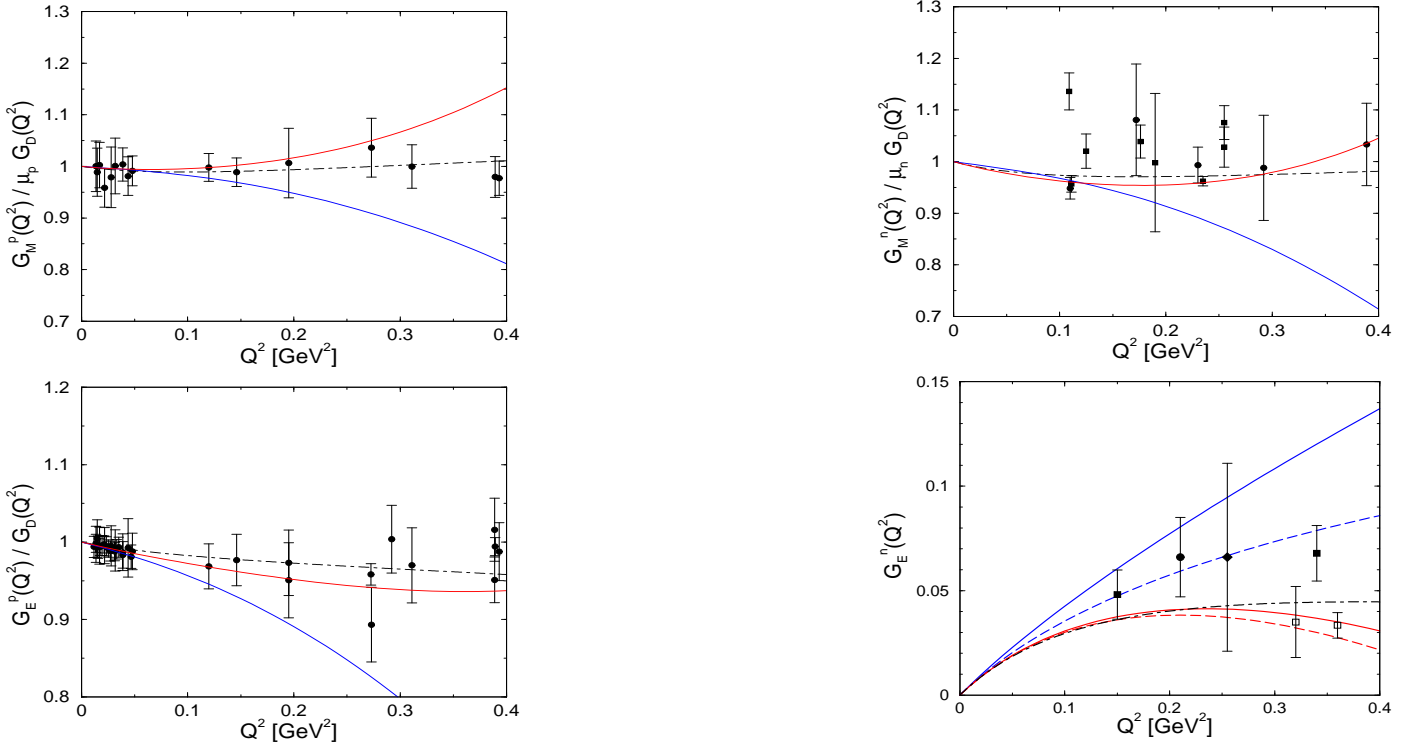


Figure 38: The nucleon e.m. FFs, divided by the dipole FF in the relativistic baryon χ PT of Kubis and Meissner [Kub01]. The results including vector mesons are shown to third order (blue solid curves) and fourth order (red solid curves). For G_{En} , the results without vector mesons are also shown to third order (blue dashed curve) and fourth order (red dashed curve). For comparison, the dashed-dotted curve is the dispersion fit of [Mer96]. Figures from Ref. [Kub01].

below 350 MeV [Ber00, Far04] have been reached. This continuous effort is important to eliminate one source of systematic error associated with the extrapolation to the light quark masses.

The bare coupling constant and quark masses are tuned as a changes to leave physical quantities unchanged. In a typical lattice calculation one starts by choosing the bare coupling constant g , which fixes the lattice spacing, and the bare masses for the u-, d- and s-quarks. One then computes a physical quantity such as the mass of the pion and the nucleon in lattice units as a function of the quark mass. The pion mass is used to fix the u- and d- quark masses (assumed degenerate) and the mass of the kaon or ϕ to fix the strange quark mass whereas the lattice spacing is determined by extrapolating the results, for instance, for the nucleon mass to the physical pion mass. Any other physical quantity in the light quark sector then follows.

In the following, we will discuss lattice calculations for the (space-like) nucleon e.m. FFs. The calculation of the nucleon e.m. FFs requires the evaluation of three-point functions, which involve two topologically different contributions as illustrated in Fig. 39. In the connected diagram contribution (left panel of Fig. 39), the photon couples to one of the quarks connected to either the initial or final nucleon. The quark lines in Fig. 39 are understood to be dressed with an arbitrary number of gluons exchanged between the quarks. If the fluctuations of such gluons into $q\bar{q}$ pairs are neglected, one speaks of the quenched approximation. The full QCD (unquenched) results include as well these sea-quark loop insertions into the gluon lines. The disconnected diagram (right panel of Fig. 39) involves a coupling to a $q\bar{q}$ loop, which then interacts with the

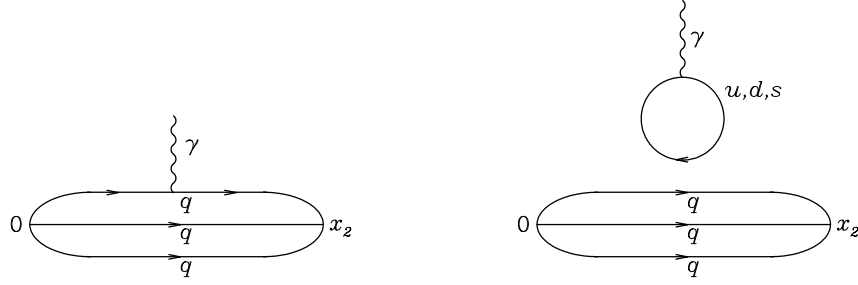


Figure 39: Diagrams illustrating the two topologically different contributions when calculating nucleon e.m. FFs in lattice QCD. Left panel : connected diagram; right panel : disconnected diagram. Figure from Ref. [Boi06].

nucleon through gluon exchange. The disconnected diagram, which requires a numerically more intensive calculation, is at present neglected in most lattice studies. When taking the difference between proton and neutron e.m. FFs, i.e. for the isovector combination of nucleon e.m. FFs, the disconnected contribution drops out. Therefore, all following calculations in which the disconnected diagram is neglected are applicable only to the isovector e.m. FFs. To directly calculate the proton and neutron e.m. FFs, involves the evaluation of the disconnected contribution, which awaits the next generation of dynamical-fermion lattice QCD simulations.

The calculation of the connected diagram contribution to the nucleon e.m. FFs involves the computation of a sequential propagator. Such calculation can be done in two different ways. In an early pioneering work⁵ of Leinweber, Woloshyn and Draper [Lei91], this was done in the so-called fixed current approach, which requires the current to have a fixed direction and to carry a fixed momentum. This method allows one to use different initial or final states without requiring further inversions, which is the time-consuming part of the calculation. For a recent calculation of charge radii and magnetic moments of the whole baryon octet using this method, see Ref. [Boi06]. The drawback of this method is that a new calculation is required for each momentum transfer.

More recently, a second method has been used by different groups to evaluate nucleon e.m. FFs, in which one fixes the initial and final states to have the quantum numbers of the nucleon. In this so-called fixed sink method, the current can couple to a quark line at any intermediate time slice, see Fig. 39 (left panel), carrying any possible value of the lattice momentum, which makes it the method of choice for a detailed study of the momentum transfer dependence of the nucleon e.m. FFs.

The Nicosia-MIT group [Ale06a, Ale06b] has performed a high-statistics calculation of nucleon isovector e.m. FFs in the fixed sink method, both in the quenched approximation and in full QCD, using two dynamical Wilson fermions. The discretization of spacetime which is at the heart of a lattice calculation introduces an ultraviolet cut-off limiting the highest momentum to $2\pi/a$. Both the quenched and unquenched calculations of Ref. [Ale06a] were performed for one value of the lattice spacing a , around 0.09 (0.08) fm for the quenched (unquenched) results. Due to the finite box size of length L , only discrete values of momentum in units of $2\pi/L$ are possible in such a calculation. This imposes a smallest available non-zero momentum transfer, which for the quenched calculation of Ref. [Ale06a] is around $Q^2 \simeq 0.17 \text{ GeV}^2$. The largest Q^2 value accessible is around $Q^2 \simeq 2 \text{ GeV}^2$. Beyond such value, the Fourier transforms needed to evaluate the two- and three-

⁵The first lattice QCD calculations for the pion e.m. FF were performed by Wilcox and Woloshyn [Wil85], whereas the first attempt at a lattice QCD calculation for the proton electric FF was reported by Martinelli and Sachrajda [Mar89].

point functions become noise dominated. Furthermore, the quenched calculation was performed for pion masses in the range $m_\pi \simeq 410 - 560$ MeV. The unquenched calculation was performed in the range of $m_\pi \simeq 380 - 690$ MeV.

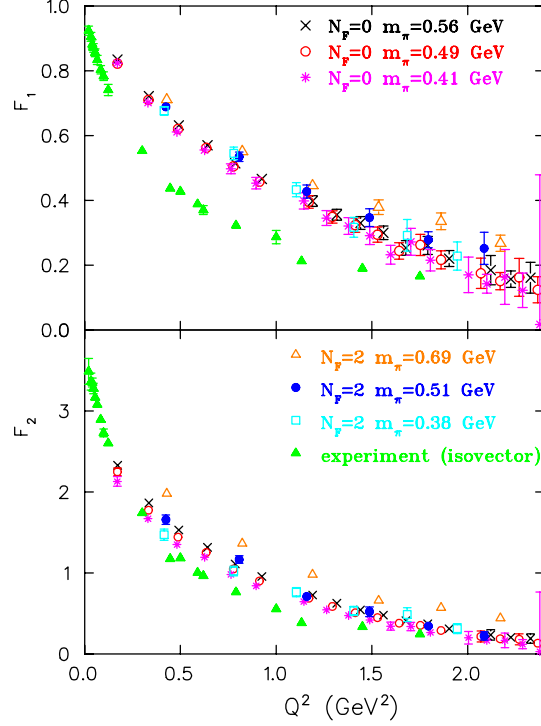


Figure 40: Lattice QCD results (from the Nicosia-MIT group [Ale06a]) for the isovector Dirac FF F_1^V (upper panel) and Pauli FF F_2^V (lower panel) as a function of Q^2 . Both the quenched results (denoted by $N_F = 0$) and unquenched lattice results with two dynamical Wilson fermions (denoted by $N_F = 2$) are shown for three different pion mass values. The filled triangles show the experimental results for the isovector FFs extracted by interpolating the experimental data for the proton and neutron e.m. FFs. Figure from Ref. [Ale06a].

The lattice QCD results of Ref. [Ale06a] for the nucleon Dirac and Pauli isovector FFs are shown in Fig. 40. One observes that both the quenched and unquenched results for the Dirac FF F_1^V show only a very weak quark mass dependence in the range $m_\pi \simeq 400 - 700$ MeV. When comparing with experiment, one sees that both the quenched and unquenched lattice results of Ref. [Ale06a] largely overestimate the data for F_1^V . For F_2^V , one observes a stronger quark mass dependence, bringing the lattice results closer to experiment when decreasing m_π .

The two main uncertainties in this calculation are the continuum extrapolation (i.e. finite a effects) and whether one is close enough to the chiral limit (i.e. extrapolation in quark mass or m_π). To check the latter, and to extrapolate the lattice results down to the physical pion mass value in order to directly compare with experiment, the Nicosia-MIT group uses a linear fit in m_π^2 (corresponding with a linear fit in the quark mass). Such a linear fit, which is supported by the lattice results in the range $m_\pi \simeq 400 - 700$ MeV, is shown in Fig. 41. The thus extrapolated lattice results for F_2^V and G_M^V are in agreement with experiment for Q^2 values larger than about 0.3 GeV^2 . At smaller values of Q^2 , an agreement can also be expected as one can calculate in this range the m_π dependence using χ PT. We will discuss in the following the fact that the corresponding pion loops for the isovector magnetic moment lead to non-analytic behaviors in the quark mass, yielding a

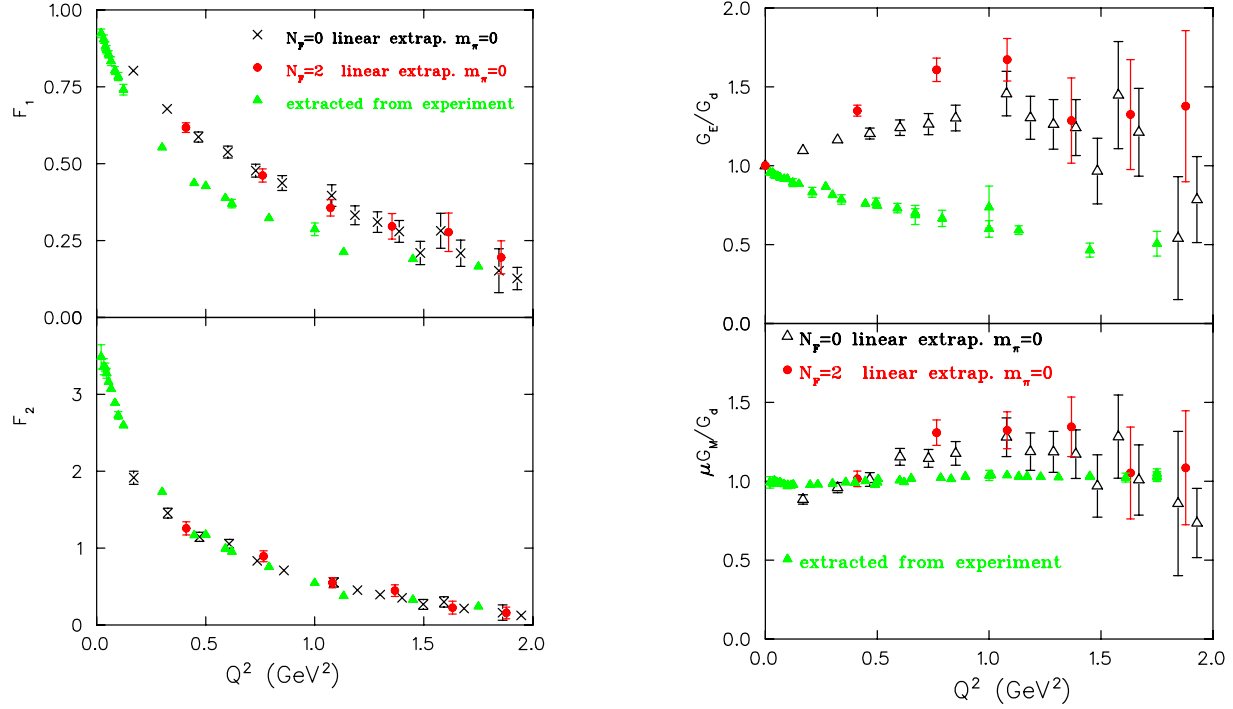


Figure 41: Lattice QCD results (from the Nicosia-MIT group [Ale06a]) for the nucleon isovector FFs F_1^V (upper left panel), F_2^V (lower left panel), G_E^V (upper right panel) and G_M^V (lower right panel) as a function of Q^2 in the chiral limit (using a linear extrapolation in m_π^2). The quenched (unquenched) results are shown by the crosses (filled circles). The experimental values are shown by the filled triangles, and both G_E^V and G_M^V have been divided by the standard dipole FF. Figure from Ref. [Ale06a].

more rapid (than linear in m_π^2) variation as one approaches the chiral limit. On the other hand, the linearly in m_π^2 extrapolated results for F_1^V still show strong disagreement with the data. This translates into an electric FF G_E^V which drops less fast than the dipole FF G_D , whereas the data tell us that G_E^V drops faster than the dipole. It is puzzling that this strong disagreement is seen at larger values of Q^2 , where effects of pion loops are already suppressed, making it unlikely that the chiral extrapolation alone can explain this discrepancy. As both quenched and unquenched calculations of Ref. [Ale06a] were only performed at one value of a , it would be very worthwhile, in order to shed light on this puzzle, to repeat such calculations for different values of the lattice spacing. This would also provide a check of the continuum extrapolation for Wilson fermions, which have discretization errors of order a .

Unquenched lattice calculations using two mass degenerate flavors of dynamical Wilson fermions have also been reported by the QCDSF Coll. [Goc06]. These results improve on previous calculations by the QCDSF Coll. [Goc05] which were performed using Wilson fermions in the quenched approximation. The Q^2 dependence of the lattice results for the nucleon isovector FFs was parameterized (as a first approximation) in terms of a dipole behavior. In particular, for F_1^V this yields :

$$F_1^V(Q^2) = \left(1 + \frac{Q^2}{(M_1^{(v)})^2}\right)^{-2}, \quad (63)$$

where $M_1^{(v)}$ represents the dipole mass. Experimentally, one finds $M_1^{(v)} \simeq 0.843$ GeV. The unquenched

QCDSF lattice results for $M_1^{(v)}$ are shown in Fig. 42 for pion mass values down to 340 MeV. One sees that the unquenched lattice results for $M_1^{(v)}$ become smaller with decreasing pion mass values. When performing a fit linear in m_π^2 to the data, the resulting value of $M_1^{(v)}$ lies however significantly above the experimental value of 0.843 GeV. This yields an isovector FF F_1^V which has a too flat Q^2 dependence, confirming the puzzling finding of Ref. [Ale06a], which was also obtained for two dynamical Wilson fermions.

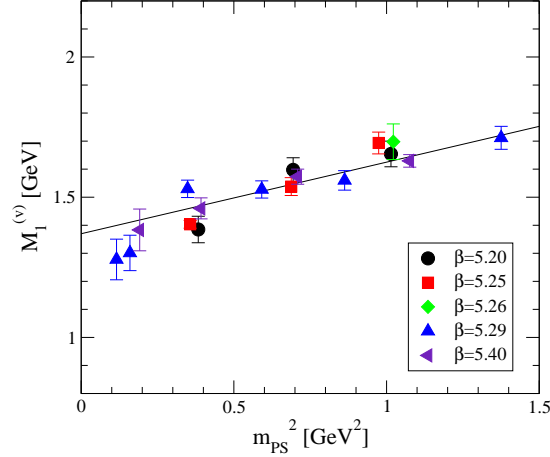


Figure 42: Lattice QCD results (from the QCDSF Coll. [Goc06]) for the isovector Dirac dipole mass $M_1^{(v)}$, see Eq. (63). The unquenched lattice results with two dynamical Wilson fermions are displayed as function of m_π^2 . Figure from Ref. [Goc06].

Recently, unquenched lattice QCD calculations for the nucleon e.m. FFs have also been performed by the LHPC Coll. [Edw06] based on the Asqtad improved action, using different fermions for valence and sea quarks. This hybrid action uses for the valence quarks domain wall fermions. For the sea quarks, the configurations generated by the MILC Coll. [Ber00] are used, with two degenerate light and one strange staggered quarks, allowing for economical calculations. The discretization errors in this action are of order a^2 , in comparison with order a for the above discussed Wilson action. The other advantage of this hybrid action is that domain wall fermions preserve chiral symmetry on the lattice. Although this action has generated quite a number of encouraging results when applied to nucleon structure studies, such as e.g. moments of unpolarized, helicity, and transversity distributions, see Ref. [Edw06] for a recent overview, some controversy remains around the fourth root of the fermion determinant [Sha06].

In Fig. 43, we show the unquenched lattice QCD results for the nucleon e.m. FFs obtained with this hybrid action by the LHPC Coll., performed for one lattice spacing of $a \simeq 0.125$ fm, and for pion mass values in the range $m_\pi = 360 - 775$ MeV. It is seen that in contrast to the above discussed Wilson results, this action yields a noticeable dependence on m_π for the Dirac isovector FF F_1^V at larger values of Q^2 . The Q^2 dependence of F_1^V at the smallest m_π value of around 360 MeV is found to be in qualitative agreement with the data. One also sees from Fig. 43 that the isovector ratio F_2^V/F_1^V approaches the experimental result when decreasing m_π . So far this is the only lattice calculation which yields a qualitative consistent picture for both F_1^V and F_2^V . Evidently, it will be very worthwhile to corroborate the results at the lowest pion masses and improve their statistics in future calculations. If confirmed by higher statistics results, it remains to be understood why different actions may yield significantly different results, in particular for F_1^V . Unquenched calculations at a

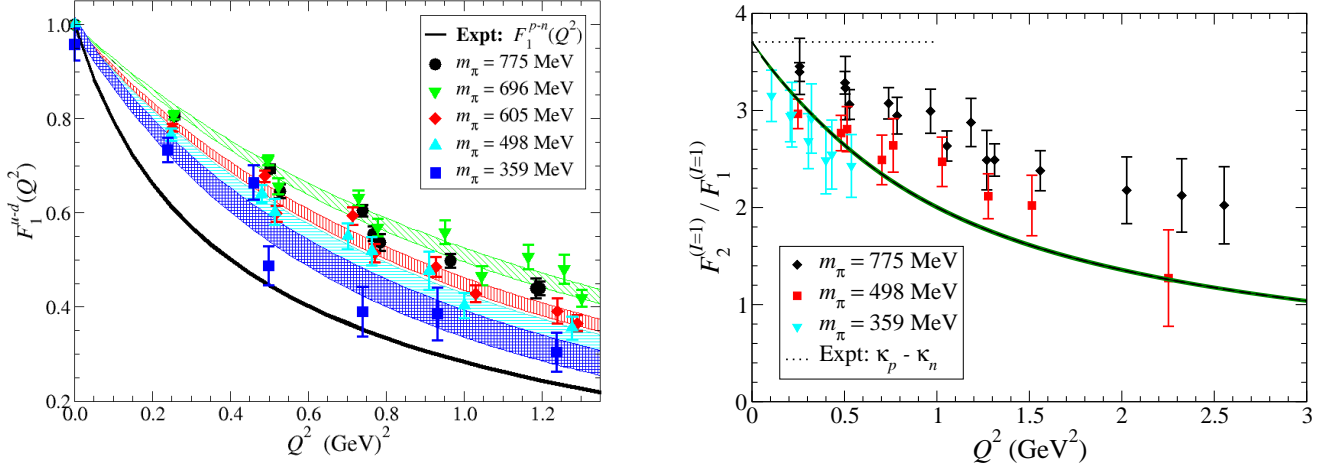


Figure 43: Lattice QCD results (from the LHPC Coll. [Edw06]) for the nucleon isovector form factors F_1^V (left panel) and for the ratio F_2^V/F_1^V (right panel). The unquenched results using a hybrid action of domain wall valence quarks and 2+1 flavor staggered sea quarks are shown for different values of m_π and are compared with experiment (solid curve, using the parametrization of Ref. [Kel04]). Figure from Ref. [Edw06].

couple of different lattice spacings using both the Wilson and the above described hybrid action would be very helpful in this respect.

4.5.2 Chiral extrapolations

Present lattice calculations are possible for larger than physical quark masses, and therefore necessitate an extrapolation procedure in order to make contact with experiment. The extrapolation in the quark mass m_q is not straightforward, because the non-analytic dependencies, such as $\sqrt{m_q}$ and $\ln m_q$, become important as one approaches the small physical value of m_q . Therefore naive extrapolations often fail, while spectacular non-analytic effects are found in a number of different quantities, such as nucleon magnetic moments and charge radii, see *e.g.* Refs. [Lei01, Hem02]. The χ EFT, discussed in the Sect. 4.4, provides a framework to compute these non-analytic dependencies, for small quark masses.

As an example, in the SSE (ε -expansion) to order ε^3 , the $\gamma^* NN$ vertex is calculated [Goc05] through the one-loop diagrams in Fig. 44. Due to the pion loops, the isovector Dirac radius $\langle r^2 \rangle_1^V$ acquires non-analytic dependencies in the quark mass. Its leading dependence in the pion mass is given by [Lei93] :

$$\langle r^2 \rangle_1^V \equiv \langle r^2 \rangle_{1p} - \langle r^2 \rangle_{1n} = a_0(\mu) - \frac{1 + 5g_A^2}{(4\pi f_\pi)^2} \log \left(\frac{m_\pi^2}{\mu^2} \right) + \mathcal{O}(m_\pi^2) + \pi \Delta \text{ loops}, \quad (64)$$

where the logarithmic term in m_π is the leading non-analytic (LNA) dependence originating from the πN loop diagrams (Fig. 44 (a - f)). This LNA contribution only depends on the nucleon axial coupling $g_A = 1.2695$ and the pion decay constant $f_\pi = 92.4$ MeV. Furthermore in Eq. (64), μ is the renormalization scale, and $a_0(\mu)$ is a LEC (evaluated at scale μ). Note that, in contrast to most chiral extrapolations which contain finite terms of the form $m_\pi^2 \log m_\pi^2$, the isovector radius diverges like $\log m_\pi^2$, rendering the variation of the radius quite substantial near the physical pion mass.

Analogously, the πN loop diagrams give rise to non-analytic terms in the quark-mass expansion of the

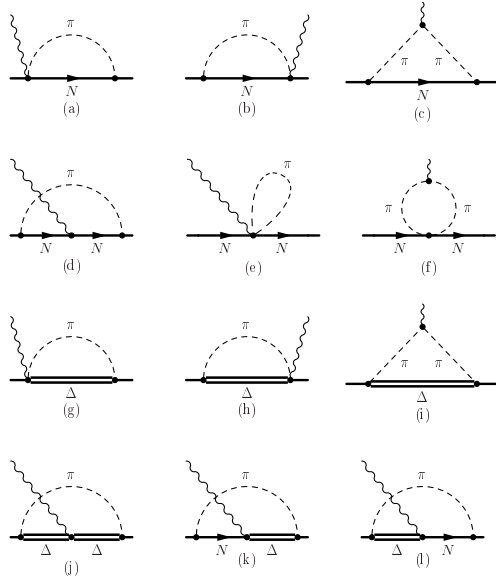


Figure 44: One-loop diagrams to the $\gamma^* NN$ vertex as calculated in χ PT in the SSE to order ε^3 in Ref. [Goc05]. Diagrams (a - f) correspond with an intermediate nucleon; diagrams (g - l) involve an intermediate $\Delta(1232)$.

nucleon isovector magnetic moment. Its leading dependence in the pion mass is given by :

$$\kappa^V \equiv \kappa_p - \kappa_n = \kappa_0^V - \frac{4g_A^2 M}{(4\pi f_\pi)^2} m_\pi + \mathcal{O}(m_\pi^2) + \pi\Delta \text{ loops}, \quad (65)$$

where the LEC κ_0^V corresponds with the isovector anomalous magnetic moment in the chiral limit.

The LNA behavior of the isovector Pauli radius $\langle r^2 \rangle_2^V$ due to πN loops shows a $1/m_\pi$ divergence in the chiral limit [Goc05] :

$$\langle r^2 \rangle_2^V \equiv \langle r^2 \rangle_{2p} - \langle r^2 \rangle_{2n}|_{LNA} = \frac{1}{\kappa^V} \frac{g_A^2 M}{8\pi f_\pi^2 m_\pi}. \quad (66)$$

In Fig. 45, the lattice results for the pion mass dependence of the isovector magnetic moment, and the isovector Dirac and Pauli squared radii are compared with the χ PT results of Ref. [Goc06] in the SSE to order ε^3 , which involves the diagrams shown in Fig. 44. Note that the χ PT fit of Ref. [Goc05] for κ^V e.g. implies fixing four LECs, which were fitted to the lattice data at relatively large m_π values. The lattice calculations shown in Fig. 45 are the quenched and unquenched results from the Nicosia-MIT group[Ale06a] and the unquenched results from the QCDSF Coll.[Goc06], both using the Wilson action. One sees that for both the isovector anomalous magnetic moment and the isovector Pauli radius, the lattice data at the smallest available values of m_π indeed seem to follow the strong rise predicted by the χ PT fit. The resulting χ PT fit is able to account for the observed m_π dependence in κ^V and $\langle r^2 \rangle_2^V$. Therefore, the too small value for the Pauli FF F_2^V at small Q^2 values, when extrapolating the lattice results linearly in m_π^2 , as shown in Fig. 41, can be reconciled with the empirical FF value by accounting for the non-analytic quark mass dependences.

On the other hand, the lattice results of Refs. [Ale06a] and [Goc06] for the isovector Dirac radius, shown in Fig. 45, show no strong indication of the logarithmic $\ln m_\pi$ divergence. This is also reflected in the comparison with the SSE results, which is not able to account for the lattice results.

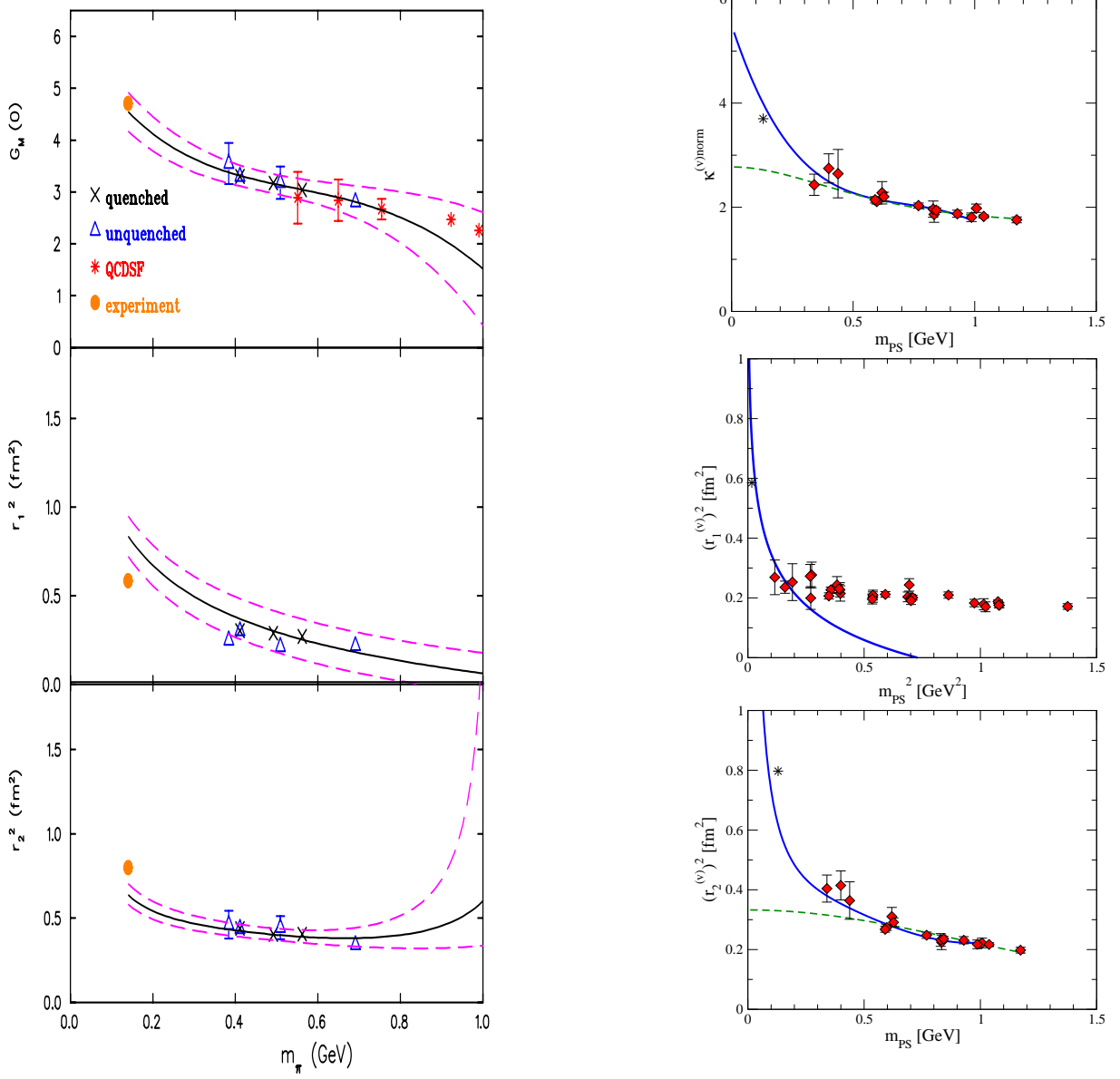


Figure 45: Chiral extrapolation of the isovector magnetic moment (upper panels) and the isovector squared radii for the Dirac, $\langle r^2 \rangle_1^V$ (middle panels), and Pauli, $\langle r^2 \rangle_2^V$ (lower panels), FFs. The left panels are the quenched (crosses) and unquenched (triangles) results from the Nicosia-MIT group [Ale06a]. The right panels show the corresponding unquenched results from the QCDSF Coll. [Goc06]. In both the left and right panels, the solid curves are the best fit to the χ EFT results of Ref. [Goc05] in the SSE to order ε^3 . In the left panel, the dashed curves are an estimate of the error band of the fit. In the right panel, the dashed curves are a fit which does not include the non-analytic contributions.

One may of course wonder if any agreement or disagreement with χ PT for m_π values as large as 0.5 - 1 GeV is very meaningful. Surely at such large m_π values, higher order contributions not accounted for in e.g. the ε^3 calculations shown in Fig. 45 are important⁶. A conservative strategy is to restrict χ PT to its limited range of applicability and await lattice results for m_π value below 300 MeV where the effect of higher order terms is still relatively small. Alternatively, one may choose to build upon χ EFT and extend its range of applicability - leaving the domain of strict power counting - by resumming higher order effects using additional physics principles.

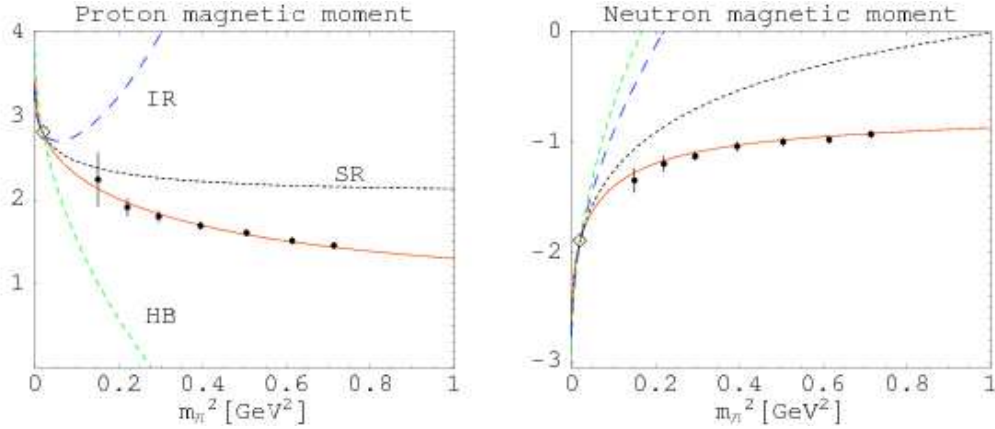


Figure 46: Chiral behavior of proton and neutron magnetic moments (in nucleon magnetons) to one loop compared with lattice data. “SR” (dotted curves): one-loop relativistic result [Pas04, Hol05], “IR” (blue long-dashed curves): infrared-regularized relativistic result [Kub01], “HB” (green dashed curves): LNA term in the heavy-baryon expansion. Red solid curves: two-parameter fit of Refs. [Pas04, Hol05] based on a sum rule (SR) evaluation. The data points are the lattice calculations of Ref. [Boi06]. The open diamonds represent the experimental values at the physical pion mass.

One such strategy has been adopted in Refs. [Pas04, Hol05] by using analyticity to resum higher order (analytic) terms in m_π^2 to the nucleon magnetic moments. By requiring the anomalous magnetic moments to satisfy (a generalization of) the Gerasimov-Drell-Hearn sum rule [Ger66, Dre66], a relativistic one-loop πN calculation has the correct chiral behavior at the small values of m_π , and yields a convergent $1/m_\pi^2$ behavior at larger values of m_π . It motivates a two-parameter fit for the m_π dependence of the magnetic moment as :

$$\mu = \frac{\mu_0}{1 + am_\pi^2} + \delta\kappa_{loop}, \quad (67)$$

where $\delta\kappa_{loop}$ is the calculated πN loop correction based on the sum rule (SR) evaluation, μ_0 is the LEC adjusted to the magnetic moment in the chiral limit ($m_\pi = 0$), and a is a parameter which is adjusted to include the effects beyond πN loops to the magnetic moment at large m_π values. The resulting two-parameter fit of the lattice results yields a much smoother m_π behavior than a truncated χ PT calculation as shown in Fig. 46. Such an extension of χ EFT may yield a convenient parametrization of lattice results for m_π values beyond 500 MeV, while encompassing the correct behavior for small m_π values.

⁶See e.g. Ref. [McG06], where it was shown that the surprisingly good agreement of fourth-order χ PT when extrapolating lattice data for the nucleon mass out to large pion mass values (in the range 0.5 - 1 GeV) is spoiled once the fifth-order terms (due to 2-loop πN diagrams) are included.

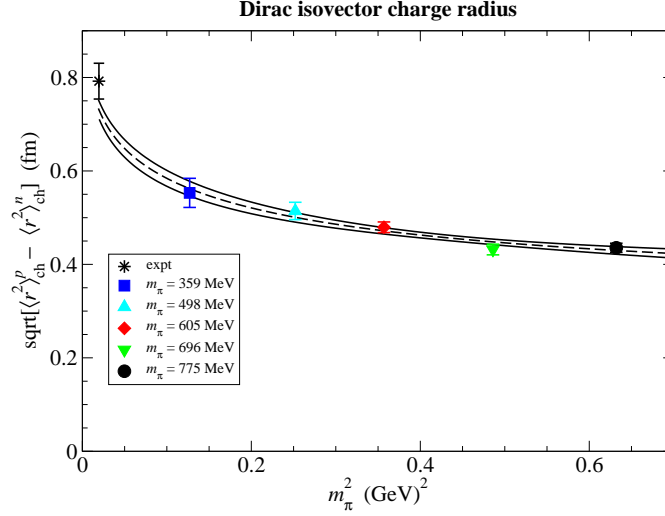


Figure 47: Chiral extrapolation of the nucleon isovector Dirac radius $\langle r^2 \rangle_1^V$. The unquenched results are from the LHPC Coll. [Edw06]. The experimental value is shown by the star. The curves are fits using the chiral extrapolation formula Eq. (68) of Ref. [Dun02]. Figure from Ref. [Edw06].

Another strategy has been pursued by the Adelaide group by modifying the one-loop χ PT results and taking into account the finite size of the nucleon through a finite range regularization procedure. This method was found successful when applying it to the calculation of the m_π dependence of nucleon and $\Delta(1232)$ masses, see e.g. Refs. [Lei00, Lei04]. For the isovector Dirac radius, one may try in this spirit a modification of the χ PT formula of Eq. (64) as [Dun02] :

$$\langle r^2 \rangle_1^V = a_0 - \frac{1 + 5g_A^2}{(4\pi f_\pi)^2} \log \left(\frac{m_\pi^2}{m_\pi^2 + \Lambda^2} \right), \quad (68)$$

where Λ is a phenomenological cut-off which reflects the finite size of the nucleon. Such a fit for the isovector Dirac radius is shown in Fig. 47 and compared with the most recent unquenched lattice results using the hybrid action (domain wall valence quarks on top of a 2+1 flavor staggered sea) of the LHPC Coll. One firstly sees, that these lattice results do shown appreciable m_π^2 variation over the pion mass range $m_\pi = 360 - 775$ MeV and provide a first clear hint of the logarithmic m_π divergence. As the pion mass approaches the physical value, the calculated nucleon size increases and approaches the correct value. Using the simple extrapolation formula of Eq. (68), which has the $\log m_\pi$ divergence at low m_π values built in, one obtains a consistent description of the m_π dependence of the lattice results using $\Lambda \sim 500$ MeV.

Finally we would like to emphasize that presently there is no systematic framework for extrapolating lattice QCD results for FFs at values of Q^2 larger than about 0.3 GeV^2 , i.e. beyond the region where a χ PT expansion is expected to be applicable. The development of such a framework remains a challenge for future work. Even when lattice results become available for m_π values below 300 MeV, at larger Q^2 , one is confronted with the problem of performing a chiral extrapolation (in the small scale m_π) in the presence of a large scale Q^2 . A first attempt in this direction has been performed in Ref. [Mat05], within the context of a light-front cloudy bag model.

4.6 Generalized parton distributions (GPDs)

4.6.1 Definition of GPDs and form factor sum rules

So far we have discussed the $N \rightarrow N$ transition as revealed with the help of the electromagnetic probe. By measuring the response of the hadron to a virtual photon, one measures the matrix element of a well-defined quark-gluon operator (in this case the vector operator $\bar{q}\gamma^\mu q$) over the hadronic state. This matrix element can be parametrized in terms of the nucleon e.m. FFs, revealing the quark-gluon structure of the nucleon. We are however not limited in nature to probes such as photons (or W , Z bosons for the axial transition). The phenomenon of asymptotic freedom of QCD, meaning that at short distances the interactions between quarks and gluons become weak, provides us with more sophisticated QCD operators to explore the structure of hadrons. Such operators can be accessed by selecting a small size configuration of quarks and gluons, provided by a hard reaction, such as deep inelastic scattering (DIS), or hard exclusive reactions such as deeply virtual Compton scattering (DVCS). We will be mostly interested here in DVCS reactions which are of the type $\gamma^*(q_h) + N(p) \rightarrow \gamma(q') + N(p')$, where the virtual photon momentum q_h is the hard scale. The common important feature of such hard reactions is the possibility to separate clearly the perturbative and nonperturbative stages of the interactions, this is the so-called factorization property.

The all-order factorization theorem for the DVCS process on the nucleon has been proven in Refs. [Ji98a, Col99, Rad98]. Qualitatively one can say that the hard reactions allow one to perform a “microsurgery” of a nucleon by removing in a controlled way a quark of one flavor and spin and implanting instead another quark (in general with a different flavor and spin) in the final nucleon. It is illustrated in Fig. 48 for the case of the DVCS process. The non-perturbative stage of such hard exclusive electroproduction processes is described by universal objects, so-called generalized parton distributions (GPDs) [Mul94, Ji97, Rad96], see Refs. [Ji98b, Goe01, Die03, Bel05, Ji04] for reviews and references.

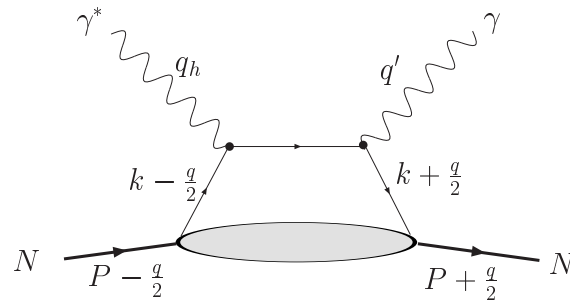


Figure 48: The “handbag” diagram for the nucleon DVCS process. Provided the virtuality of the initial photon (with momentum q_h) is sufficiently large, the QCD factorization theorem allows to express the total amplitude as the convolution of a Compton process at the quark level and a non-perturbative amplitude parametrized in terms of generalized parton distributions (lower blob). The diagram with the photon lines crossed is also understood.

The nucleon structure information entering the nucleon DVCS process, can be parametrized at leading twist-2 level, in terms of four (quark chirality conserving) GPDs⁷. The GPDs depend on three variables: the quark longitudinal momentum fractions x and ξ , and the momentum transfer $Q^2 = -q^2$ to the nucleon. The light-cone momentum fraction x is defined by $k^+ = xP^+$, where k is the quark loop momentum and P is the average nucleon momentum $P = (p + p')/2$, where $p(p')$ are the initial (final) nucleon four-momenta respec-

⁷ We do not consider chirally odd GPDs, which are also discussed in the literature, see e.g. the review of Ref. [Die03]

tively, see Fig. 48. The skewedness variable ξ is defined by $q^+ = -2\xi P^+$, where $q = p' - p$ is the overall momentum transfer in the process, and where $2\xi \rightarrow x_B/(1 - x_B/2)$ in the Bjorken limit: $x_B = Q_h^2/(2p \cdot q_h)$ is the usual Bjorken scaling variable, with $Q_h^2 = -q_h^2 > 0$ the virtuality of the hard photon. Furthermore, the third variable entering the GPDs is given by the invariant $Q^2 = -q^2$, being the total squared momentum transfer to the nucleon.

The DVCS process corresponds with the kinematics $Q_h^2 \gg Q^2, M^2$, so that at twist-2 level, terms proportional to Q^2/Q_h^2 or M^2/Q_h^2 are neglected in the amplitude. In a frame where the virtual photon momentum q_h^μ and the average nucleon momentum P^μ are collinear along the z -axis and in opposite directions, one can parametrize the non-perturbative object entering the nucleon DVCS process as (following Ji [Ji97])⁸:

$$\begin{aligned} & \frac{1}{2\pi} \int dy^- e^{ixP^+ y^-} \langle N(p') | \bar{\psi}(-y/2) \gamma \cdot n \psi(y/2) | N(p) \rangle \big|_{y^+ = \vec{y}_\perp = 0} \\ &= H^q(x, \xi, Q^2) \bar{u}(p') \gamma \cdot n u(p) + E^q(x, \xi, Q^2) \bar{u}(p') i\sigma^{\mu\nu} \frac{n_\mu q_\nu}{2M} u(p), \end{aligned} \quad (69)$$

where ψ is the quark field of flavor q , u the nucleon spinor, and n^μ is a light-cone vector along the negative z -direction which can be expressed at twist-2 level in terms of the external momenta as:

$$q_h = -2\xi P + \frac{Q_h^2}{4\xi} n, \quad q = -2\xi P + q_\perp, \quad q' = \frac{Q_h^2}{4\xi} n - q_\perp, \quad (70)$$

where $q_\perp = (0, \mathbf{q}_\perp, 0)$ is the transverse component of the momentum transfer q , satisfying $q_\perp \cdot n = q_\perp \cdot P = 0$. Furthermore the light-cone vector n , satisfying $n^2 = 0$ is normalized in such a way that $n \cdot P = 1$. The *lhs* of Eq. (69) can be interpreted as a Fourier integral along the light-cone distance y^- of a quark-quark correlation function, representing the process where a quark is taken out of the initial nucleon (having momentum p) at the space-time point $y/2$, and is put back in the final nucleon (having momentum p') at the space-time point $-y/2$. This process takes place at equal light-cone time ($y^+ = 0$) and at zero transverse separation ($\vec{y}_\perp = 0$) between the quarks. The resulting one-dimensional Fourier integral along the light-cone distance y^- is with respect to the quark light-cone momentum xP^+ . The *rhs* of Eq. (69) parametrizes this non-perturbative object in terms of the GPDs H^q and E^q for a quark of flavor q . The quark vector operator ($\gamma \cdot n$) corresponds at the nucleon side to a vector transition (parametrized by the function H^q) and a tensor transition (parametrized by the function E^q). Analogously, there are two GPDs corresponding with a quark axial vector operator ($\gamma \cdot n \gamma_5$), which are commonly denoted by the polarized GPDs \tilde{H}^q and \tilde{E}^q .

The variable x in the GPDs runs from -1 to 1 . Therefore, the momentum fractions of the active quarks ($x + \xi$) for the initial quark and ($x - \xi$) for the final quark can either be positive or negative. Since positive (negative) momentum fractions correspond to quarks (antiquarks), it has been noted in [Rad96] that in this way, one can identify two regions for the GPDs: when $x > \xi$ both partons represent quarks, whereas for $x < -\xi$ both partons represent antiquarks. In these regions, the GPDs are the generalizations of the usual parton distributions from DIS. Actually, in the forward direction, the GPD H reduces to the quark (anti-quark) density distribution $q(x)$ ($\bar{q}(x)$) obtained from DIS:

$$H^q(x, 0, 0) = \begin{cases} q(x), & x > 0, \\ -\bar{q}(-x), & x < 0. \end{cases} \quad (71)$$

The function E (and likewise the function \tilde{E} for the axial operator) are not measurable through DIS because the associated tensor in Eq. (69) vanishes in the forward limit ($q \rightarrow 0$). Therefore, E is a new leading twist

⁸In all non-local expressions we always assume the gauge link: $P \exp(i g \int dx^\mu A_\mu)$, ensuring the color gauge invariance.

function, which is accessible by measuring hard exclusive electroproduction reactions, such as DVCS.

As the momentum fractions of initial and final quarks are different, one accesses quark momentum correlations in the nucleon. Furthermore, in the region $-\xi < x < \xi$, one parton connected to the lower blob in Fig. 48 represents a quark and the other one an antiquark. In this region, the GPDs behave like a meson distribution amplitude and contain completely new information about nucleon structure, because the region $-\xi < x < \xi$ is absent in DIS, which corresponds to the limit $\xi \rightarrow 0$.

Besides coinciding with the quark distributions at vanishing momentum transfer, the GPDs have interesting links with other nucleon structure quantities. The first moments of the GPDs are related to the elastic form factors of the nucleon through model independent sum rules. By integrating Eq. (69) over x , one obtains for any ξ the following relations for a particular quark flavor [Ji97] :

$$\int_{-1}^{+1} dx H^q(x, \xi, Q^2) = F_1^q(Q^2), \quad \int_{-1}^{+1} dx E^q(x, \xi, Q^2) = F_2^q(Q^2), \quad (72)$$

where $F_1^q(Q^2)$ represents the elastic Dirac FF for the quark flavor q in the nucleon. These quark FFs are expressed, using $SU(2)$ isospin, as flavor combinations of the proton and neutron elastic FFs as:

$$F_1^u = 2 F_{1p} + F_{1n} + F_1^s, \quad F_1^d = 2 F_{1n} + F_{1p} + F_1^s, \quad (73)$$

where F_{1p} (F_{1n}) are the proton (neutron) Dirac FFs respectively. In Eq. (73) F_1^s is the strangeness FF of the nucleon (which is neglected in the calculations discussed below). Relations similar to Eq. (73) hold for the Pauli FFs F_2^q . At $Q^2 = 0$, the normalizations of the Dirac FFs for the quark flavors are given by: $F_1^u(0) = 2$ ($F_1^d(0) = 1$) so as to yield the normalization of 2 (1) for the u (d)-quark distributions in the proton. The normalizations of the Pauli FF at $Q^2 = 0$ are given by $F_2^q(0) = \kappa^q$ (for $q = u, d$), where κ^u, κ^d can be expressed in terms of the proton (κ_p) and neutron (κ_n) anomalous magnetic moments as:

$$\kappa^u \equiv 2\kappa_p + \kappa_n = +1.673, \quad \kappa^d \equiv \kappa_p + 2\kappa_n = -2.033. \quad (74)$$

The sum rules of Eq. (72) also satisfy the condition that they are independent of ξ , which is a consequence of Lorentz invariance⁹.

The above sum rules allow us to make a prediction for the nucleon e.m. FFs provided we have a model for the nucleon GPDs. Note that the sum rules of Eq. (72) only involve valence quark GPDs, since the sea-quark and anti-quark contributions (the latter correspond with negative x -values) cancel each other in the sum rules. A model for the valence quark GPDs will be discussed in the following section. Conversely, the existing precise experimental information on the nucleon e.m. FFs provides a strong constraint on the nucleon GPDs. As discussed above, the GPDs are however much richer observables and provide us with quark distribution information in the nucleon. First experiments accessing the nucleon GPDs have been reported in recent years by the HERMES Coll. [Air01, Air06], at HERA [Adl01, Che03, Akt05], and at JLab [Ste01, Che06, Mun06]. Furthermore, accessing the nucleon GPDs is a major project for the planned JLab 12 GeV upgrade.

4.6.2 Models for the GPDs H and E

In this section, we discuss current parameterizations for the GPDs H and E , and evaluate the sum rules of Eq. (72) to obtain the Dirac and Pauli nucleon FFs. Since the results of the integration in Eq. (72) do not

⁹This is the simplest example of a so-called polynomiality condition when calculating moments of GPDs.

depend on the skewness ξ , one can choose $\xi = 0$ in these sum rules. We therefore only discuss the GPDs H and E at $\xi = 0$ in the following.

An initial model for the Q^2 dependence of the GPD H was to take a Gaussian ansatz [Rad98, Die99]. In Ref. [Sto01], the Gaussian ansatz has been modified at large Q^2 by terms having a power-law dependence. Such a Gaussian ansatz, however, is not able to describe the small Q^2 behavior of GPDs, and, in particular, gives divergent rms radii for the nucleon e.m. FFs. Ref. [Goe01] used a parameterization which is motivated from the expected Regge behavior of the GPDs at small x and Q^2 . This yields the ansatz (denoted by Regge parameterization R1) for the valence part of the GPD H^q :

$$H_{R1}^q(x, 0, Q^2) = q_v(x) x^{\alpha' Q^2}, \quad (75)$$

where $q_v(x)$ is the forward valence quark distribution and α' is the slope of the corresponding Regge trajectory. This slope can be directly related to the Dirac mean squared radii for proton and neutron as :

$$\langle r^2 \rangle_{1p} = -6 \alpha' \int_0^1 dx \left\{ e_u u_v(x) + e_d d_v(x) \right\} \ln x, \quad (76)$$

$$\langle r^2 \rangle_{1n} = -6 \alpha' \int_0^1 dx \left\{ e_u d_v(x) + e_d u_v(x) \right\} \ln x, \quad (77)$$

which involves logarithmic moments of the valence u -quark (u_v) and d -quark (d_v) distributions, weighted by the corresponding u - and d -quark charges : $e_u = +2/3$ and $e_d = -1/3$. Using these expressions for the Dirac radii, the Regge slope parameter α' can then be directly fitted from the knowledge of the electromagnetic radii of proton and neutron. In particular, the electric mean squared radii of proton and neutron are given by

$$\langle r^2 \rangle_{Ep} = \langle r^2 \rangle_{1p} + \frac{3}{2} \frac{\kappa_p}{M^2}, \quad \text{and} \quad \langle r^2 \rangle_{En} = \langle r^2 \rangle_{1n} + \frac{3}{2} \frac{\kappa_n}{M^2}, \quad (78)$$

where the first term on the *rhs* is the Dirac radius squared $\langle r^2 \rangle_1$, whereas the second term is the Foldy term.

In the following estimates, the unpolarized valence quark distributions are taken at input scale $\mu^2 = 1 \text{ GeV}^2$ from the MRST2002 global NNLO fit [Mar02] as:

$$\begin{aligned} u_v &= 0.262 x^{-0.69} (1-x)^{3.50} (1 + 3.83 x^{0.5} + 37.65 x), \\ d_v &= 0.061 x^{-0.65} (1-x)^{4.03} (1 + 49.05 x^{0.5} + 8.65 x). \end{aligned} \quad (79)$$

Using these empirical valence quark distributions, the proton and neutron rms radii are shown in Fig. 49 as the functions of the Regge slope α' using the Regge parameterization of Eqs. (76,77). One notes that the neutron charge radius is dominated by the Foldy term, which gives $\langle r^2 \rangle_{En} = -0.126 \text{ fm}^2$. Therefore, a relatively wide range of values α' are compatible with the neutron data. However for the proton, a rather narrow range of values around $\alpha' = 1.0 - 1.1 \text{ GeV}^{-2}$ is favored. Such value is close to the expectation from the near universal Regge slopes for meson trajectories, therefore supporting the Regge type parameterization.

Analogously to the GPD H^q , the function $E^q(x, 0, Q^2)$ can also be parameterized at low Q^2 through a Regge-type form (R1 model) as [Gui05] :

$$E_{R1}^q(x, 0, Q^2) = e^q(x) x^{\alpha' Q^2}. \quad (80)$$

The forward magnetic densities $e^q(x)$ - unlike the usual forward parton densities $q(x)$ - are unfortunately not known from experiment at present. The simplest idea is to take them proportional to the valence up-quark

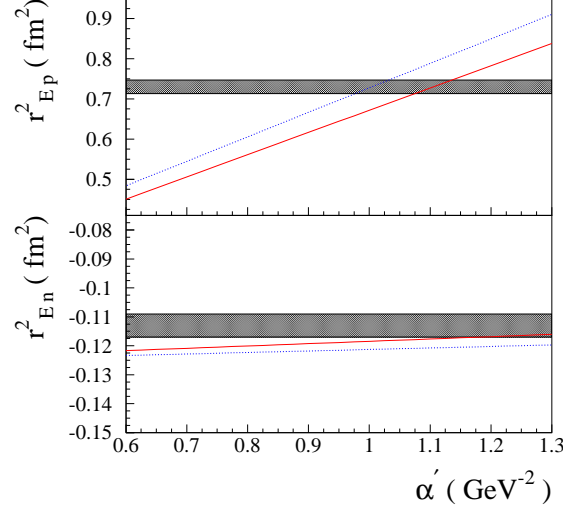


Figure 49: Proton and neutron mean squared charge radii $\langle r^2 \rangle_{Ep}$ (upper panel) and $\langle r^2 \rangle_{En}$ (lower panel), Eq. (78). Dotted curves: Regge ansatz R1, Eqs. (76,77); solid curves : modified Regge ansatz R2, Eqs. (84,85). Both calculations are shown as function of the Regge slope α' . For the quark distributions, the MRST02 NNLO parameterization [Mar02], Eq. (79), was used. The shaded bands correspond to the experimental values. Figure from Ref. [Gui05].

($u_v(x)$) and down-quark ($d_v(x)$) densities as:

$$e^u(x) = \frac{\kappa^u}{2} u_v(x) \quad \text{and} \quad e^d(x) = \kappa^d d_v(x), \quad (81)$$

which satisfy the normalization constraint of Eq. (72) at $Q^2 = 0$:

$$\kappa^q = \int dx e^q(x). \quad (82)$$

where κ^u and κ^d are defined in Eq. (74). One thus sees that the functions $e^q(x)$ encode the quark distribution information giving rise to the nucleon anomalous magnetic moments.

As shown in Figs. 50, 51, the Regge model R1 fits the nucleon Dirac and Pauli FF data for small momentum transfers $Q^2 \lesssim 0.5 \text{ GeV}^2$. However, at larger Q^2 the R1 model gives too strong suppression, and it consequently falls considerably short of the data for $Q^2 > 1 \text{ GeV}^2$.

In Refs. [Die05, Gui05], the above Regge parameterization was extended to larger values of Q^2 . To preserve the Regge behavior at small x and Q^2 , and to modify the large Q^2 behavior, the simplest idea is to adopt a modified Regge ansatz (denoted by the Regge parameterization R2) [Bur03, Bur04] :

$$H_{R2}^q(x, 0, Q^2) = q_v(x) x^{\alpha' (1-x) Q^2}. \quad (83)$$

At small Q^2 , the modifications compared to the R1 model are not very significant numerically. The Dirac

mean squared radii of proton and neutron in the R2 model are finite and given by :

$$\langle r^2 \rangle_{1p} = -6 \alpha' \int_0^1 dx \left\{ e_u u_v(x) + e_d d_v(x) \right\} (1-x) \ln x , \quad (84)$$

$$\langle r^2 \rangle_{1n} = -6 \alpha' \int_0^1 dx \left\{ e_u d_v(x) + e_d u_v(x) \right\} (1-x) \ln x . \quad (85)$$

In the case of the Pauli FF F_2 , one performs the same modification of the ansatz for the GPD E^q :

$$E_{R2}^q(x, 0, Q^2) = e^q(x) x^{\alpha' (1-x) Q^2} . \quad (86)$$

In order to get a more realistic parameterization for the GPD E^q at larger Q^2 , one may notice that experimentally, the proton helicity flip FF $F_2(Q^2)$ has a faster power fall-off at large Q^2 than $F_1(Q^2)$. This means that the $x \sim 1$ behavior of the functions $e^q(x)$ and $q(x)$ should be different. To produce a faster decrease with Q^2 , the $x \sim 1$ limit of the density $e^q(x)$ should have extra powers of $1-x$ compared to that of $q(x)$. Aiming to avoid introducing too many free parameters, Guidal *et al.* [Gui05] tried the next simplest ansatz for $e^q(x)$ by just multiplying the valence quark distributions by an additional factor $(1-x)^{\eta^q}$, i.e. by taking:

$$e^u(x) = \frac{\kappa^u}{N^u} (1-x)^{\eta^u} u_v(x) \quad \text{and} \quad e^d(x) = \frac{\kappa^d}{N^d} (1-x)^{\eta^d} d_v(x) , \quad (87)$$

where the normalization factors N^u and N^d

$$N^u = \int_0^1 dx (1-x)^{\eta^u} u_v(x) , \quad N^d = \int_0^1 dx (1-x)^{\eta^d} d_v(x) , \quad (88)$$

guarantee the condition of Eq. (82). This yields the modified Regge parametrization (R2 model) for the GPD E^q as [Gui05]:

$$E_{R2}^q(x, 0, Q^2) = \frac{\kappa^q}{N^q} (1-x)^{\eta^q} q_v(x) x^{\alpha' (1-x) Q^2} . \quad (89)$$

The resulting Regge ansatz R2 has 3 free parameters which are to be determined from a fit to the FF data. Diehl *et al.* [Die05] chose a more general functional form for $e^q(x)$ at the expense of more free parameters. In the following, we discuss the ‘minimal’ model with 3 parameters, and refer the interested reader to Ref. [Die05] for a study of more general functional forms.

In Figs. 50, 51, the proton and neutron Sachs electric and magnetic FFs are shown for both models R1 and R2. One observes that the 3-parameter modified Regge model R2 gives a rather good overall description of the available FF data for both proton and neutron in the whole Q^2 range, using as value for the Regge trajectory $\alpha' = 1.105 \text{ GeV}^{-2}$, and the following values for the coefficients governing the $x \rightarrow 1$ behavior of the E -type GPDs: $\eta^u = 1.713$ and $\eta^d = 0.566$. Note that a value $\eta^q = 2$ corresponds to a $1/Q^2$ asymptotic behavior of the ratio F_2^q/F_1^q at large Q^2 .

In Figs. 50, 51, we also show the results of the 1-parameter Regge model R1, with the above value $\alpha' = 1.105 \text{ GeV}^{-2}$, which gives a good description of the proton charge radius. One sees from Figs. 50, 51 that the Regge model R1 is able to reproduce the main trends of both proton and neutron e.m. FF data for $Q^2 \leq 0.5 \text{ GeV}^2$. For higher values of Q^2 , however, it falls short of the data, as noted above. The Regge model R2 is able to describe existing data at larger Q^2 with relatively good accuracy, and the two additional parameters η^u and η^d in the R2 model, in particular, allow to describe the decreasing ratio of G_{Ep}/G_{Mp} with increasing Q^2 . The GPD parameterization R2 also leads to a zero for G_{Ep} at a momentum transfer of $Q^2 \simeq 8 \text{ GeV}^2$, which will be within the range covered by an upcoming JLab experiment [Bra04].

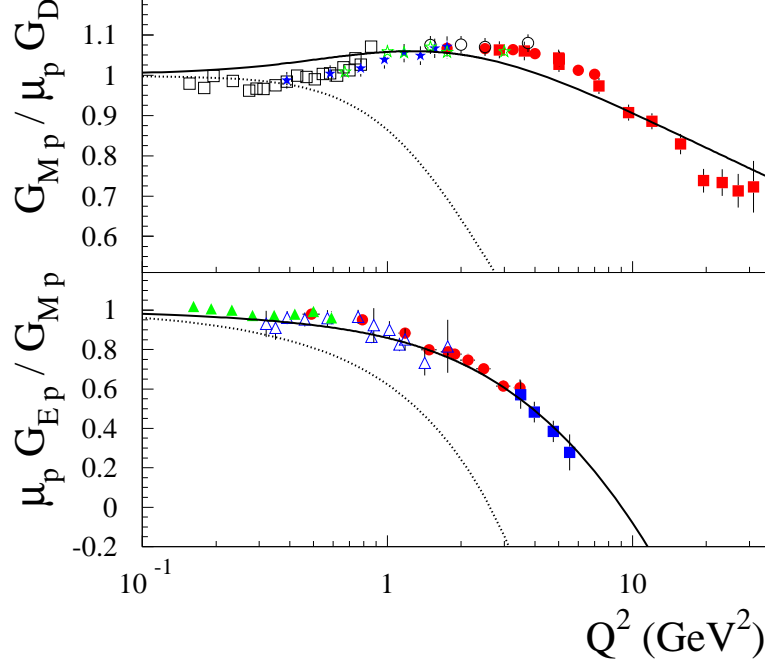


Figure 50: GPD calculation of the proton magnetic FF relative to the dipole G_D (upper panel), and ratio of proton electric over magnetic FFs (lower panel), according to Ref. [Gui05]. The dotted curves correspond to the Regge parameterization R1, with $\alpha' = 1.105 \text{ GeV}^{-2}$. The solid curves are for the 3 parameter modified Regge parameterization R2 : $\alpha' = 1.105 \text{ GeV}^{-2}$, $\eta^u = 1.713$ and $\eta^d = 0.566$. Data for G_{Mp} are from [Jan66] (open squares), [Lit70] (open circles), [Ber71] (blue solid stars), [Bar73] (green open stars), [And94] (red solid circles), [Arn86] (red solid squares), according to the recent re-analysis of Ref. [Bra02]. Data for the ratio G_{Ep}/G_{Mp} are from [Gay01] (blue open triangles), [Gay02] (blue solid squares), [Pun05] (red solid circles), and [Cra06] (green solid triangles).

4.6.3 GPDs and transverse structure of hadrons

The interplay between the x and Q^2 -dependence of the GPDs contains new nucleon structure information beyond the information encoded in forward parton distributions depending only on x , or FFs depending only on Q^2 . It has been shown that by a Fourier transform of the Q^2 -dependence of GPDs, it is conceivable to access the distributions of parton in the transverse plane, see Ref. [Bur00], and to provide a 3-dimensional picture of the nucleon [Bel04].

For $\xi = 0$, one can define the impact parameter versions of GPDs which are obtained through a Fourier integral in transverse momentum q_\perp . For the GPD H^q , this reads as:

$$H^q(x, \mathbf{b}_\perp) \equiv \int \frac{d^2 \mathbf{q}_\perp}{(2\pi)^2} e^{i\mathbf{b}_\perp \cdot \mathbf{q}_\perp} H^q(x, 0, -\mathbf{q}_\perp^2), \quad (90)$$

and an analogous definition for the GPD E^q . These impact parameter GPDs have the physical meaning of measuring the probability to find a quark which carries longitudinal momentum fraction x at a transverse po-

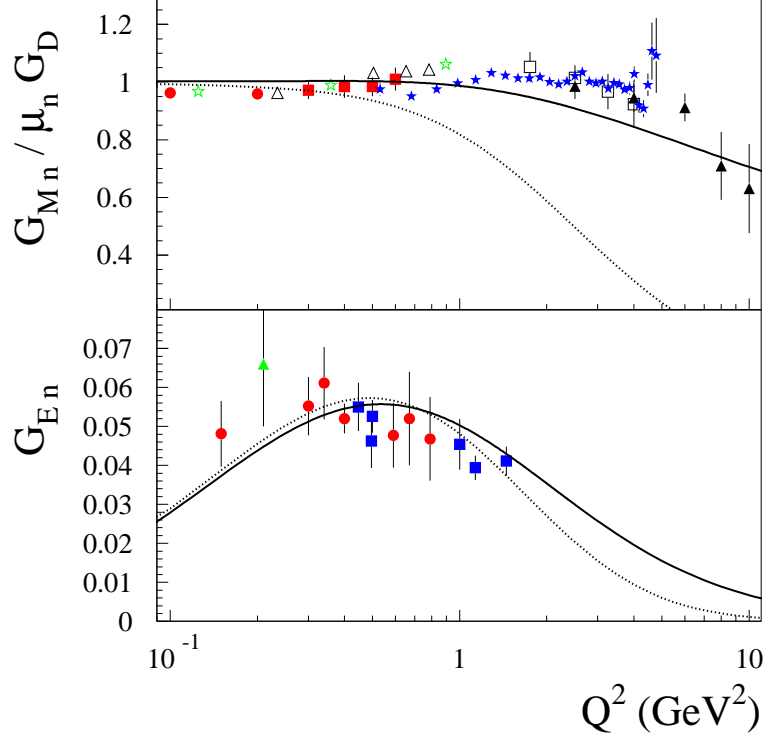


Figure 51: GPD calculation of the neutron magnetic FF relative to the dipole form (upper panel), and neutron electric FF (lower panel), according to Ref. [Gui05] with curve conventions as in Fig. 50. The data for G_{Mn} are from [Xu00] (red solid circles), [Xu03] (red solid squares), [Ank98] (open triangles), [Kub02] (green open stars), [Lun93] (open squares), [Roc82] (solid triangles), and [Bro05b] (blue solid stars). The data for G_{En} are from double polarization experiments at MAMI [Her99, Ost99, Bec99, Roh99, Gla05] (red solid circles), NIKHEF [Pas99] (green solid triangle), and JLab [Zhu01, Mad03, War04] (blue solid squares).

sition \mathbf{b}_\perp (relative to the transverse center-of-momentum) in a nucleon, see Refs. [Bur00, Bur03].

When translating the GPD parametrization R2 of Eqs. (83, 89) into the impact parameter space, one obtains :

$$H^q(x, \mathbf{b}_\perp) = q_v(x) \frac{e^{-\mathbf{b}_\perp^2 / [-4\alpha' (1-x) \ln x]}}{4\pi [-\alpha' (1-x) \ln x]}, \quad (91)$$

$$E^q(x, \mathbf{b}_\perp) = \frac{\kappa^q}{N^q} (1-x)^{\eta^q} q_v(x) \frac{e^{-\mathbf{b}_\perp^2 / [-4\alpha' (1-x) \ln x]}}{4\pi [-\alpha' (1-x) \ln x]}. \quad (92)$$

In Fig. 52, we display the impact parameter GPD $H^u(x, \mathbf{b}_\perp)$ for a valence up-quark in the proton according to Eq. (91). It is clearly seen from this image that for large values of x , the quark distributions are concentrated at small values of \mathbf{b}_\perp , reflecting the distribution of valence quarks in the core of the proton. On the other hand, at small values of x , the distribution in transverse position extends much further out.

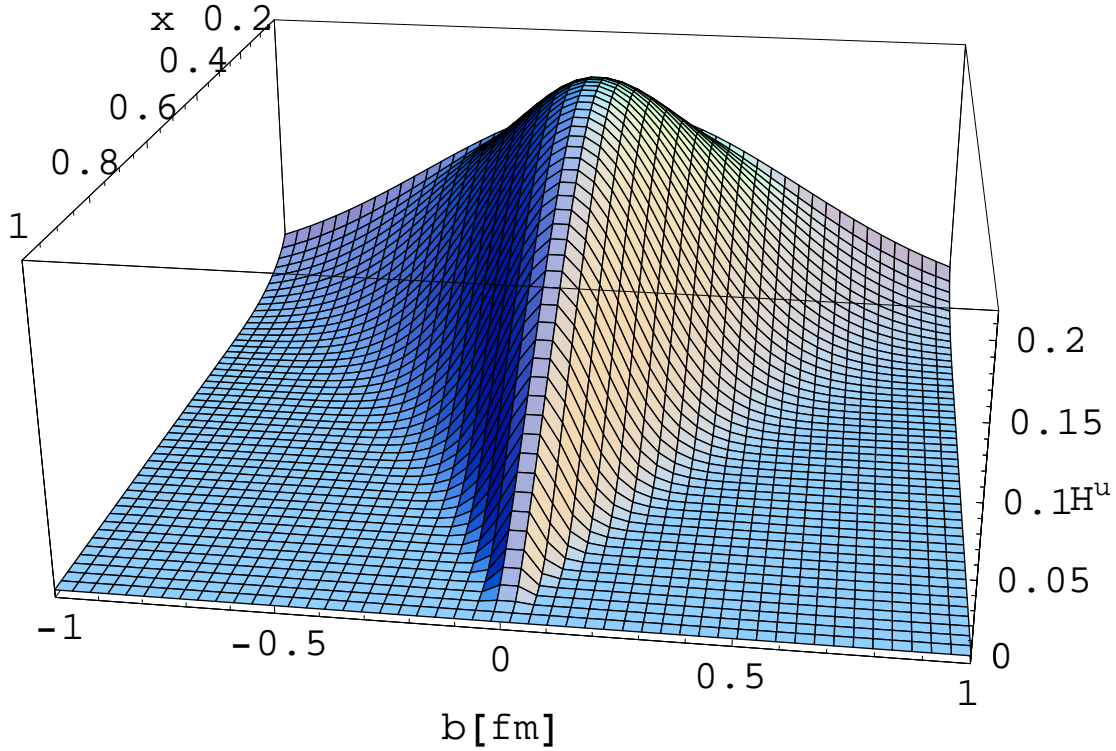


Figure 52: The GPD H^u for a valence up-quark in the proton as function of the quark momentum fraction x and the quark position b in the transverse plane (perpendicular to the average direction of the fast moving nucleons), where b stands for either $(b_\perp)_x$ or $(b_\perp)_y$. The calculation is based on the modified Regge parametrization R2 of Eq. (91).

4.7 Perturbative QCD (pQCD)

4.7.1 pQCD predictions for form factors

The nucleon e.m. FFs provide a famous test for perturbative QCD. Brodsky and Farrar derived scaling rules for dominant helicity amplitudes which are expected to be valid at sufficiently high momentum transfers Q^2 [Bro75]. A photon of sufficient high virtuality will see a nucleon consisting of three massless quarks moving collinear with the nucleon. When measuring an elastic nucleon form factor, the final state consists again of three massless collinear quarks. In order for this (unlikely process) to happen, the large momentum of the virtual photon has to be transferred among the three quarks through two hard gluon exchanges as illustrated in Fig. 53. This hard scattering mechanism is generated by valence quark configurations with small transverse size and finite light-cone momentum fractions of the total hadron momentum carried by each valence quark. The hard amplitude can be written in a factorized form [Che77a, Che77b, Efr79, Lep80], as a product of a perturbatively calculable hard scattering amplitude and two distribution amplitudes describing how the large longitudinal momentum of the initial and final nucleons is shared between their constituents. Because each gluon in such hard scattering process carries a virtuality proportional to Q^2 , this leads to the pQCD prediction that the helicity conserving nucleon Dirac form factor F_1 should fall as $1/Q^4$ (modulo $\ln Q^2$ factors) at sufficiently high Q^2 . Processes such as in Fig. 53, where the interactions among the quarks proceed via gluon or photon exchange, both of which are vector interactions, conserve the quark helicity in the limit when the quark masses or off-shell effects can be neglected. In contrast to the helicity conserving form factor F_1 , the

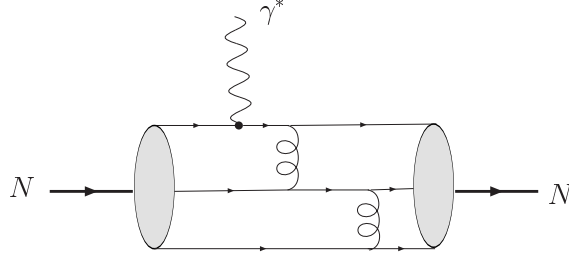


Figure 53: Perturbative QCD picture for the nucleon e.m. FFs. The highly virtual photon resolves the leading three-quark Fock states of the nucleon, described by a distribution amplitude. The large momentum is transferred between the quarks through two successive gluon exchanges (only one of several possible lowest-order diagrams is shown).

nucleon Pauli form factor F_2 involves a helicity flip between the initial and final nucleons. Hence it requires one helicity flip at the quark level, which is suppressed at large Q^2 . Therefore, for collinear quarks, i.e. moving in a light-cone wave function state with orbital angular momentum projection $l_z = 0$ (along the direction of the fast moving hadron), the asymptotic prediction for F_2 leads to a $1/Q^6$ fall-off at high Q^2 .

We can test how well the above pQCD scaling predictions for the nucleon e.m. FFs are satisfied at currently available momentum transfers, see Fig. 54. One firstly sees from Fig. 54 that the proton Dirac FF, which has been measured up to about 30 GeV^2 , displays an approximate $1/Q^4$ scaling above 10 GeV^2 . For the proton ratio F_{2p}/F_{1p} , the data up to 5.6 GeV^2 show no sign of a $1/Q^2$ behavior as predicted by pQCD. Instead, the data show that the ratio F_{2p}/F_{1p} falls less fast than $1/Q^2$ with increasing Q^2 . Belitsky, Ji, and Yuan [Bel03] investigated the assumption of quarks moving collinearly with the proton, which underlies the pQCD prediction. It has been shown in Ref. [Bel03] that by including components in the nucleon light-cone wave functions with quark orbital angular momentum projection $l_z = 1$, one obtains the behavior $F_2/F_1 \rightarrow \ln^2(Q^2/\Lambda^2)/Q^2$ at large Q^2 , with Λ a non-perturbative mass scale¹⁰. Choosing Λ in the range $0.2 - 0.4 \text{ GeV}$, Ref. [Bel03] found that the data for F_{2p}/F_{1p} support such double-logarithmic enhancement. The arguments of Ref. [Bel03] still rely on pQCD and it remains to be seen by forthcoming data at higher Q^2 if this prediction already starts in the few GeV^2 region.

4.7.2 The transition to pQCD

Although at high enough Q^2 , the pQCD scaling predictions should set in, the available data for the nucleon electromagnetic form factors show that one is still far away from this regime. This has been further investigated in several theoretical approaches.

Nesterenko and Radyushkin [Nes83] argued that the above described hard scattering mechanism is suppressed at accessible momentum transfers relative to the Feynman mechanism [Fey72], also called soft mechanism. The soft mechanism involves only one active quark, and the form factor is obtained as an overlap of initial and final hadron wave functions. The hard scattering mechanism on the other hand, involving three active quarks, requires the exchange of two gluons each of which brings in a suppression factor $\alpha_s/\pi \sim 0.1$. One therefore expects the hard scattering mechanism for F_{1p} to be numerically suppressed by a factor 1/100 compared to the soft term, see also Ref. [Bol95]. Even though the soft mechanism is suppressed asymptotically by a power of $1/Q^2$ relative to the hard scattering mechanism, it may well dominate at accessible values of

¹⁰In Refs. [Ral04, Bro03], it has also been discussed that inclusion of quark orbital angular momentum yields a ratio F_{2p}/F_{1p} which drops less fast than $1/Q^2$ with increasing Q^2 .

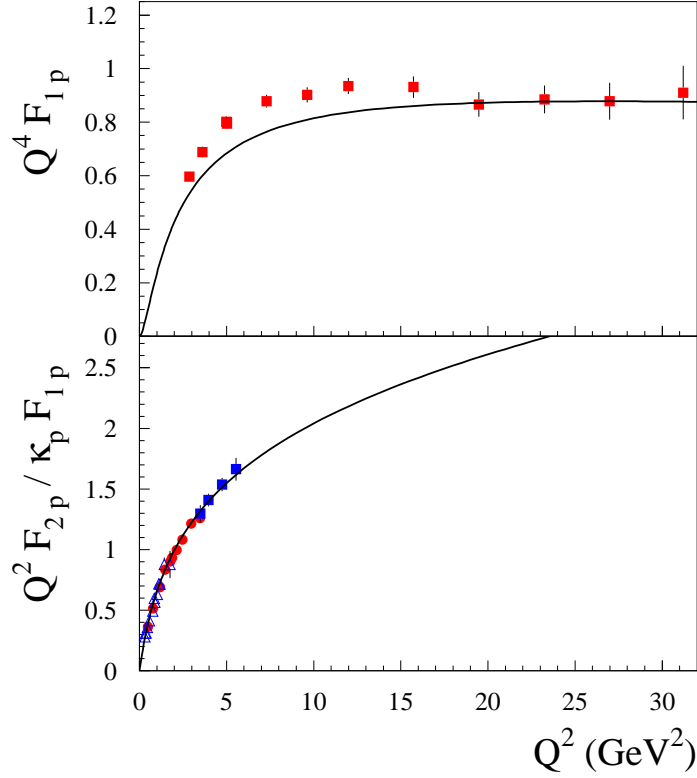


Figure 54: Test of the scaling behavior of the proton FFs. Upper panel : proton Dirac FF multiplied by Q^4 ; Lower panel : ratio of Pauli to Dirac proton FFs multiplied by Q^2 . The data for F_{1p} are from [Sil93] (solid squares). Data for the ratio F_{2p}/F_{1p} are from [Pun05] (red solid circles), [Gay01] (blue open triangles), and [Gay02] (blue solid squares). The curves represent the calculation based on the three parameter modified Regge GPD parametrization R2 of Ref. [Gui05].

Q^2 . In Ref. [Nes83], the soft contribution to the nucleon e.m. FFs was estimated using a model based on local quark-hadron duality. Within this approach, the soft contribution to the Dirac FF F_{1p} was found to yield an approximate $1/Q^4$ behavior at accessible momentum transfers in the range $Q^2 \sim 10 - 20 \text{ GeV}^2$, in qualitative agreement with the data.

The dominance of the soft mechanism in the nucleon e.m. FFs at accessible momentum transfers was also observed in diquark model calculations [Kro91].

In a more recent work, Braun *et al.* [Bra06], evaluated the soft contribution to the nucleon e.m. FFs within the light-cone sum rule (LCSR) approach. In this approach, one analyzes a matrix element, in which the final nucleon is represented by an interpolating field η . More specifically, one computes the correlation function of this interpolating field and the electromagnetic current operator J_ν given by the matrix element:

$$T_{\mu\nu}(P, q) = i \int d^4y e^{iq \cdot y} \langle 0 | T \{ \eta(0) J_\nu(y) \} | N(P) \rangle, \quad (93)$$

between the vacuum and a single-nucleon state $|N(P)\rangle$. At large space-like momentum transfer Q^2 and large space-like momentum flowing into the final hadronic state, the asymptotics of the above correlation function is governed by the light-cone kinematics $y^2 \rightarrow 0$, and can be studied by an operator product expansion on the light cone, $y^2 = 0$. It was found in Ref. [Bra06] that using asymptotic distribution amplitudes for the nucleon, the LCSR approach yields values of G_{Mp} and G_{Mn} which are within 20 % compatible with the data in the range $Q^2 \sim 1 - 10 \text{ GeV}^2$. The electric FFs however were found to be much more difficult to describe, with G_{En} overestimated, and G_{Ep}/G_{Mp} near constant when using an asymptotic nucleon distribution amplitude. Only when including twist-3 and twist-4 nucleon distribution amplitudes within a simple model, is a qualitative description of the electric proton and neutron FFs obtained. Such higher twist components hint at the importance of quark angular momentum components in the nucleon wave function.

In Sect. 4.6, we have shown that the nucleon e.m. FFs can be obtained from model independent GPD sum rules. These GPDs, represented by the lower blob in Fig. 48, are non-perturbative objects which include higher Fock components in the nucleon wave functions. One can use a GPD parametrization to provide an estimate of the soft contributions, and expects this non-perturbative approach to be relevant in the low and intermediate Q^2 region for the FFs. This is shown in Fig. 54 (solid curves) from which one sees that the GPD Regge parametrization $R2$, discussed in Sect. 4.6.2 is able to explain at the same time an approximate $1/Q^4$ behavior for F_{1p} and a behavior for F_{2p}/F_{1p} which falls less steep than $1/Q^2$. Forthcoming experiments at the Jefferson Lab 12 GeV facility will extend the data for F_{2p}/F_{1p} to Q^2 values around 13 GeV^2 . Such measurements will allow to quantify in detail the higher Fock components in the nucleon wave function (which are all included in the nucleon GPD) versus the simple three-quark Fock component, and to map out the transition to the perturbative QCD regime.

5 Conclusions and outlook

The increasingly common use of the double-polarization technique to measure the nucleon form factors, in the last 15 years, has resulted in a dramatic improvement of the quality of all four nucleon e.m. FFs, G_{Ep} , G_{Mp} , G_{En} and G_{Mn} . It has also completely changed our understanding of the proton structure, having resulted in a distinctly different Q^2 -dependence for G_{Ep} and G_{Mp} , which contradicted the prevailing wisdom of the 1990's based on cross section measurements and the Rosenbluth separation method, namely that G_{Ep} and G_{Mp} obey a “scaling” relation $\mu G_{Ep} \sim G_{Mp}$. One of the most direct consequences of the faster decrease of G_{Ep} revealed by the JLab polarization experiments was the disappearance of the early scaling $F_2/F_1 \sim 1/Q^2$ predicted by perturbative QCD.

The main origin of this abrupt change in results is now understood in simple terms. The faster decrease of G_{Ep} reduces its contribution to the cross section significantly below the natural ratio prevailing at small Q^2 , namely $G_{Ep}^2/G_{Mp}^2 \sim 1/\mu_p^2$. At the highest Q^2 for which we now have polarization data, 5.6 GeV^2 , the contribution from the electric FF to the cross section is less than 1%. As a direct consequence, the radiative corrections which affect the cross section by typically 10-30%, have become much more demanding. As discussed in Sect. 3.6, there is now a range of approaches to the calculation of radiative corrections of ep scattering, with differences in the approximations used and terms included, which results in variation of the correction by up to 4%. In particular, the corrections due to two hard photon exchange have been estimated in recent years in different model approaches. They were found to yield sizable corrections to the slope of the Rosenbluth plot, and may substantially reconcile the two ways of measuring G_{Ep}/G_{Mp} . The radiative corrections, including two hard photon exchange effects, affect the polarization only weakly, mostly because these are measurement of a ratio of FFs, and both FFs are, in first order, modified similarly. Until the origin of the difference between cross section- and polarization results is understood in full quantitative detail, it is safe to take the polarization results as the closest to the real, Born approximation, proton FFs.

The use of the polarization technique has also resulted in a constant progress in the measurement of G_{En} , which is intrinsically more difficult to obtain because of the smallness of this form factor, due to the overall zero charge of the neutron. Recent times have seen the maximum Q^2 for which we have polarization FFs grow to 1.5 GeV^2 , with new data obtained and under analysis up to 3.4 GeV^2 , and several experiments planned or proposed to significantly higher Q^2 values. Important progress has been made for G_{Mn} too, with new data with much improved error bars up to 4.8 GeV^2 .

On the theoretical side, the basic dipole structure of the nucleon e.m. FFs can be understood based on the vector meson dominance picture, in which the photon couples to the nucleon through the exchange of vector mesons. Dispersion analyses build on this picture by including, besides vector mesons, also non-resonant contributions in the coupling of the photon with the nucleon. State-of-the-art dispersion analyses include the 2π continuum as independent input in the isovector spectral function, and the $K\bar{K}$ and $\rho\pi$ continua as input in the isoscalar spectral function. Such approach is able to provide predictions for the nucleon FFs in both the space-like and time-like regions. The present dispersion analyses, which build in the pQCD prediction $F_2/F_1 \sim 1/Q^2$ as a constraint, are found to yield a reasonably good overall description of the data for all four nucleon e.m. FFs using a 15 parameter fit.

The effect of pionic degrees of freedom in the nucleon e.m. FFs can be systematically calculated within chiral effective field theory. The latest relativistic χ EFT calculations found that calculations based on pions and nucleons alone are not able to explain the nucleon e.m. FFs. Only upon inclusion of explicit vector meson degrees of freedom, these calculations were found to describe the FFs in the range $Q^2 \lesssim 0.4 \text{ GeV}^2$.

Calculations of the nucleon e.m. FFs within constituent quark models have highlighted the role of relativity

when trying to arrive at a microscopic description of nucleon FFs based on quark degrees of freedom in the few GeV^2 region. Although a complete calculation is independent of the specific choice of relativistic form chosen to describe the dynamics, present approximations destroy this independence.

We have also reviewed the recent progress made by lattice QCD calculations of the nucleon e.m. FFs. High statistics, unquenched lattice calculations have been performed using different actions. In present lattice simulations, disconnected diagrams, which are numerically more intensive, have not yet been evaluated. Therefore the current lattice calculations are for the isovector combinations of nucleon FFs where this disconnected diagram contribution drops out. The present lattice calculations are also performed at pion mass values above about 350 MeV and have to be extrapolated to the physical pion mass to allow for a comparison with experiment. A detailed comparison of the Q^2 dependence of the FFs has been performed using both dynamical Wilson fermions and a hybrid action consisting of domain wall valence quarks and staggered sea quarks. The dynamical Wilson calculations are able to provide a reasonably good description of the isovector Pauli FF F_2^V . At the lower Q^2 , the non-analytic terms in the chiral extrapolation were found to be important to arrive at a description of the isovector magnetic moment and Pauli radius. The present dynamical Wilson calculations largely overestimate the isovector Dirac form factor F_1^V however. In contrast, the results using the hybrid action are compatible for F_2^V , but differ from the Wilson results for F_1^V . The F_1^V results using the hybrid action are in qualitative better agreement with the data, and provide a first clear hint of the logarithmic m_π divergence in the isovector Dirac radius.

The quark structure of the $N \rightarrow N$ electromagnetic transition can be accessed in hard scattering processes such as deeply virtual Compton scattering. The non-perturbative information in this process can be parameterized in terms of generalized parton distributions, and the nucleon e.m. FFs can be obtained as first moment sum rules in the quark longitudinal momentum fraction x of these GPDs. In particular, the GPDs contain the information on the quark distribution of the nucleon anomalous magnetic moment which can not be accessed from inclusive deep inelastic scattering experiments. We discussed a GPD parameterization, which contains the forward parton distributions as input, and which extends the Regge behavior of the quark distributions to calculate the Q^2 dependence. The first moment of such a 3-parameter modified Regge parameterization was found to provide a good overall description of the nucleon e.m. FF data over the whole available Q^2 range. The resulting GPDs then yield, through a Fourier transform, the probability to find partons in the nucleon with a given momentum fraction x as function of their transverse positions. The modified Regge GPD parameterization predicts that, at moderately large Q^2 values, F_{1p} follows an approximate $1/Q^4$ scaling, whereas F_{2p}/F_{1p} drops less fast than the $1/Q^2$ pQCD behavior, in agreement with the polarization data. It furthermore predicts that G_{Ep} reaches a zero around $Q^2 \sim 8 \text{ GeV}^2$, which is in the reach of an upcoming experiment.

We like to end this review by spelling out a few open issues and challenges (both theoretical and experimental) in this field :

1. *Quantifying the two-photon exchange processes experimentally, and improving their theoretical understanding*

In order to use electron scattering as a precision tool, it is clearly worthwhile to arrive at a quantitative understanding of two-photon exchange processes. This calls for detailed experimental studies, and several new experiments are already planned. Differences between elastic e^- and e^+ scattering on a proton target directly access the real part of the two-photon exchange amplitude. The predicted small effect of two-photon processes on the polarization data can be checked by measuring the ϵ dependence in polarization transfer experiments. These upcoming experiments also call for further refinements on

the theoretical side.

2. Dispersion analyses

In the present dispersion analysis for the nucleon e.m. FFs, the pQCD limit $F_2/F_1 \sim 1/Q^2$ was built in as a constraint, although the data do not support this limit. It might therefore be worthwhile to investigate how the dispersion fits change by removing this bias from the analysis, when fitting data at the largest available Q^2 values.

3. Relativistic constituent quark model calculations

The quality of the commonly introduced impulse approximation when describing nucleon FFs in relativistic constituent quark models may differ between different forms. As a next step for CQMs, it would clearly be worthwhile to investigate the approximations made in the current operator within each form, and quantify e.g. the effect of explicit two-body currents.

4. Lattice calculations and chiral extrapolations

- (a) One would clearly like to understand the present disagreement between the unquenched lattice predictions when using different actions (Wilson action vs. hybrid action). Understanding the structure of the FFs at low Q^2 , such as the Dirac charge radius, depends crucially on the effect of pion loops, which yield strong non-analytic dependence (in particular a $\log m_\pi$ singularity). At the larger Q^2 values, between 0.5 and 2 GeV^2 , the effects of pion loops are expected to be reduced however. One may therefore suspect that the differences between different actions at larger Q^2 values are due to discretization errors, which have only partly been studied. As the present lattice calculations for the FFs have been performed for a single lattice spacing, unquenched calculations at a couple of different lattice spacings using both the Wilson and hybrid actions would be very helpful to shed a further light on this issue.
- (b) In order to provide lattice predictions for proton and neutron e.m. FFs separately, the calculation of the disconnected diagrams awaits the next generation of dynamical fermion lattice QCD simulations.
- (c) A further challenge for the lattice calculations is a fully consistent treatment of both valence and sea quarks which respect chiral symmetry on the lattice.
- (d) As future lattice calculations for pion mass values around and below 300 MeV become available for FFs in the range $Q^2 \gtrsim 0.5 \text{ GeV}^2$, i.e. beyond the range where present χPT calculations are applicable, one is confronted with a two-scale problem. A challenge is to theoretically study the extrapolation (in the small scale m_π) in the presence of a (moderately) large scale Q^2 .

5. Precision measurements in the low Q^2 regime

Precision measurements of the nucleon e.m. FFs in the Q^2 range below 0.5 GeV^2 , may bring the effects of the pion could sharper into focus. In this respect, new measurements for G_{En} currently analyzed by the BLAST Coll., will allow to better quantify the conjectured “bump” structure in G_{En} around $Q^2 \sim 0.3 \text{ GeV}^2$.

6. Extending the FF measurements to larger Q^2

The anticipated upgrade of JLab to 12 GeV beam energy, offers promises of measurements of all four FFs up to or larger than $\sim 10 \text{ GeV}^2$. It is unlikely that we will see indications of a clear departure from the soft physics dominance to the hard collision regime of pQCD. However these data will constrain the parameterizations of GPDs and yield information on the spatial distribution of partons which carry a large momentum fraction of the nucleon momentum, i.e. partons with $x \sim 1$.

The recent unexpected results in the nucleon e.m. FFs using double-polarization high-precision experiments, have challenged our theoretical understanding of the structure of the nucleon. They have triggered several new theoretical developments, which were reviewed in this work. As a result of the unexpected findings, several further experiments are planned, which will bring the quark-gluon structure of the most common constituent of visible matter in the universe into sharper focus.

Acknowledgements

We like to thank C. Alexandrou, T. Averett, D. Day, K. Orginos, V. Pascalutsa, B. Pasquini, and T. Walcher, for useful discussions and correspondence during the course of this work and E.J. Brash and B. Mecking for their careful reading of the experimental sections.

C.F. P. acknowledges support from a National Science Foundation grant, PHY-0456645. The work of V. P. is supported by the Physics Division, Department of Energy, grant DE-FG02-89ER40525. Furthermore, the work of M. V. is supported in part by DOE grant DE-FG02-04ER41302 and contract DE-AC05-06OR23177 under which Jefferson Science Associates operates the Jefferson Laboratory.

References

- [Ada97] Adams D. *et al*, Phys. Rev. D **56**, 5330 (1997).
- [Adl01] Adloff C. *et al*. [H1 Collaboration], Phys. Lett. B **517**, 47 (2001).
- [Afa98] Afanasev A. V., arXiv:hep-ph/9808291.
- [Afa99] Afanasev A. V., arXiv:hep-ph/9910565.
- [Afa01] Afanasev A. V., I. Akushevich, A Ilyichev and N. P. Merenkov, Phys. Lett. B **514**, 269 (2001).
- [Afa04] Afanasev, A. *et al.*, JLab proposal E04-116 (2004).
- [Afa05b] Afanasev A.V., private communication (2005).
- [Afa05] Afanasev A. V., S. J. Brodsky, C. E. Carlson, Y. C. Chen and M. Vanderhaeghen, Phys. Rev. D **72**, 013008 (2005).
- [Air01] Airapetian A. *et al*. [HERMES Collaboration], Phys. Rev. Lett. **87**, 182001 (2001).
- [Air06] Airapetian A. *et al*. [HERMES Collaboration], arXiv:hep-ex/0605108.
- [Akh68] Akhiezer A. I. and M. P. Rekalo, Sov. Phys. - Doklady **13**, 572 (1968).
- [Akh74] Akhiezer A. I. and M. P. Rekalo, Sov. J. Part. Nucl. **3**, 277 (1974).
- [Akt05] Aktas A. *et al*. [H1 Collaboration], Eur. Phys. J. C **44**, 1 (2005).
- [Alc04] Alcorn J. *et al.*, Inst. Meth. in Phys. Res. **A522**, 294 (2004).
- [Ale99] Alekseev I. A. *et al.*, 1.35-GeV/c Nucl. Instrum. Meth. A **434**, 254 (1999).
- [Ale06a] Alexandrou C., G. Koutsou, J. W. Negele and A. Tsapalis, Phys. Rev. D **74**, 034508 (2006).
- [Ale06b] Alexandrou C., arXiv:hep-lat/0608025.
- [Alg76] Alguard M. J. *et al.*, Phys. Rev. Lett. **37**, 1258 (1976).
- [And94] Andivahis L. *et al.*, Phys. Rev. D **50**, 5491 (1994); P. E. Bosted *et al*, Phys. Rev. Lett. **68**, 3841 (1992).
- [And06] Anderson B. *et al*. [Jefferson Lab E95-001 Collaboration], arXiv:nucl-ex/0605006.
- [Ank94] Anklin H. *et al.*, Phys. Lett. B **336**, 313 (1994).
- [Ank98] Anklin H. *et al.*, Phys. Lett. B **428**, 248 (1998).
- [Are87] Arenhövel H., Phys. Lett. B **199**, 13 (1987); H. Arenhövel, W. Leidemann, and E. L. Tomusiak, Z. Phys. A **331**, 123 (1988).
- [Arn81] Arnold R. G., C.E. Carlson, and F. Gross, Phys. Rev. C **23**, 363 (1981).

- [Arn86] Arnold R. G. *et al.*, Phys. Rev. Lett. **57**, 174 (1986). Sill A. F. *et al.*, Phys. Rev. D **48**, 29 (1993).
- [Arr03] Arrington J., Phys. Rev. C **68**, 034325 (2003).
- [Arr04] Arrington J. *et al.*, JLab Proposal E-05-017 (2005).
- [Arr05] Arrington, J., JLab proposal E05-017 (2005).
- [Ash04] Ashley J. D., D.B. Leinweber, A.W. Thomas and R.D. Young, Eur. Phys. J. A **19**, 9 (2004).
- [Ash88] Ashman J. *et al*, Phys. Lett. B **206**, 364 (1988).
- [Ave05] Averett T., J.P. Chen and X. Jiang, JLab experiment E-05-015 (2005).
- [Azh04] Azhgirey L. S. *et al*, Nucl. Inst. and Methods in Phy. Res. A **538**, 431 (2004).
- [Azn93] Aznauryan I. G., Phys. Lett. B **316**, 391 (1993).
- [Bar99] Barkhuff D. *et al.*, Phys. Lett. **470**, 39 (1999).
- [Bar73] Bartel W. *et al.*, Nucl. Phys. B **58**, 429 (1973).
- [Bar68] Barut A.O., Corrigan Dennis, and Kleinert H., Phys. Rev. Lett. **20**, 167 (1968).
- [Bec97] Beck R. *et al.*, Phys. Rev. Lett. **78**, 606 (1997); Phys. Rev. C **61**, 035204 (2000).
- [Bec99] Becker J. *et al.*, Eur. Phys. J. A **6**, 329 (1999).
- [Bei05] Beise E. J., M. L. Pitt and D. T. Spayde, Prog. Part. Nucl. Phys. **54**, 289 (2005).
- [Bel03] Belitsky A. V., X. d. Ji and F. Yuan, Phys. Rev. Lett. **91**, 092003 (2003).
- [Bel04] Belitsky A. V., X. d. Ji and F. Yuan, Phys. Rev. D **69**, 074014 (2004).
- [Bel05] Belitsky A. V. and A. V. Radyushkin, Phys. Rept. **418**, 1 (2005).
- [Bel05] Belushkin M. A., H. W. Hammer and U. G. Meissner, Phys. Lett. B **633**, 507 (2006).
- [Bel06] Belushkin M. A., H. W. Hammer and U. G. Meissner, arXiv:hep-ph/0608337.
- [Ben64] Benaksas D., D. Drikey and D. Frerejacque, Phys. Rev. Lett. **13**, 353 (1964), and D. Benaksas, D. Drikey and D. Frerejacque, Phys. Rev. **148**, 1327 (1966).
- [Ber76] Berestetsky V. B. and M. V. Terentev, Sov. J. Nucl. Phys. **24**, 547 (1976) [Yad. Fiz. **24**, 1044 (1976)]; **25**, 347 (1977) [**25**, 653 (1977)].
- [Ber71] Berger Ch. *et al.*, Phys. Lett. B **35**, 87 (1971).
- [Ber03] Bermuth J. *et al.*, Phys. Lett. B **564**, 199 (2003).
- [Ber98] Bernard V., H. W. Fearing, T. R. Hemmert and U. G. Meissner, Nucl. Phys. A **635**, 121 (1998) [Erratum-ibid. A **642**, 563 (1998 NUPHA,A642,563-563.1998)].

- [Ber00] Bernard C. *et al.*, Phys. Rev. D **61**, 111502(R) (2000); K. Orginos, D. Tousaint and R. L. Sugar, Phys. Rev. D **60**, 054503 (1999).
- [Ber95] Bertz M., COSY INFINITY version 7, NSCL Tech. Rep., MSUCL-977, Michigan State University (1995).
- [Bij04] Bijker R. and F. Iachello, Phys. Rev. C **69**, 068201 (2004).
- [Bil93] Bilenky S. M., C. Giunti and V. Wataghin, Z. Phys. C **59**, 475 (1993).
- [Bla84] Blankleider B. and R. M. Woloshyn, Phys. Rev. C **29**, 538 (1984).
- [Bla97] Blanpied G. *et al.* [LEGS Collaboration], Phys. Rev. Lett. **79**, 4337 (1997); Phys. Rev. C **64**, 025203 (2001).
- [Blu03] Blunden P. G., W. Melnitchouk and J. A. Tjon, Phys. Rev. Lett. **91**, 142304 (2003); Phys. Rev. C **72**, 034612 (2005).
- [Bof01] Boffi S., L. Y. Glozman, W. Klink, W. Plessas, M. Radici and R. F. Wagenbrunn, Eur. Phys. J. A **14**, 17 (2002).
- [Boh75] Bohr A. and B. Mottelson, *Nuclear Structure II* (Benjamin, Reading, MA, 1975).
- [Boi06] Boinepalli S., D. B. Leinweber, A. G. Williams, J. M. Zanotti and J. B. Zhang, Phys. Rev. D **74**, 093005 (2006).
arXiv:hep-lat/0604022.
- [Bol95] Bolz J., R. Jakob, P. Kroll, M. Bergmann and N. G. Stefanis, Z. Phys. C **66**, 267 (1995).
- [Bos95] Bosted P. E., Phys. Rev. C **51**, 409 (1995).
- [Bou96] Bourseix S. *et al.*, Phys. Rev. Lett. **76**, 384 (1996).
- [Bra02] Brash E. J., A. Kozlov, S. Li and G. M. Huber, Phys. Rev. C **65**, 051001 (2002).
- [Bra04] Brash E. *et al.*, JLab Proposal 04-108 (2004).
- [Bra06] Braun V. M., A. Lenz and M. Wittmann, Phys. Rev. D **73**, 094019 (2006).
- [Bro75] Brodsky S. J. and G.R. Farrar, Phys. Rev. D **11**, 1309 (1975).
- [Bro03] Brodsky S. J., J. R. Hiller, D. S. Hwang and V. A. Karmanov, Phys. Rev. D **69**, 076001 (2004).
- [Bro05a] Brodsky S. J., C.E. Carlson, J.H. Hiller and D. S. Hwang, Phys. Rev. Lett. **94**, 022001 (2005).
- [Bro05b] Brooks W. K. and J. D. Lachniet [CLAS Collaboration], Nucl. Phys. A **755**, 261 (2005), and J.D. Lachniet, PhD thesis, Carnegie Mellon University, unpublished (2005)
- [Bru95] Bruins E. E. W. *et al.*, Phys. Rev. Lett. **75**, 21 (1995).
- [Bru97] Bruins, E. E. W., *et al.*, Phys. Rev. Lett. **79**, 5187 (1997)

- [Buc01] Buchmann A. J. and E. M. Henley, Phys. Rev. C **63**, 015202 (2001); Phys. Rev. D **65**, 073017 (2002).
- [Buc02] Buchmann A. J., J. A. Hester and R. F. Lebed, Phys. Rev. D **66**, 056002 (2002).
- [Bud68] Budnitz R. G. *et al*, Phys. Rev. **173**, 1357 (1968).
- [Bum60] Bumiller F., M. Croissiaux and R. Hofstadter, Phys. Rev. Lett. **5**, 261 (1960); R. Hofstadter, F. Bumiller, and M. Croissiaux, Phys. Rev. Lett. **5**, 263 (1960).
- [Bur00] Burkardt M., Phys. Rev. D **62**, 071503 (2000) [Erratum-ibid. D **66**, 119903 (2002)].
- [Bur03] Burkardt M., Int. J. Mod. Phys. A **18**, 173 (2003).
- [Bur04] Burkardt M., Phys. Lett. B **595**, 245 (2004).
- [Bys06] Bystritskiy Yu. M., E. A. Kuraev and E. Tomasi-Gustafsson, arXiv:hep-ph/0603132.
- [Cap86] Capstick S. and N. Isgur, Phys. Rev. D **34**, 2809 (1986).
- [Car95] Cardarelli F., E. Pace, G. Salme and S. Simula, Phys. Lett. B **357**, 267 (1995).
- [Car00] Cardarelli F. and S. Simula, Phys. Rev. C **62**, 65201 (2000).
- [Cat03] Cates, G., K. McCormick, B. Reitz and B. Wojtsekhowski, JLab proposal 02-13, (2002).
- [Che03] Chekanov S. *et al*. [ZEUS Collaboration], Phys. Lett. B **573**, 46 (2003).
- [Che06] Chen S. *et al*. [CLAS Collaboration], Phys. Rev. Lett. **97**, 072002 (2006).
- [Che04] Chen Y. C., A. Afanasev, S.J. Brodsky, C.E. Carlson and M. Vanderhaeghen, Phys. Rev. Lett. **93**, 122301 (2004);
- [Che77a] Chernyak V. L. and A. R. Zhitnitsky, JETP Lett. **25**, 510 (1977) [Pisma Zh. Eksp. Teor. Fiz. **25**, 544 (1977)].
- [Che77b] Chernyak V. L., A. R. Zhitnitsky and V. G. Serbo, JETP Lett. **26**, 594 (1977) [Pisma Zh. Eksp. Teor. Fiz. **26**, 760 (1977)].
- [Che95] Cheung N. E. *et al*., Nucl. Instrum. Meth. A **363** (1995) 561.
- [Cho55] Chodorow M., E.L. Ginzton, W.W. Hansen, R.L. Kyhl, R.B. Neal and W.K.H. Panofsky, Rev. Scient. Inst. **26**, 134 (1955)
- [Chr95] Christov C. V., A. Z. Gorski, K. Goeke and P. V. Pobylitsa, Nucl. Phys. A **592**, 513 (1995)
- [Chr96] Christov Chr. V., A. Blotz, H.-C. Kim, P. Pobylitsa, T. Watabe, Th. Meissner, E. Ruiz Arriola and K. Goeke, Prog. Part. Nucl. Phys. **37**, 91 (1996).
- [Chr04] Christy M. E. *et al*., Phys. Rev. C **70**, 015206 (2004).
- [Chu91] Chung P. L. and F. Coester, Phys. Rev. D **44**, 229 (1991).

- [Cle56] Clementel E. and C. Villi, Nuov. Cim **4**, 1207, (1956).
- [Coe03] Coester F. and D. O. Riska, Nucl. Phys. A **728**, 439 (2003).
- [Col99] Collins J. C. and A. Freund, Phys. Rev. D **59**, 074009 (1999).
- [Cow68] Coward D. H. *et al.*, Phys Rev Lett **20**, 292 (1968).
- [Cra95] Crabb D. G. and D. B. Day, Nucl. Instrum. Meth. A **356**, 9 (1995).
- [Cra06] Crawford C. B. *et al.*, arXiv:nucl-ex/0609007.
- [DeR75] De Rujula A., H. Georgi and S.L. Glashow, Phys. Rev. D **12**, 147 (1975).
- [DeS00] De Sanctis M., M.M. Giannini, L. Repetto, and E. Santopinto, Phys. Rev. C **62**, 025208 (2000).
- [Des04] Desplanques B. and L. Theussl, Eur. Phys. J. A **21**, 93 (2004).
- [Des06] Desplanques B., arXiv:nucl-th/0510003.
- [Dia86] Diakonov D. I. and V. Petrov, Nucl. Phys. **B272**, 457 (1986).
- [Dia88] Diakonov D. I., V. Petrov and P. Pobylitsa, Nucl. Phys. **B306**, 809 (1988).
- [Die99] Diehl M., T. Feldmann, R. Jakob and P. Kroll, Eur. Phys. J. C **8**, 409 (1999).
- [Die03] Diehl M., Phys. Rept. **388**, 41 (2003).
- [Die05] Diehl M., T. Feldmann, R. Jakob and P. Kroll, Eur. Phys. J. C **39**, 1 (2005).
- [Die01] Dietrich S. *et al.*, Phys. Lett. B **500**, 47 (2001).
- [Dil99] Dillon G. and G. Morpurgo, Phys. Lett. B **459**, 321 (1999).
- [Dir49] Dirac P.A.M., Rev. Mod. Phys. **21**, 392 (1949).
- [Dom69] Dombey N., Rev. Mod. Phys. **41**, 236 (1969).
- [Don86] Donnelly T. W. and A.S. Raskin, Ann. Phys. **169**, 247 (1986).
- [Dre66] Drell S. D. and A. C. Hearn, Phys. Rev. Lett. **16**, 908 (1966).
- [Dri62] Drickey D. J. and L.N. Hand, Phys. Rev. Lett. **9**, 521 (1962).
- [Dub05] Dubnicka S., E. Kuraev, M. Secansky and A. Vinnikov, arXiv:hep-ph/0507242.
- [Dun02] Dunne G. V., A. W. Thomas and S. V. Wright, Phys. Lett. B **531**, 77 (2002).
- [Dun66] Dunning J. R. *et al*, Phys. Rev. **141**, 1286 (1966).
- [Dzi97] Dziembowski Z. *et al.*, Ann. of Phys. **258**, 1 (1997).
- [Ede94] Eden T. *et al.*, Phys Rev. C **50**, 1749 (1994).

- [Edw06] Edwards R. G. *et al.* [LHPC Collaboration], arXiv:hep-lat/0610007.
- [Efr79] Efremov A. V. and A. V. Radyushkin, Phys. Lett. B **94**, 245 (1980).
- [Ent01] Ent R., B.W. Fillipone, N.C.R. Makins, R.G. Milner, T.G. O'Neill and D.A. Wasson, Phys. Rev. C **64**, 054610 (2001).
- [Ern60] Ernst F. J., R.G. Sachs, and K.C. Wali, Phys. Rev. **119**, 1105 (1960).
- [Eyl95] Eyl D. *et al.*, Z. Phys. A **352**, 211 (1995).
- [Fae06] Faessler A., T. Gutsche, V. E. Lyubovitskij and K. Pumsa-ard, Phys. Rev. D **73**, 114021 (2006).
- [Far04] Farchioni F. *et al.*, hep-lat/0512017; R. Frezzotti and G. Rossi, JHEP 0408, 007 (2004); JHEP 0410, 070 (2004).
- [Fer47] Fermi E. and L. Marshall, Phys. Rev. **72**, 1139 (1947).
- [Fes67] Feshbach H. and E. Lomon, Rev. Mod. Phys. **39**, 611 (1967).
- [Fey72] Feynman R. P., *Photon-Hadron Interactions* (Benjamin, Reading, MA, 1972).
- [Fol52] Foldy L. L., Phys. Rev. **87**, 688 (1952).
- [Fra59] Frazer W. R. and J. R. Fulco, Phys. Rev. Lett. **2**, 365 (1959); Phys. Rev. **117**, 1609 (1960).
- [Fra96] Frank M. R., B.K. Jennings, and G.A. Miller, Phys. Rev. C **54**, 920 (1996).
- [Fri05] Friar J. L. and I. Sick, arXiv:nucl-th/0508025.
- [Fri60] Friedman J. I., H.W. Kendall and P.A.M. Gram, Phys. Rev. **120**, 992 (1960).
- [Fri03] Friedrich J. and Th. Walcher, Eur. Phys. J. A **17**, 607 (2003).
- [Fuc04] Fuchs T., J. Gegelia and S. Scherer, J. Phys. G **30**, 1407 (2004).
- [Gal71] Galster S. *et al.*, Nucl. Phys. **B32**, 221 (1971).
- [Gao94] Gao H. Y. *et al.*, Phys Rev. C **50**, R546 (1994).
- [Gao03] Gao H. Y., Int. J. Mod. Phys. E **12**, 1 (2003) [Erratum-ibid. E **12**, 567 (2003)] [arXiv:nucl-ex/0301002].
- [Gar85] Gari M. F. and W. Krümpelmann, Z. Phys. A **322**, 689 (1985) 689; Phys. Lett. B **274**, 159 (1992); Phys. Lett. B **282**, 483(E) (1992).
- [Gay01] Gayou O. *et al.*, Phys. Rev. C **64**, 038202 (2001).
- [Gay02] Gayou O. *et al.* [Jefferson Lab Hall A Collaboration], Phys. Rev. Lett. **88**, 092301 (2002).
- [Ger66] Gerasimov S. B., Sov. J. Nucl. Phys. **2**, 430 (1966) [Yad. Fiz. **2**, 598 (1966)].

- [Gla79] Glashow S. L., *Physica* **96A**, 27 (1979).
- [Gla05] Glazier D. *et al.*, *Eur. Phys.J. A* **24**, 101 (2005).
- [Glo98a] Glozman L. Y., Z. Papp, W. Plessas, K. Varga and R. F. Wagenbrunn, *Phys. Rev. C* **57**, 3406 (1998).
- [Glo98b] Glozman L. Y., W. Plessas, K. Varga and R. F. Wagenbrunn, *Phys. Rev. D* **58**, 094030 (1998).
- [Goc05] Göckeler M., T. R. Hemmert, R. Horsley, D. Pleiter, P. E. L. Rakow, A. Schäfer and G. Schierholz [QCDSF Collaboration], *Phys. Rev. D* **71**, 034508 (2005).
- [Goc06] Göckeler M. *et al.* [QCDSF/UKQCD Collaboration], arXiv:hep-lat/0610118.
- [Goe01] Goeke K., M. V. Polyakov and M. Vanderhaeghen, *Prog. Part. Nucl. Phys.* **47**, 401 (2001).
- [Goi67] Goitein, M. *et al.*, *Phys. Rev. Lett.* **18**, 1016 (1967) and Goitien, M., J.R. Dunning, Jr. and Richard Wilson, *Phys. Rev. Lett.* **18**, 1018 (1967).
- [Gol01] Golak J. *et al.*, *Phys Rev. C* **63**, 034006 (2001).
- [Gou64] Gourdin M., *Nuov. Cim.* **33**, 533 (1963) and **32E**, 493 (1964).
- [Gro06] Gross F. and P. Agbakpe, *Phys. Rev. C* **73**, 015203 (2006).
- [Gro66a] Grossetête B., D. Drickey and P. Lehmann, *Phys. Rev.* **141**, 1425 (1966).
- [Gro66b] Grossetête B., S. Julian and P. Lehmann, *Phys. Rev.* **141**, 1435 (1966).
- [Gui03] Guichon P. A. M. and M. Vanderhaeghen, *Phys. Rev. Lett.* **91**, 142303 (2003).
- [Gui05] Guidal M., M. V. Polyakov, A. V. Radyushkin and M. Vanderhaeghen, *Phys. Rev. D* **72**, 054013 (2005).
- [Ham62] Hamada T. and J.D. Johnston, *Nucl. Phys.* **34**, 382 (1962).
- [Ham96] Hammer H. W., U. G. Meissner and D. Drechsel, *Phys. Lett. B* **385**, 343 (1996).
- [Ham99] Hammer H. W. and M. J. Ramsey-Musolf, *Phys. Rev. C* **60**, 045204 (1999) [Erratum-ibid. C **62**, 049902 (2000)]; *Phys. Rev. C* **60**, 045205 (1999) [Erratum-ibid. C **62**, 049903 (2000)].
- [Ham04] Hammer H.-W. and Ulf-G. Meissner, *Eur. Phys. J. A* **20**, 469 (2004).
- [Han63] Hand L. N., D.G. Miller, and R. Wilson, *Rev. Mod. Phys.* **35**, 335 (1963).
- [Han73] Hanson K. M. *et al.* *Phys. Rev. D* **8**, 753 (1973).
- [Hau98] Hauser P. *et al.*, proposal for an experiment at Paul Scherrer Institute, Villigen, No. R-98-03.1, 1998 (unpublished)
- [Hem97] Hemmert T. R., B. R. Holstein and J. Kambor, *Phys. Lett. B* **395**, 89 (1997); *J. Phys. G* **24**, 1831 (1998).

- [Hem02] Hemmert T. R. and W. Weise, Eur. Phys. J. A **15**, 487 (2002).
- [Her99] Herberg C. *et al.*, Eur. Phys. J. A **5**, 131 (1999).
- [Hof53a] Hofstadter R., H.R. Fecher and J.A. McIntyre, Phys. Rev. **91**, 422 (1953).
- [Hof53b] Hofstadter R., H.R. Fecher and J.A. McIntyre, Phys. Rev. **92**, 978 (1953).
- [Hof55] Hofstadter R. and R. W. McAllister, Phys. Rev. **98**, 217 (1955).
- [Hof56] Hofstadter R., Rev. Mod. Phys. **28**, 214 (1956).
- [Hof58] Hofstadter R., F. Bumiller and M.R. Yearian, Rev. Mod. Phys. **30**, 482 (1958).
- [Hof60] Hofstadter R. in Proc. of 9th Intern. Ann. Conference on High Energy Physics Academy of Science USSR, Moscow 1960), vol. I, p. 355.
- [Hoh75] Höhler G. and E. Pietarinen, Nucl. Phys. B **95**, 210 (1975).
- [Hoh76] Höhler G. *et al.*, Nucl. Phys. B **114**, 505 (1976).
- [Hol05] Holstein B. R., V. Pascalutsa and M. Vanderhaeghen, Phys. Rev. D **72**, 094014 (2005).
- [Hol96] Holzwarth G., Z Phys. A **356**, 339 (1996); G. Holzwarth, hep-ph/0201138 v1 (2002).
- [Hol05] Holzwarth G., arXiv:hep-ph/0511194.
- [Hu06] Hu B. *et al.*, Phys. Rev. C **73**, 064004 (2006).
- [Hug65] Hughes E. B., T.A. Griffy, M.E. Yearian and R. Hofstadter, Phys. Rev. **139**, B458 (1965).
- [Hyd04] Hyde-Wright C. E. and K. de Jager, Ann. Rev. Nucl. Part. Sci. **54**, 217 (2004).
- [Iac73] Iachello F., A.D. Jackson, and A. Landé, Phys. Lett. B **43**, 191 (1973).
- [Iac04] Iachello F. and Q. Wan, Phys. Rev. C **69**, 055204 (2004).
- [Isg78] Isgur N. and G. Karl, Phys. Rev. D **18**, 4187 (1978); **19**, 2653 (1979); **20**, 1191 (1979); C. Hayne and N. Isgur, *ibid* **25**, 1944 (1982).
- [Isg82] Isgur N., G. Karl and R. Koniuk, Phys. Rev. D **25**, 2394 (1982).
- [Isg99] Isgur N., Phys. Rev. Lett. **83**, 272 (1999).
- [Jan66] Janssens T., R. Hofstadter, E.B. Hughes and M.R. Yearian, Phys. Rev. **142**, 922 (1966).
- [Ji97] Ji X. D., Phys. Rev. Lett. **78**, 610 (1997); Phys. Rev. D **55**, 7114 (1997).
- [Ji98a] Ji X. D. and J. Osborne, Phys. Rev. D **58**, 094018 (1998).
- [Ji98b] Ji X. D., J. Phys. G **24**, 1181 (1998).

- [Ji03] Ji Xiangdong, Phys. Rev. Lett. **91**, 062001 (2003).
- [Ji04] Ji X., Ann. Rev. Nucl. Part. Sci. **54**, 413 (2004).
- [Jon00] Jones M. K. *et al.* [Jefferson Lab Hall A Collaboration], Phys. Rev. Lett. **84**, 1398 (2000).
- [Jon06] Jones M. K. *et al.* [Jefferson Lab Resonance Spin Structure Collaboration], Phys. Rev. C **74**, 035201 (2006).
- [Jon91] Jones-Woodward C. E. *et al.*, Phys. Rev. C **44**, 571 (1991).
- [Jou97] Jourdan E. E. W., I. Sick and J. Zhao, comment in Phys. Rev. Lett **79**, 5186 (1997).
- [Jul04] Julia-Diaz B., D. O. Riska and F. Coester, Phys. Rev. C **69**, 035212 (2004).
- [Kel02] Kelly J. J., Phys. Rev. C **66**, 065203 (2002).
- [Kel04] Kelly J. J., Phys. Rev. C **70**, 068202 (2004).
- [Kon80] Koniuk R. and N. Isgur, Phys. Rev. D **21**, 1868 (1980) [Erratum-ibid. D **23**, 818 (1981)].
- [Kon05] Kondratyuk S., P. G. Blunden, W. Melnitchouk and J. A. Tjon, Phys. Rev. Lett. **95**, 172503 (2005).
- [Kro91] Kroll P., M. Schürmann, and W. Schweiger, Z. Phys. A **338**, 339 (1991).
- [Kub01] Kubis B. and U. G. Meissner, Eur. Phys. J. C **18**, 747 (2001); B. Kubis and U. G. Meissner, Nucl. Phys. A **679**, 698 (2001).
- [Kub02] Kubon G. *et al.*, Phys. Lett. B **524**, 26 (2002).
- [Kvi06] Kvinikhidze A. and G. A. Miller, Phys. Rev. C **73**, 065203 (2006).
- [Lac81] Lacombe M., Phys Lett. **101**, 1439 (1981).
- [Lag91] Laget J. M., Phys. Lett. B **273**, 367 (1991).
- [Lei91] Leinweber D. B., R. M. Woloshyn and T. Draper, Phys. Rev. D **43**, 1659 (1991).
- [Lei93] Leinweber D. B. and T. D. Cohen, Phys. Rev. D **47**, 2147 (1993).
- [Lei00] Leinweber D. B., A. W. Thomas, K. Tsushima and S. V. Wright, Phys. Rev. D **61**, 074502 (2000).
- [Lei01] Leinweber D. B., A. W. Thomas and R. D. Young, Phys. Rev. Lett. **86**, 5011 (2001).
- [Lei04] Leinweber D. B., A. W. Thomas and R. D. Young, Phys. Rev. Lett. **92**, 242002 (2004).
- [Lep80] Lepage G. P. and S. J. Brodsky, Phys. Rev. D **22**, 2157 (1980).
- [Lic70] Licht A. L. and A. Pagnamenta, Phys. Rev. D **2** (1970) 1150; Phys. Rev. D **2** (1970) 1156.
- [Lit70] Litt J. *et al.*, Phys. Lett. B **31**, 40 (1970).

- [Lom01] Lomon E. L., Phys.Rev. C **64**, 035204 (2001).
- [Lu98] Lu D. H., A.W. Thomas and A.G. Williams, Phys. Rev. C **57**, 2628 (1998).
- [Lun93] Lung A. *et al.*, Phys. Rev. Lett. **70**, 718 (1993).
- [Ma02] Ma B. Q., D. Quing, and I. Schmidt, Phys. Rev C **65**, 035205 (2002).
- [MacL06] MacLachlan G. *et al.*, Nucl. Phys. A **764**, 261 (2006).
- [Mad03] Madey R. *et al.* [E93-038 Collaboration], Phys. Rev. Lett. **91**, 122002 (2003).
- [Mar93] Markowitz P. *et al.*, Phys. Rev. C **48**, 5 (1993).
- [Mar02] Martin A. D., R. G. Roberts, W. J. Stirling and R. S. Thorne, Phys. Lett. B **531**, 216 (2002).
- [Mar89] Martinelli G. and C. T. Sachrajda, Nucl. Phys. B **316**, 355 (1989).
- [Mat05] Matevosyan H. H., A. W. Thomas and G. A. Miller, Phys. Rev. C **72**, 065204 (2005); Phys. Rev. C **71**, 055204 (2005).
- [Mat05] Matevosyan H. H., A. W. Thomas and G. A. Miller, Phys. Rev. C **72**, 065204 (2005); Phys. Rev. C **71**, 055204 (2005).
- [Max69] Maximon L. C., Rev. Mod. Phys, **41**, 193 (1969).
- [Max00] Maximon L. C. and J.A. Tjon, Phys. Rev. C **62**, 054320 (2000).
- [McA56] McAllister R. W. and R. Hofstadter, Phys. Rev.**102**, 851 (1956).
- [McI57] McIntyre John A. and Sobhana Dhar, Phys. Rev. **106**, 1074 (1957).
- [McG06] McGovern J. A. and M. C. Birse, Phys. Rev. D **74**, 097501 (2006).
- [Mei97] Meissner U. G., V. Mull, J. Speth and J. W. van Orden, Phys. Lett. B **408**, 381 (1997).
- [Mei06] Meitanis N., MIT PhD thesis, unpublished (2006).
- [Mel00] Melnikov K. and T. van Ritbergen, Phys. Rev. Lett. **84**, 1673 (2000).
- [Mel74] Melosh H. J., Phys. Rev. D **9**, 1095 (1974).
- [Mer96] Mergell P., U.G. Meissner, and D. Drechsel, Nucl. Phys. A **596**, 367 (1996).
- [Mer02] Merten D., U. Loring, K. Kretzschmar, B. Metsch and H. R. Petry, Eur. Phys. J. A **14**, 477 (2002).
- [Mey94] Meyerhoff M. *et al.*, Phys. Lett. B **327**, 201 (1994).
- [Mil98] Milbrath B. D. *et al.* [Bates FPP collaboration], Phys. Rev. Lett. **80**, 452 (1998) [Erratum-ibid. **82**, 2221 (1999)].
- [Mil77] Miller D. *et al.*, Phys. Rev. D **16**, 2016 (1977).

- [Mil02a] Miller G. A. and M.R. Frank, Phys. Rev. C **65**, 065205 (2002).
- [Mil02b] Miller G. A., Phys. Rev. C **66**, 032201(R) (2002).
- [Mil03] Miller G. A., Phys. Rev. C **68**, 022201(R) (2003).
- [Mit77] Mitra A. N. and I. Kumari, Phys. Rev. D **15**, 261 (1977).
- [MoT69] Mo L. W. and Y.S. Tsai, Rev. Mod. Phys. **41**, 205 (1969).
- [Mul94] Müller D., D. Robaschik, B. Geyer, F. M. Dittes and J. Horejsi, Fortsch. Phys. **42**, 101 (1994).
- [Mun06] Muñoz Camacho C. *et al.* [Jefferson Lab Hall A Collaboration], arXiv:nucl-ex/0607029.
- [Mur74] Murphy J.J., Y.M. Shin and D.M. Skopik Phys. Rev. **C9**, 2125 (1974).
- [Nes83] Nesterenko V. A. and A. V. Radyushkin, Phys. Lett. B **128**, 439 (1983).
- [Ost99] Ostrick M.*et al.*, Phys. Rev. Lett. **83**, 276 (1999).
- [Pac00] Pace E., G. Salme, F. Cardarelli and S. Simula, Nucl. Phys. A **666&667**, 33c (2000).
- [Pac96] Pachucki K., Phys. Rev. A **53**, 209 (1996).
- [Pas99] Passchier I. *et al.*, Phys. Rev. Lett. **82**, 4988 (1999).
- [Pas04] Pascalutsa V., B. R. Holstein and M. Vanderhaeghen, Phys. Lett. B **600**, 239 (2004).
- [Pas06a] Pascalutsa V. and M. Vanderhaeghen, Phys. Lett. B **636**, 31 (2006).
- [Pas06b] Pascalutsa V., M. Vanderhaeghen and S. N. Yang, Phys. Rept. (2006) in press; arXiv:hep-ph/0609004.
- [Pas06c] Pascalutsa V. and M. Vanderhaeghen, arXiv:hep-ph/0611050.
- [Pen03] Pentchev L., JLab Technical Note No. TN-03-024 (2003).
- [Pet03] Petronzio R., S. Simula and G. Ricco, Phys. Rev. D **67**, 094004 (2003) [Erratum-ibid. D **68**, 099901 (2003)].
- [Pla90] Platchkov S. *et al.*, Nucl. Phys. **A510**, 740 (1990).
- [Pla05] Plaster B. *et al.* Phys. Rev. C **73**, 025205 (2006).
- [Pos01] Pospischil Th. *et al.*, Eur. Phys. J. A **12**, 125 (2001).
- [Pri71] Price L. E. *et al.*, Phys. Rev. D **4**, 45 (1971).
- [Pun05] Punjabi V. *et al.*, Phys. Rev. C **71**, 055202 (2005) [Erratum-ibid. C **71**, 069902 (2005)].
- [Qat04] Qattan I. A. *et al.*, Phys. Rev. Lett. **94**, 142301 (2005).

- [Rad84] Radyushkin A. V., Acta Phys. Polnica B **15**, 40 (1984).
- [Rad96] Radyushkin A. V., Phys. Lett. B **380**, 417 (1996).
- [Rad98] Radyushkin A. V., Phys. Rev. D **58**, 114008 (1998).
- [Ral04] Ralston J. P. and P. Jain, Phys.Rev. D **69**, 053008 (2004).
- [Ras86] Raskin A. S. and T.W. Donnelly, Ann. Phys. **191**, 78 (1986).
- [Rei68] Reid, R.V., Ann. of Phys. **50**, 411 (1968).
- [Rek89] Rekalo M. P., G. I. Gakh, and A. P. Rekalo, J. Phys. G **15**, 1223 (1989).
- [Roc82] Rock S. *et al.*, Phys. Rev. Lett. **49**, 1139 (1982).
- [Roc92] Rock S. *et al.* Phys. Rev D **46**, 24 (1992).
- [Roh99] Rohe D. *et al.*, Phys. Rev. Lett. **83**, 4257 (1999).
- [Rose47] Rose M. E., Phys. Rev. **73**, 279 (1947).
- [Ros50] Rosenbluth M. N., Phys. Rev. **79**, 615 (1950).
- [Ros00] Rosenfelder R., Phys. Lett. B **479**, 381 (2000).
- [Sal55] Salzmann G., Phys. Rev **99**, 973 (1955).
- [Schi49] Schiff L. I., Stanford Microwave Laboratory, report no. 102 (1949), unpublished.
- [Schi01] Schiavilla R. and I. Sick, Phys. Rev. C **64**, 041002 (2001).
- [Schi05] Schindler M. R., J. Gegelia and S. Scherer, Eur. Phys. J. A **26**, 1 (2005).
- [Schl93] Schlumpf F., Phys. Rev. D **47**, 4114 (1993); J. Phys. G **20**, 237 (1994).
- [Schw67] Schwinger, Julian, Phys. Rev. Lett. **19**, 1154 (1967).
- [Schw99] Schwob C. *et al.*, Phys. Rev. Lett. **82**, 4960 (1999).
- [Sha06] Sharpe S. R., PoS **LAT2006**, [arXiv:hep-lat/0610094].
- [Sic05] Sick I., Nucl. Phys. A **755**, 265c (2005).
- [Sil93] Sill A. F. *et al.*, Phys. Rev. D **48**, 29 (1993).
- [Sim80] Simon G. G., Ch. Schmitt, F. Borowski and V.H. Walther, Nucl. Phys. A **333** (1980).
- [Spi83] Spinka H. *et al.*, Nucl. Instrum. Meth. **211**, 239 (1983).
- [Ste66] Stein P., M. Binkley, A. Suri and W. Woodward, Phys. Rev. Lett. **16**, 592 (1966).
- [Ste01] Stepanyan S. *et al.* [CLAS Collaboration], Phys. Rev. Lett. **87**, 182002 (2001).

- [Ste33] Stern O., Nature **132**, 103 (1933).
- [Sto01] Stoler P., Phys. Rev. D **65**, 053013 (2002).
- [Str03] Strauch S. *et al.*, Phys. Rev. Lett. **91**, 052301 (2003).
- [Sul04] Suleiman R. *et al.*, JLab Proposal 04-019 (2004).
- [Tho82] Thomas A. W., Adv. Nucl. Phys. **13**, 1 (1984).
- [Tho92] Thompson A. K. *et al.*, Phys. Rev. Lett. **68**, 2901 (1992).
- [Tia01] Tiator L., D. Drechsel, O. Hanstein, S. S. Kamalov and S. N. Yang, Nucl. Phys. A **689**, 205 (2001).
- [Tia03] Tiator L., D. Drechsel, S. S. Kamalov and S. N. Yang, Eur. Phys. J. A **17**, 357 (2003).
- [Tib04] Tiburzi B. C., W. Detmold and G.A. Miller, Phys. Rev. D **70**, 093008 (2004).
- [Tom01] Tomasi-Gustafsson E. and M. P. Rekalo, Phys. Lett. B **504**, 291 (2001); arXiv:nucl-th/0307065.
- [Tom05a] Tomasi-Gustafsson E. and G. I. Gakh, Phys. Rev. C **72**, 015209 (2005).
- [Tom05b] Tomasi-Gustafsson E. and G. I. Gakh, Eur. Phys. J. A **26**, 285 (2005).
- [Tom06] Tomasi-Gustafsson E., arXiv:hep-ph/0610108.
- [Tsa61] Tsai Y. S., Phys. Rev. **122**, 1898 (1961).
- [Tsa71] Tsai Y. S., SLAC report, no. SLAC-PUB-848. 1971, unpublished.
- [Vdh00] Vanderhaeghen M., J. M. Friedrich, D. Lhuillier, D. Marchand, L. Van Hoorebeke and J. Van de Wiele, Phys. Rev. C **62**, 025501 (2000).
- [Wag01] Wagenbrunn R. F., S. Boffi, W. Klink, W. Plessas and M. Radici, Phys. Lett. B **511**, 33 (2001).
- [Wag05] Wagenbrunn R. F., T. Melde and W. Plessas, arXiv:hep-ph/0509047.
- [Wal59] Walecka J. D., Nuovo Cimento **11**, 821 (1959).
- [Wal89] Walker R. C. *et al.*, Phys. Lett. B **224**, 353 (1989).
- [Wal94] Walker R. C. *et al.*, Phys. Rev. D **49**, 5671 (1994).
- [Wal06] Walcher T., private communication.
- [War04] Warren G. *et al.* [Jefferson Lab E93-026 Collaboration], Phys. Rev. Lett. **92**, 042301 (2004).
- [Wei04] Weissbach F., K. Hencken, D. Rohe, I. Sick and D. Trautmann, arXiv:nucl-th/0411033.
- [Wil85] Wilcox W. and R. M. Woloshyn, Phys. Rev. Lett. **54**, 2653 (1985).
- [Wil64] Wilson R. R. and J. S. Levinger, Ann. Rev. Nucl. Part. Sci. **14**, 135 (1964).

- [Wil74] Wilson K. G., Phys. Rev. D **10**, 2445 (1974).
- [Wir84] Wiringa R. R., A. S. Smith and T. A. Ainsworth, Phys. Rev. **C29**, 1207 (1984).
- [Xu00] Xu W. *et al.*, Phys. Rev. Lett. **85**, 2900 (2000).
- [Xu03] Xu W. *et al.*, Phys. Rev. C **67**, 012201 (2003).
- [Yao06] Yao W. M. *et al.* [Particle Data Group], J. Phys. G **33**, 1 (2006).
- [Yea58] Yearian M. R. and R. Hofstadter, Phys. Rev. **110**, 553 (1958).
- [Yen57] Yennie D. R., M.M. Lévy and D.G. Ravenhall, Rev. Mod. Phys. **29**, 144 (1957).
- [Zem56] Zemach A. C., Phys. Rev. **104**, 1771 (1956).
- [Zhu01] Zhu H. *et al.*, Phys. Rev. Lett. **87**, 081801 (2001).